2009

Sedimentation on a mixed siliciclastic/carbonate continental margin over decadal to millennial timescales: Gulf of Papua

Zahid Muhammad
Louisiana State University and Agricultural and Mechanical College

SEDIMENTATION ON A MIXED SILICICLASTIC/CARBONATE CONTINENTAL MARGIN OVER DECADAL TO MILLENNIAL TIMESCALES: GULF OF PAPUA

A Dissertation
Submitted to the Graduate Faculty of the
Louisiana State University and
Agricultural and Mechanical College
in partial fulfillment of the
requirements for the degree of
Doctor of Philosophy

in

The Department of Oceanography and Coastal Sciences

by
Zahid Muhammad
B.S., Karachi University, 1994
M.S., Louisiana State University, 2001
August 2009

O the One Whom eyes cannot see, conjectures cannot grasp,
and describers cannot describe; Whom events cannot effect
and Who does not fear calamities; Who knows the weights of
the mountains and the volumes of the oceans and the counts
of the raindrops and of the tree leaves, and the counts of everything
on which night brings darkness and day brings the light;
(O the One from Whom) a heaven cannot hide another heaven;
nor the earth can hide another earth, nor an ocean can hide
what is in its depths, nor a mountain can hide what is behind
its ruggedness-make the last part of my life its best, my last
deed my best one, and the day I meet You my best day

ACKNOWLEDGEMENTS

I am greatly indebted to my co-advisor, Sam Bentley, who has guided me and supported me as a mentor and as a friend in all these years during my stay at LSU. I would also like to extend my appreciation to my co-advisor, Harry Roberts, and committee members Robert Carney and Phil Bart, who provided me with valuable insight and have been very supportive throughout my Ph.D. program.

The Department of Oceanography has been generous in providing assistantship to complete my program.

I would also like to thank all those friends and colleagues at LSU who helped me in one way or the other in completing my dissertation. I would like to thank the crew and scientists aboard the R/V Melville during the PANASH cruise for their assistance in collecting samples and data. Special thanks go to Lawrence Febo, Luke Patterson and Floyd De Mers for providing assistance during and after the PANASH cruise. I also thank other members of the MARGINS Source-to-Sink research group for useful discussions and constructive comments during my research. I thank Asif Hoda, who was instrumental in assisting me with the numerical model. This MARGINS Source-to-Sink research was funded by National Science Foundation grant OCE 0305373 to S. J. Bentley.

This project would not have been possible without the support and prayers of my parents and other family members.

TABLE OF CONTENTS

ABSTRACT

Sediments from the Gulf of Papua were examined to estimate particle flux and sediment mass accumulation rates on multiple timescales. Patterns of sediment mass accumulation and inventory-derived ^{210}Pb fluxes display regional variations, decreasing seaward, and along isobaths seaward from the northeastern shelf edge. The amount of terrigenous sediment load being discharged annually from the shelf and accumulating in Pandora Trough is approximately 7-14×10^{6} tonnes. The existence of possible turbidity-current transport and deposition have been documented in deeper parts of the Gulf of Papua. High excess ^{210}Pb fluxes estimated from seabed inventories at the shelf edge and upper slope are consistent with the combined effects of sediment focusing and boundary scavenging of oceanic water masses. Sediments may be transported from inner-shelf depocenters by oceanic processes, focused in depocenters near the northeastern Gulf of Papua shelf edge, and distributed downslope through a combination of nepheloid-layer flow and possible turbidity-currents.

For the cores located between shelf edge and lower slope, biodiffusion coefficients and mixing depths exhibit a decreasing trend with increasing water depth. Using a two-layer model, biodiffusion coefficients in these cores are in the range of 0.007-60 cm^2 y^{-1} for the upper layer and 0.002-2.9 cm^2 y^{-1} for the bottom layer. Sediment mass accumulation rates without the influence of physical mixing are probably overestimated by a factor of ~1.4.

Jumbo piston cores taken from the shelf edge and upper and middle slope in the northern Pandora Trough suggest variation in sediment mass accumulation rates during post-Last Glacial Maximum (LGM) sea level rise. Upper 12 m of the sediment on the northeastern shelf edge has deposited in < 12 ky BP after post-LGM sea level rise. The bulk of this mud deposit, with mass accumulation rates as high as 3900 g cm^{-2} ky^{-1}, is constrained between the time of Last Glacial Maximun and Younger Dryas. The findings from this study suggest that physical processes

building the mud wedge on the northeastern Gulf of Papua shelf were similar to the physical processes acting today building the clinoform in the western Gulf of Papua shelf.

CHAPTER 1
INTRODUCTION

Continental margins reflect a diverse range of geological, physical and climatic conditions that collectively modulate transfer of terrigenous sediments to the coastal oceans and deposition on the shelf and slope [e.g. *Nittrouer and Wright*, 1994]. The processes which build this stratigraphic record on continental margins vary over spatial and temporal scales [*Leeder*, 1999]. On a century timescale, seasonal variations, river discharge, ocean currents, and local seabed morphology may decide the fate of sedimentary particles [*Milliman and Syvitski*, 1992]. On a millennium timescale, this sedimentary record is influenced by climatic cycles such as glacial-interglacial periods, sea level fluctuations and regional tectonics [*Leeder*, 1999]. Although natural variability in the environment is inherent, rapid industrialization and exploitation of natural resources since the last century has become a major factor in altering sediment flux to continental margins [*Syvitski et al*., 2005; *Wilkinson and McElroy*, 2007].

The MARGINS Source-to-Sink (S2S) initiative was aimed at developing a quantitative understanding of sediment transport and accumulation across and along continental margins [*NSF MARGINS Office*, 2004]. The Gulf of Papua located in the northeastern Australian continental margin represents one of the focus areas in the S2S Initiative, chosen in part because of its relatively closed system, low latitude location, relatively pristine natural environment, and juxtaposition of large siliciclastic and carbonate sediment sources [*Davies et al*., 1989; *Francis et al*., 2008]. Several very large rivers draining southern Papua New Guinea currently deliver 200-300 megatonnes (Mt) of terrigenous siliciclastic material (e.g., clay, quartz, feldspars) to the Gulf of Papua inner shelf each year [*Harris et al*., 1993; *Milliman*, 1995] (**Figure 1.1**).

Sediment delivered to the Gulf of Papua continental margin is distributed by a combination of tidal, wind-driven, and baroclinic currents [*Wolanski and Alongi*, 1995;

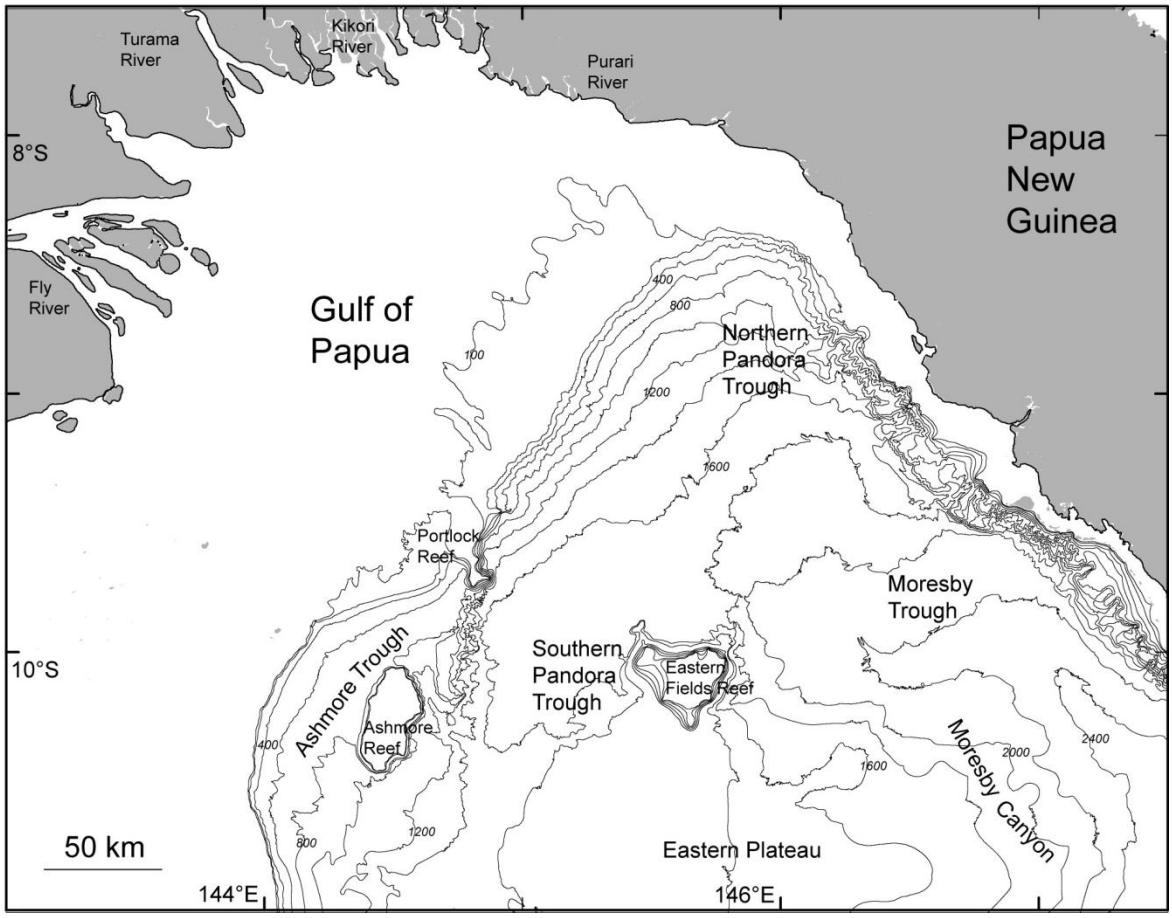

Figure 1.1 Gulf of Papua study area. Bathymetric contour interval is in meters.

Harris et al., 1996; *Keen et al.*, 2006; *Slingerland et al.*, 2004; *Walsh et al.*, 2004]. Tides on the shelf are mostly semidiurnal and the shelf has a maximum spring tidal range of 4–5 m [*Harris et al.*, 2004]. Wind-driven currents show two dominant circulation states that are highly influenced by seasonal monsoon and trade winds [*Hemer et al.*, 2004]. During the southern hemisphere monsoon season from December to March, winds are generally weak (1–2 m s^{-1}) [*Slingerland et al*., 2008]. In winter, trade winds that commence from the southeast are strong (4–5 m s^{-1}) with a large fetch over the Gulf of Papua [*Slingerland et al*., 2008]. The South Equatorial Current (SEC) is a large, westward, geostrophic flow which drives circulation in the Gulf of Papua [*Wolanski*, 1994]. This SEC bifurcates at 18°S in the Coral Sea into the Coral Sea Current (CSC)

to the north [*Bostock et al.*, 2006]. The CSC forms a clockwise gyre that sweeps along the outer shelf of the Gulf of Papua from the south and follows the southeastern Papuan peninsula as it travels eastward [*Andrews and Clegg*, 1989].

Of the total 200-300 Mt of terrigenous siliciclastic material discharged from Papua New Guinea rivers, some 100 Mt y^{-1} accumulate on the inner and middle shelf in an extensive prograding delta system [*Harris et al.*, 1993; *Walsh et al.*, 2004]. Another 10–15 Mt y^{-1} is probably being sequestered in prograding mangrove regions in western Gulf of Papua [*Wolanski et al.*, 1998; *Walsh and Nittrouer*, 2004]. Based on these calculations, huge amounts of siliciclastic sediment that exceed 100 × Mt y^{-1} may be escaping the Gulf of Papua shelf on the 100-year timescale. However, recent work has indicated that ~ 15 × Mt y^{-1} escapes the shelf edge [*Walsh and Nittrouer*, 2003]. Also, core stratigraphy in deeper seabed region of Gulf of Papua shows alternating turbidite and hemipelagic intervals deposited since the Last Glacial Maximum (LGM) [*Jorry et al.*, 2008]. The issue is if these alternating turbidite and hemipelagic intervals represent periods of variable terrigenous input in the Gulf of Papua since post-LGM sea level rise.

This dissertation focuses on sediment accumulation rates in the Gulf of Papua on multiple timescales. Sediment mass accumulation rates and particles fluxes on the shelf and slope on a century timescale are estimated using a naturally occurring radioisotope tracer. This sediment mass accumulation is also influenced by particle mixing at the seabed due to bioturbation. A two-layer one-dimensional numerical model is applied to estimate bioturbation coefficient for selected core location. Sedimentary processes on a millennium time scale influenced by global climate change and tectonics require a longer record. To elucidate the sedimentary record that may extend back to the last glacial maximum, jumbo piston cores taken from the shelf and upper slope in the northeastern continental margin are analyzed.

Chapter 2 discusses excess ^{210}Pb inventories and fluxes along shelf and slope of the Gulf of Papua and examines sediment dispersal pathways from source-to-sink. A suite of 30 multi-cores taken from the study area are used to constrain sediment mass accumulation rates on a 100-year timescale.

The estimates of sediment accumulation rates are refined in Chapter 3 by incorporating influences of particle mixing rates on ^{210}Pb profiles for sediment cores taken from the Gulf of Papua (GoP) shelf and slope. The primary approach to constrain patterns of bioturbation is by using a two-layer numerical model to evaluate patterns of vertical profiles of ^{210}Pb.

Chapter 4 examines the Late Quaternary sedimentation and buildup on the shelf edge and upper slope in the northeastern Gulf of Papua since LGM. Three jumbo piston cores taken between the shelf edge and middle slope are studied to constrain the timing and formation of the sediment blanket on the northeastern shelf edge.

Finally, chapter 5 summarizes the conclusions of the present study.

1.1 References

Andrews, J. C., and S. Clegg (1989), Coral sea circulation and transport deduced from modal information models, *Deep Sea Res., Part A*, *36*, 957–974.

Bostock, H. C., B. N. Opdyke, M. K. Gagan, A. E. Kiss, and L. K. Fifield (2006), Glacial/interglacial changes in the East Australian Current, *Clim. Dyn.*, *26*(6), 645–659.

Davies, P. J., P. A. Symonds, D. A. Feary, and C. J. Pigram (1989), The evolution of the carbonate platforms of northeast Australia, in *Controls on Carbonate Platform and Basin Development*, edited by P. D. Crevello, Spec. Publ. SEPM Soc. Sediment. Geol., *44*, 233–258.

Francis, J. M., J. J. Daniell, A. W. Droxler, G. R. Dickens, S. J. Bentley, L. C. Peterson, B. Opdyke, and L. Beaufort (2008), Deep-water geomorphology and sediment pathways of the mixed siliciclastic-carbonate system, Gulf of Papua, *J. Geophys. Res.*, *113*, doi:10.1029/2007JF000851.

Harris, P. T., E. K. Baker, A. R. Cole, and S. A. Short (1993), A preliminary study of sedimentation in the tidally dominated Fly River delta, Gulf of Papua, *Cont. Shelf Res.*, *13*, 441–472.

Harris, P. T., C. B. Pattiaratchi, J. B. Keene, R. W. Dalrymple, J. V. Gardner, E. K. Baker, A. R. Cole, D. Mitchell, P. Gibbs, and W. W. Schroeder (1996), Late Quaternary deltaic and carbonate sedimentation in the Gulf of Papua foreland basin: Response to sea-level change, *J. Sediment. Res.*, *66*, 801–819.

Harris, P. T., M. G. Hughes, E. K. Baker, R. W. Dalrymple, and J. B. Keene (2004), Sediment transport in distributary channels and its export to the pro-deltaic environment in a tidally dominated delta: Fly River, Papua New Guinea, *Cont. Shelf Res.*, *24*, 2431–2454.

Hemer, M. A., P. T. Harris, R. Coleman, and J. Hunter (2004), Sediment mobility due to currents and waves in the Torres Strait–Gulf of Papua region, *Cont. Shelf Res.*, *24*, 2297–2316.

Jorry, S. J., A. W. Droxler, G. Mallarino, G. R. Dickens, S. J. Bentley, L. Beaufort, L. C. Peterson, and B. N. Opdyke (2008), Bundled turbidite deposition in the central Pandora Trough (Gulf of Papua) since Last Glacial Maximum: Linking sediment nature and accumulation to sea level fluctuations at millennial timescale, *J. Geophys. Res.*, 113, doi:10.1029/2006JF000649.

Keen, T. R., D. S. Ko, R. L. Slingerland, S. Riedlinger, and P. Flynn (2006), Potential transport pathways of terrigenous material in the Gulf of Papua, *Geophys. Res. Lett.*, *33*, L04608, doi:10.1029/2005GL025416.

Leeder, M. R. (Ed.) (1999), *Sedimentology and sedimentary basins: from turbulence to tectonics*, 592 pp., Blackwell Science, Oxford.

Milliman, J. D., and J. P.M. Syvitski (1992), Geomorphic/tectonic control of sediment discharge to the ocean: the importance of small mountainous rivers, *J. Geol*., *100*, 525-544.

Milliman, J. D. (1995), Sediment discharge to the ocean from small mountainous rivers: the New Guinea example, *Geo-Mar. Lett.*, *15*, 127-133.

Nittrouer, C. A., and L. D. Wright (1994), Transport of particles across continental shelves, *Rev. Geophys*., *32*, 85-113.

NSF MARGINS Office (2004), NSF MARGINS Program Science Plans, pp. 170, Lamont-Doherty Earth Obs., Columbia Univ., Ithaca, N. Y.

Slingerland, R. L., J. D. Milliman, N. W. Driscoll, J. P. Walsh, and T. R. Keen (2004), Development of the Holocene clinoform in the Gulf of Papua, *Eos Trans. AGU*, *85*(47), Fall Meet. Suppl., OS44A-06.

Slingerland, R., R. W. Selover, A. S. Ogston, T. R. Keen, N. W. Driscoll, and J. D. Milliman (2008b), Building the Holocene clinothem in the Gulf of Papua: An ocean circulation study, *J. Geophys. Res.*, doi:10.1029/2006JF000680.

Syvitski, J. P. M., C. J. Vörösmarty, A. J. Kettner, and P. Green (2005), Impact of humans on the flux of terrestrial sediment to the global coastal ocean, *Science*, *308*, 376-380.

Walsh, J. P., and C. A. Nittrouer (2004), Mangrove-bank sedimentation in a mesotidal environment with large sediment supply, Gulf of Papua, *Mar. Geol.*, *208*, 225–248.

Walsh, J. P., C. A. Nittrouer, C. M. Palinkas, A. S. Ogston, R. W. Sternberg, and G. J. Brunskill (2004), Clinoform mechanics in the Gulf of Papua, New Guinea, *Cont. Shelf Res.*, *24*, 2487–2510.

Wilkinson, B. H., and B. J. McElroy (2007), The impact of humans on continental erosion and sedimentation, *GSA Bull.*, *119*, 140-156.

Wolanski, E. (1994), *Physical Oceanographic Processes of the Great Barrier Reef*, 194 pp., CRC Press, Boca Raton, Fla.

Wolanski, E., and D. M. Alongi (1995), A hypothesis for the formation of a mud bank in the Gulf of Papua, *Geo Mar. Lett.*, *15*(3–4), 166–171.

Wolanski, E., R. J. Gibbs, S. Spagnol, B. King, and G. Brunskill (1998), Inorganic sediment budget in the mangrove-fringed Fly River Delta, Papua New Guinea, *Mangroves Salt Marshes*, *2*, 85–98.

CHAPTER 2
EXCESS ^{210}Pb INVENTORIES AND FLUXES ALONG THE CONTINENTAL SLOPE AND BASINS OF THE GULF OF PAPUA*

2.1 Introduction

The MARGINS Source-to-Sink (S2S) initiative aims to develop a quantitative understanding of sediment transport and accumulation across and along continental margins [*NSF MARGINS Science Plans*, 2004]. The uplands of southern Papua New Guinea (PNG) and the adjacent Gulf of Papua (GoP) (**Figure 2.1**) were chosen because of large production of siliciclastic and carbonate sediments, clearly defined sediment sources and sinks, variable sediment fluxes over a range of timescales, and a relatively pristine environment [*NSF MARGINS Science Plans*, 2004].

A series of rivers deliver some 200 to 365×10^6 tonnes per year of siliciclastic sediment (e.g., quartz, feldspars, clays) to the inner shelf of the northern GoP annually [*Harris et al*., 1993; *Milliman*, 1995; *Milliman et al*., 1999]. This massive sediment discharge is largely due to voluminous rainfall (4-10 m y^{-1} in many places) on young and very steep (erodible) mountains where landslides frequently occur [*Pickup*, 1984; *Harris et al*., 1993]. Of the total mass discharged, some 100×10^6 tonnes per year accumulate on the inner to middle shelf in an extensive prograding delta system comprised of clinoforms [*Harris et al*., 1993; *Walsh et al*., 2004]. Another $10\text{-}15\times10^6$ tonnes per year may collect in mangrove covered coastal regions [*Wolanski et al*., 1998; *Walsh and Nittrouer*, 2004]. Assuming that these estimates are correct, huge amounts of siliciclastic sediment ($> 100\times10^6$ tonnes per year) escape the GoP shelf, at least on the 100-year timescale. However, *Walsh and Nittrouer* [2003] indicate that very little fluvially-derived sediment ($<15\times10^6$ tonnes per year) accumulates beyond the shelf break.

---

* Submitted and accepted for publication in *Journal of Geophysical Research – Earth Surface*, Reproduced by permission of American Geophysical Union, see APPENDIX F.

Sedimentary facies across the northern GoP shelf can be generally divided into a silt/sand-rich region of clinoform topsets on the inner shelf, a fine-grained region of clinoform foresets on the middle shelf, and a region of relict lithogenic and carbonate sands on the outer shelf [*Harris et al*., 1993; *Brunskill et al.*, 1995; *Walsh and Nittrouer*, 2003]. This distribution suggests that very little sediment presently crosses the shelf directly south of the major river inputs. However, some sediment from fluvial sources either bypasses the clinoform or is resuspended from the clinoform to be transported clockwise around the GoP shelf [*Harris et al*., 1993; *Wolanski et al*., 1995; *Walsh et al*., 2004; *Ogston et al*., 2008]. A portion of this suspended-sediment flux crosses the outer shelf in the northeastern GoP, where the shelf narrows dramatically (**Figure 2.1**). *Walsh and Nittrouer* [2003] suggest that nepheloid layers, created by northeastward alongshelf advection, transport the sediment. In any case, thick prograding sediment packages extend to the shelf edge in this area [*Wolanski and Alongi*, 1995, *Slingerland et al.*, 2008a; *Francis et al*., 2008], likely supplying siliciclastic sediment to adjacent deep-water environments.

Slope and basin settings in the GoP (**Figure 2.1**) can be divided into three large physiographic regions: Pandora Trough, Ashmore Trough and, Moresby Trough [*Winterer*, 1970; *Francis et al*., 2008]. Pandora Trough is a SW-NE trending basin confined by Portlock Reef, Boot Reef, and Ashmore Reef to the west, Eastern Plateau to the southeast, and the shelf edge to the north and east. The southwestern end is a ~1700 m deep semi-enclosed basin without a clear modern outlet, whereas the northeastern end is connected to Moresby Trough at ~2000 m water depth [*Francis et al*., 2008]. Ashmore Trough is a SSW-NNE trending feature rimmed by active carbonate reef systems on two sides and a water depth of less than 1000 m [*Francis et al*., 2008]. The third deep region, Moresby Trough, is a NW-SE trending basin confined by the narrow shelf of the Papuan Peninsula to the northeast, and Eastern Plateau and Eastern Fields

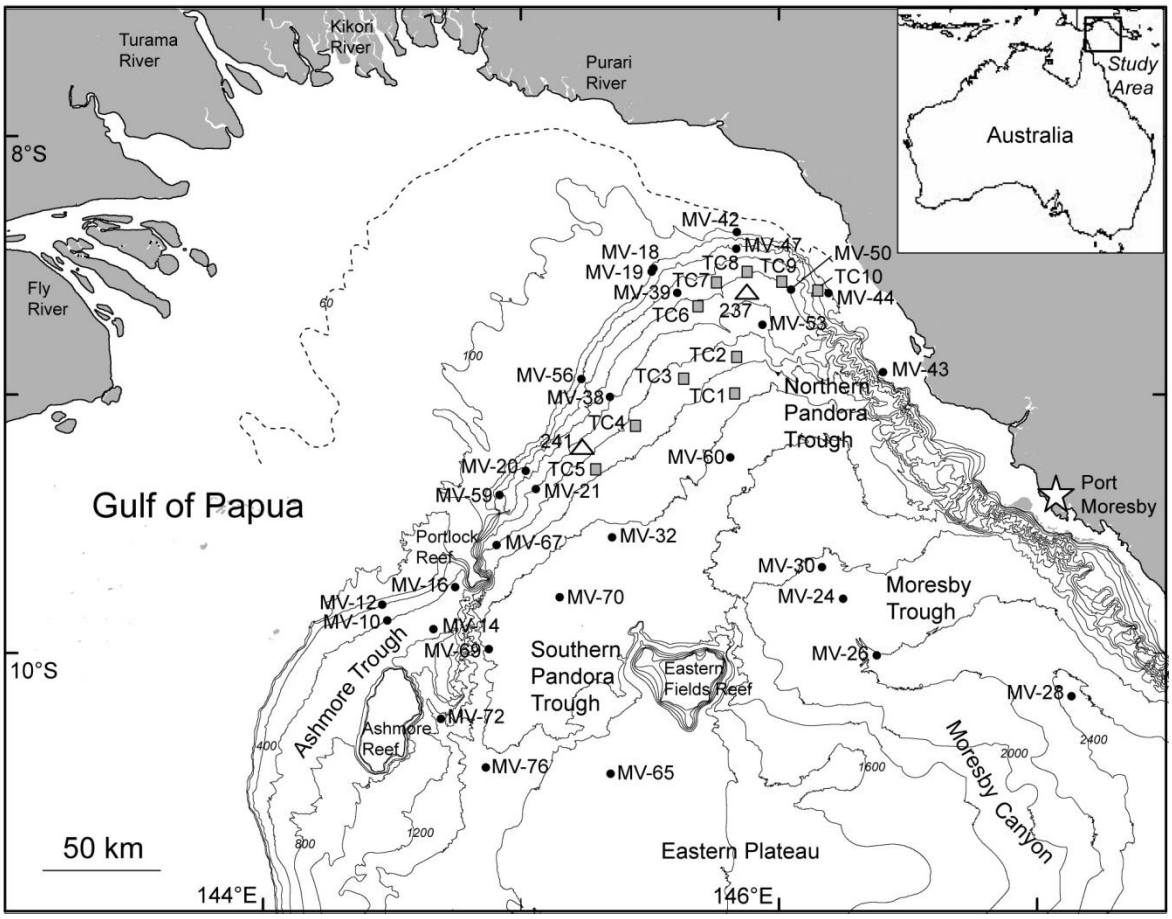

Figure 2.1. Map of the Gulf of Papua (GoP) region showing the continental slope, major basinsand reefs. The hashed line on the inner shelf is the 60-m isobath showing the extent of prograding clinoform. Black dots show locations of multi-cores examined in this study, whereas gray squares and white triangles show locations of cores examined by *Walsh and Nittrouer* [2003] and *Brunskill et al*., [2003], respectively. Bathymetric contour interval is 200 m; the 100-m contour is also shown.

Reef to the southwest. It is connected to the Coral Sea Basin via Moresby Canyon in the southeast.

The three deepwater structural basins collectively constitute a major depocenter for sediment escaping the GoP shelf (**Figure 2.1**). Sedimentation in Ashmore Trough is presently dominated by neritic carbonate input from surrounding reefs [*Francis et al*., 2008]. Pandora and Moresby troughs, however, receive enough terrigenous material so that siliciclastic contents of surface samples can exceed 80% [*Febo et al*., 2006]. This material presumably escapes from the

shelf to the slope, principally in the northeast GoP where the sediment packages cross the shelf edge.

To measure sediment accumulation on century timescales, Lead-210 (^{210}Pb), a naturally occurring radionuclide in marine sediments, has been widely used [e.g., *Goldberg and Koide*, 1962; *Nittrouer et al*., 1979]. Particles, organic or inorganic, scavenge ^{210}Pb from the water column and deposit ^{210}Pb in excess of that produced within sediments by the decay of its parent isotope, ^{226}Ra (half life = 1602 yr). As sediments are buried, ^{210}Pb decays with a half-life of 22 years [*Appleby and Oldfield*, 1992]. Bioturbation can significantly affect ^{210}Pb distributions in sediment [*Benninger et al*., 1979; *Thomson et al*., 1988]. However, measurement of ^{210}Pb activities at selected intervals can yield an activity-versus-depth relationship that can be used to estimate an apparent sediment accumulation rate [e.g., *Koide et al*., 1972; *Nittrouer et al*., 1984].

Two studies have examined ^{210}Pb in sediment from the outermost shelf, slope and basin regions in the GoP. *Walsh and Nittrouer* [2003] studied ten boxcores (**Figure 2.1**) in the northeast GoP, and determined apparent accumulation rates of ≤ 0.2 cm y^{-1} (0.08 g cm^{-2} y^{-1}). *Brunskill et al*. [2003] examined Kasten cores from the base of the slope where mass accumulation rates were between 0.05 and 0.07 g cm^{-2} y^{-1}. Core locations used for the above-cited studies were selected without the aid of detailed geoacoustic seabed surveys.

Recent studies in the GoP have highlighted the importance of designing seabed sampling based on multibeam and subbottom surveys so that depositional processes can be associated with known seabed geomorphology [*Slingerland et al*., 2008a]. Building on previous studies, we undertook a more extensive coring program in conjunction with detailed seabed mapping [*Daniell*, 2008; *Francis et al.*, 2008]. These studies allow us to identify and map major pathways (gullies, canyons and channels) for sediment transport from shelf and bank top sediments to deep water (by gravity flows and/or sediment plumes), and constrain ^{210}Pb inventories, ^{210}Pb

depositional fluxes, and rates of sediment accumulation associated with the depositional environments. These observations are then used to examine possible sediment-transport pathways and processes in the GoP.

2. 2 Materials and Methods

2.2.1 Field Sampling

Thirty multi-cores were collected from shelf edges and slope basins of the northern GoP during the PANASH cruise of the *R/V Melville* during March-April, 2004 (**Figure 2.1**). Core sites were selected based on seabed morphology and sedimentary facies determined from geoacoustic seabed mapping on the same cruise [*Francis et al*., 2008]. Positioning was accomplished by Differential Global Positioning System and the ship's dynamic positioning system. The use of a multi-corer allowed recovery of undisrupted sediment samples extending from the surface of the seabed to a maximum subsurface depth of 60 cm. The presence of clearly defined, oxidized core tops and *in situ* arborescent foraminifera and ophiuroids in some cores suggests that our multi-cores indeed recovered relatively undisturbed sediment samples.

Immediately after recovery, one sediment-filled core tube from each multi-corer deployment was extruded at 1-cm intervals for the top 6 cm, and at 2-cm intervals from 6 cm to the base. These samples were sealed in plastic bags and refrigerated until analysis in an onshore laboratory. One additional sediment-filled tube from each multi-core deployment was prepared for X-radiography. These were sliced into 2-cm-thick axial slabs, and imaged onboard using a Thales Flashscan 35 digital X-ray detector panel, illuminated with a Medison Acoma PX15HF X-ray generator. Images were archived as 14-bit grayscale images with 127-micron pixel resolution.

2.3 Laboratory Measurements and Theory

Samples for radionuclide measurements were dried for 24 hours at 60°C, ground with a porcelain mortar and pestle, and sealed with glue in 50×9 mm petri dishes. Weighed masses were then counted for 24 hours on Canberra low-background planar gamma detectors; correction for self-absorption of ^{210}Pb was done using the method of *Cutshall et al*. [1983]. Total ^{210}Pb was determined by measurement of the 46.5-KeV ^{210}Pb gamma peak. Supported ^{210}Pb from the decay of ^{226}Ra within the seabed was determined by measurement of the granddaughters of ^{226}Ra, ^{214}Pb (at 295 and 352-KeV) and ^{214}Bi (at 609-KeV). Excess (unsupported) ^{210}Pb was determined by subtracting total ^{210}Pb activity from supported ^{210}Pb activity for each interval. All values of excess ^{210}Pb were decay-corrected to the date of collection. Activities are reported in decays per minute (dpm), with one dpm = 1/60 Becquerels. Activity errors are derived from detector control software, and represent goodness-of-fit of a Gaussian curve to the observed spectral peak near 46.5 KeV. Minimum detectable activity for excess ^{210}Pb is 1 dpm g^{-1}, which is approximately three times the counting error for supported activity.

Apparent sediment accumulation rates (*SARs*) can be derived from ^{210}Pb observations using a one-dimensional, two-layer, steady-state model in which mixing of sediments occurs only in the upper layer [*Goldberg and Koide*, 1962; *Nittrouer et al*., 1979]. Such modeling assumes constant depositional rates for sediment and unsupported ^{210}Pb. It also assumes that the thickness of the mixed layer remains constant with time. The general equation for this steady-state model is:

$$dA/dt = D_b(\partial^2 A/\partial z^2) - S(\partial A/\partial z) - \lambda A \qquad (2.1)$$

where A = activity of radionuclide (dpm g^{-1}), D_b = particle mixing coefficient (cm^2 y^{-1}), λ = decay constant for radionuclide (y^{-1}), S = apparent sediment accumulation rate (*SAR*) in centimeter per year (cm y^{-1}), and z = depth in sediment column (cm).

Once sediments are deposited, they may undergo biological mixing by benthic organisms. If biological mixing can be ignored, then $D_b = 0$ in equation (2.1). The solution of equation (2.1) is then given by [*Krishnaswami et al*., 1980]:

$$A_z = A_0 e^{(-\lambda z/S)} \tag{2.2}$$

where A_0 is excess ^{210}Pb activity extrapolated to the sediment surface, and A_z is activity at depth z. Apparent accumulation rates (i.e., values of *SAR* that assume negligible effects of biological mixing) are then calculated using least-squares regressions of the ^{210}Pb profiles and application of equation (2) to ^{210}Pb data. In addition to *SAR*, we calculated sediment mass accumulation rate (*MAR*) according to: $MAR = (1-\Phi)\rho_s\, SAR$, where Φ is the average porosity for the core, and ρ_s is the density of sediment grains assumed to be 2.65 g cm^{-3}.

Under steady-state conditions of sediment accumulation and bioturbation, the distribution of excess ^{210}Pb activity in a core commonly delineates two distinct zones [e.g., *Nittrouer et al*., 1979; *Kuehl et al*., 1986]: a surface layer of uniform and high ^{210}Pb activity, where bioturbation thoroughly mixes sediments; and a lower zone of exponentially decreasing excess ^{210}Pb activity, where the activity gradient is influenced by sediment burial and ^{210}Pb decay. Below this depth, all detected ^{210}Pb is supported by decay of the parent radioisotope ^{226}Ra. Sediment accumulation rates herein are estimated from the log-linear slope for the lower interval of decreasing excess ^{210}Pb activity. Some cores appear to have a distinct surface mixed layer (e.g., MV-18, MV-21), but most do not. Nevertheless, only basal portions of ^{210}Pb profiles were used to estimate accumulation rates, to minimize the influence of bioturbation.

These sediment accumulation rates are upper limits because our calculations ignore the potential influences of bioturbation in this region. The minimum *SAR* we report is 0.05 cm y^{-1}, which is near the practical lower limit for ^{210}Pb geochronology and may be strongly influenced by slow, shallow bioturbation. This rate represents effectively negligible sediment accumulation

over 100-y timescales. However, the same rate extended over millennial timescales represents a significant sediment flux.

Other radioisotopes, including ^{137}Cs and ^{234}Th, have been used to constrain ^{210}Pb-derived *SARs*. However, ^{137}Cs was not detectable above our detection limit of 0.5 dpm g^{-1} for this radioisotope. The cruise duration and shipping times for samples precluded measurement of excess ^{234}Th, due to its short half life (24 d).

The effects of bioturbation undoubtedly introduce significant uncertainty into some of our *SAR* and *MAR* estimates. However, the use of ^{210}Pb inventories to constrain depositional fluxes is less influenced by the effects of bioturbation. The seabed inventory of excess ^{210}Pb is calculated as the product of depth-integrated radionuclide activity and sediment dry-bulk density. This seabed inventory is supplied by ^{210}Pb flux from the atmosphere and ^{210}Pb production in the water column. Sediment inventories of excess ^{210}Pb (dpm cm^{-2}) at the seabed can be calculated by the following equation:

$$I = \Sigma \rho_s \Delta z \, (1 - \Phi_i) \, A_i \qquad (2.3)$$

where I is inventory, ρ_s is mineral density, Δz is thickness (cm) of the sampled interval i (1 or 2 cm), Φ is porosity (measured by water loss at 60°C), and A is the excess ^{210}Pb activity (dpm g^{-1}) of the sampled interval. Sediment ^{210}Pb inventories reported here are minimum values because not all cores penetrated to depths below the zone of excess ^{210}Pb. However, additional contributions from deeper, unsampled intervals should be minimal, however, because excess ^{210}Pb activities at core bases were generally more than one order of magnitude lower than at the surface. Errors for radionuclide concentrations are propagated accordingly to obtain error for inventory values.

From this measured inventory of ^{210}Pb, we can estimate the annual flux of excess ^{210}Pb required to support the observed inventory at steady state. We refer to this as the core-calculated flux (F), determined by:

$$F=\lambda I \quad (2.4)$$

where F is the annual flux (dpm cm^{-2} y^{-1}), and λ is the radioactive decay constant for ^{210}Pb (0.031 y^{-1}).

2.4 Results

Core profiles of excess-^{210}Pb activity for the study area are shown in **Figure 2.2** and measured excess-^{210}Pb seabed inventories are given in **Table 2.1**.

For most multi-cores, X-radiographs display pervasively bioturbated sedimentary fabric. A typical example is core MV-14, located in the northern Ashmore Trough at a water depth of 760 m. Mottling without primary stratification characterizes sediment throughout the entire core (**Figure 2.3)**. A prominent exception to this pattern is core MV-24, taken from a well developed channel in Moresby Trough at a water depth of 2102 m. This core displays stratification at three depths (**Figure 2.3)**, consistent with turbidity-current deposition [*Bentley et al*., 2006a].

Across the entire study area, ^{210}Pb sediment accumulation rates are generally highest near the shelf edge in the northern Pandora Trough (**Figure 2.2**), and decrease with increasing water depth (**Figure 2.4**), toward the southwest (i.e., toward Ashmore Trough) (**Figure 2.2**). In the Pandora Trough, *SAR* and *MAR* drop from 0.35 cm y^{-1} and 0.20 g cm^{-2} y^{-1} for core MV-42 at the shelf edge (water depth = 91 m), to 0.21 cm y^{-1} and 0.11 g cm^{-2} y^{-1} for core MV-53 on the middle slope (water depth = 1111 m) (**Figure 2.2**). These values compare favorably with those determined by *Walsh and Nittrouer* [2003] ($\leq$ 2 mm y^{-1}, 0.1 g cm^{-2} y^{-1}; **Table 1**). A similar pattern is evident for upper-slope cores MV-18 and MV-19, and middle-slope core MV-38 (**Figure 2.2**, **Table 2.1**). All three cores are located along one channel system, with *MAR*

(a)

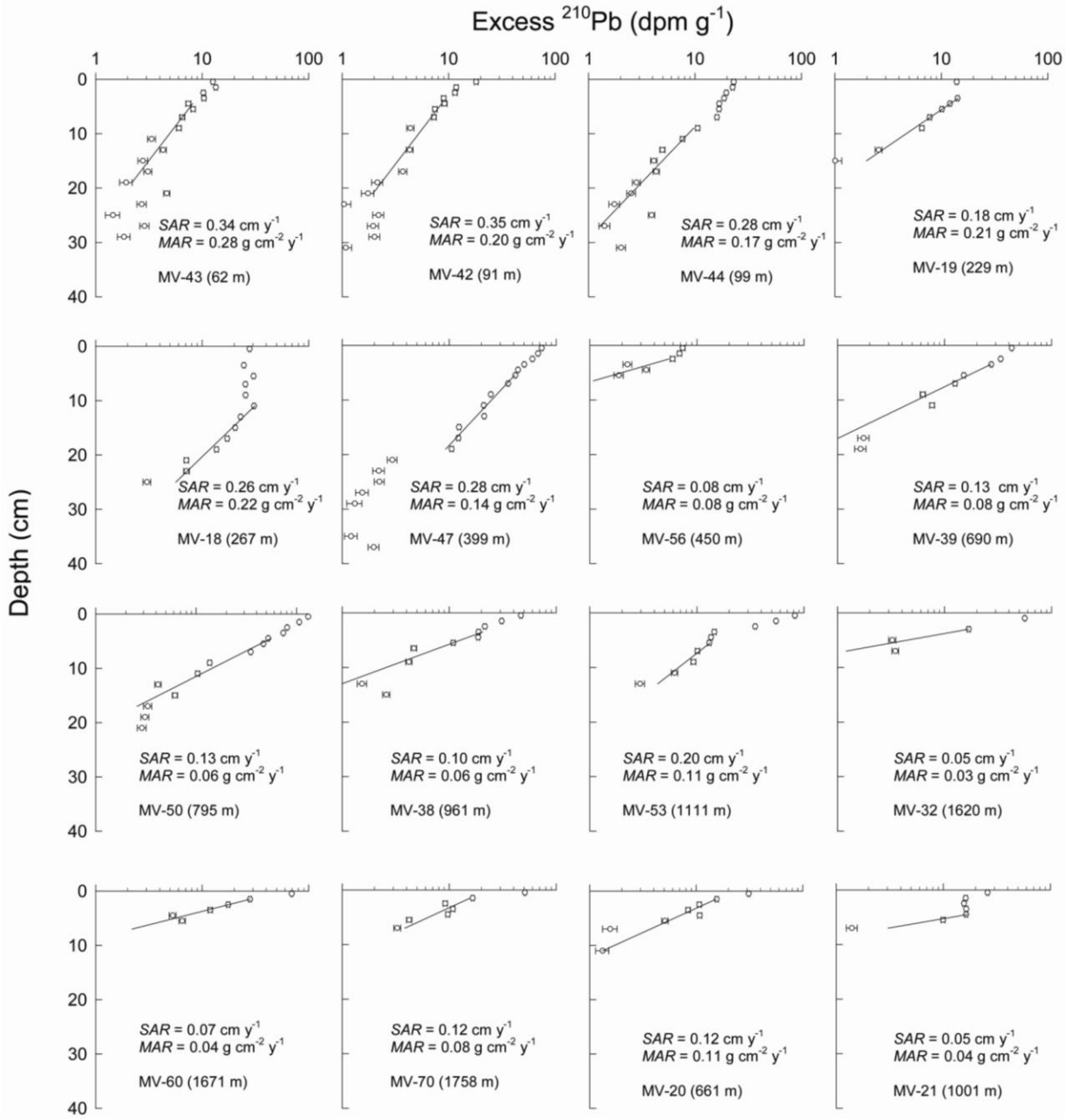

Figure 2.2. Excess ^{210}Pb activity (dpm g^{-1}; decay per minute per gram) is plotted on the x-axis and depth is plotted on the y-axis. Solid lines represent best fit through the data points. Core locations are shown in Fig. 1 and water depths are given in Table 1. (a) cores from the northern Pandora Trough, (b) cores from the Ashmore Trough and southwestern Pandora basin, (c) cores from the Moresby Trough channel.

(b)

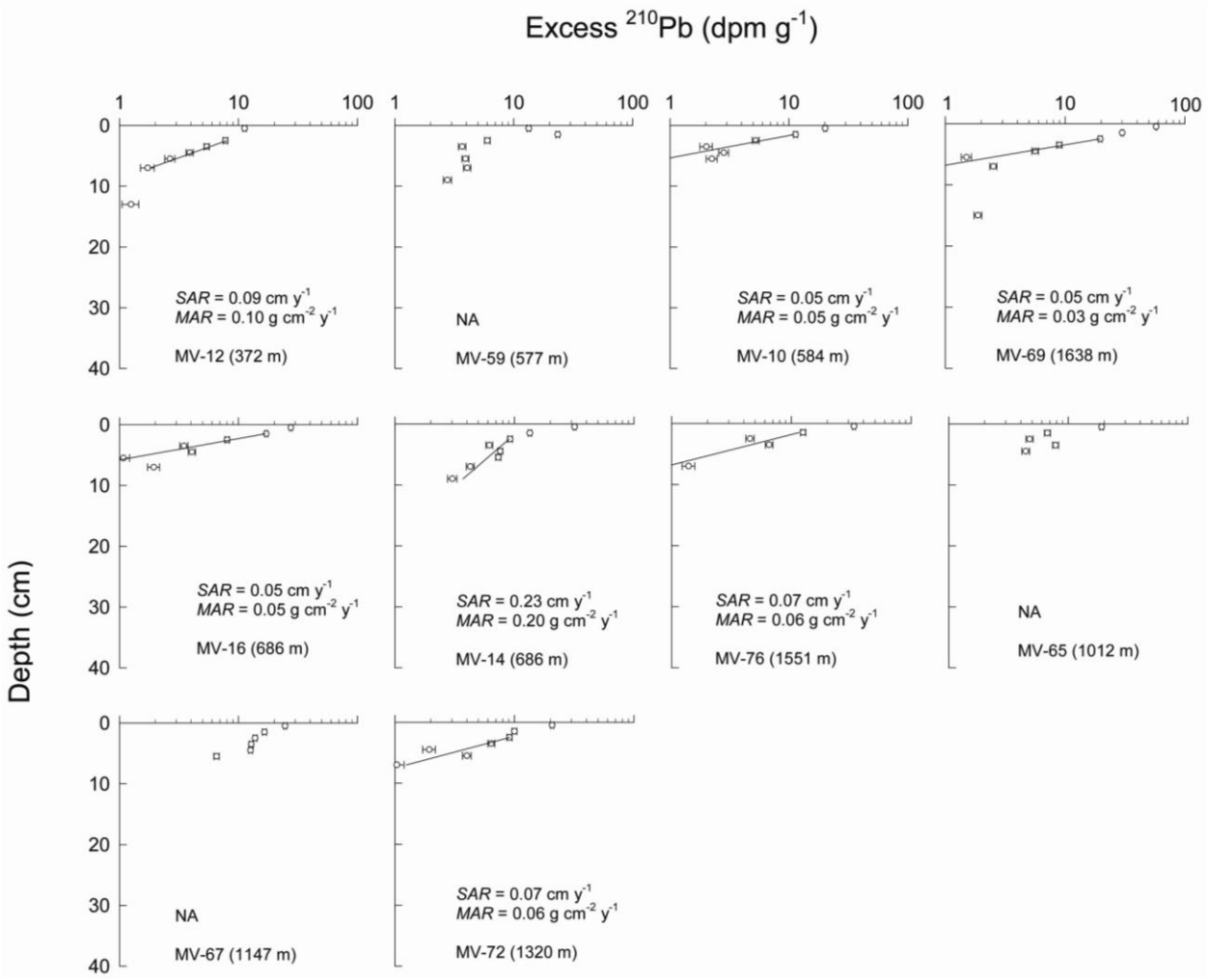

(c)

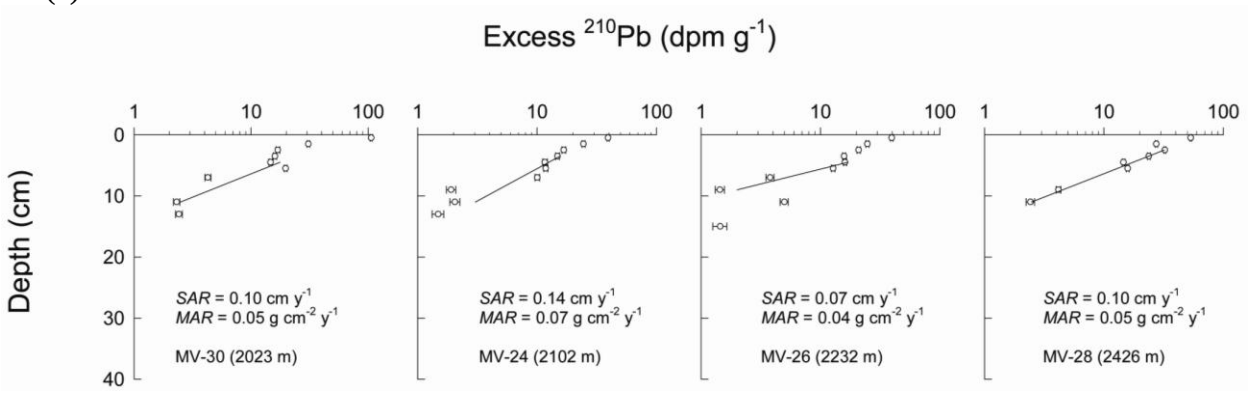

Figure 2.2. Continued.

Table 2.1. Excess ^{210}Pb surface activities, supported activities, measured inventories, estimated fluxes, and upper limits for sediment accumulation rates.

Core No.	Water depth (m)	Supported ^{210}Pb Activity (dpm g^{-1})[a]	Measured excess ^{210}Pb inventory (dpm cm^{-2})	Theoretical flux (dpm cm^{-2} y^{-1})[b]	R (Eq. 5)[c]	*SAR* (cm y^{-1})[d]	*MAR* (g cm^{-2} y^{-1})[e]
MV-10	584	0.64 ± 0.17	43	0.5	2.5	0.05	0.05
MV-12	372	0.52 ± 0.15	50	0.4	4.0	0.09	0.10
MV-14	760	1.1 ± 0.53	72	0.7	3.4	0.23	0.20
MV-16	686	1.3 ± 0.21	68	0.6	3.7	0.05	0.05
MV-18	267	0.97 ± 0.12	413	0.4	34.9	0.26	0.22
MV-19	229	0.86 ± 0.19	164	0.4	14.2	0.18	0.21
MV-20	661	1.2 ± 0.28	78	0.6	4.4	0.12	0.11
MV-21	1001	1.7 ± 0.22	83	0.8	3.1	0.05	0.04
MV-24	2102	2.2 ± 0.19	63	1.9	1.0	0.14	0.07
MV-26	2232	3.4 ± 0.44	76	2.0	1.2	0.07	0.04
MV-28	2426	3.7 ± 0.33	85	2.2	1.2	0.10	0.05
MV-30	2023	3.5 ± 0.33	87	1.9	1.5	0.10	0.05
MV-32	1620	4.2 ± 0.27	77	1.5	1.6	0.05	0.03
MV-38	961	3.1 ± 0.34	78	0.8	3.0	0.10	0.06
MV-39	690	1.4 ± 0.25	136	0.6	6.8	0.13	0.08
MV-42	91	1.4 ± 0.35	98	0.3	9.7	0.35	0.20
MV-43	62	0.53 ± 0.16	117	0.3	11.7	0.34	0.28
MV-44	99	1.4 ± 0.29	136	0.3	13.4	0.28	0.17
MV-47	399	0.89 ± 0.27	267	0.4	21.2	0.28	0.14
MV-50	795	2.2 ± 0.37	245	0.7	11.3	0.13	0.06
MV-53	1111	2.5 ± 0.38	140	0.9	4.8	0.21	0.11
MV-56	450	1.5 ± 0.20	29	0.4	2.1	0.08	0.08
MV-59	577	1.6 ± 0.19	74	0.5	4.4	NA	NA
MV-60	1671	3.5 ± 0.33	78	1.5	1.6	0.07	0.04
MV-65	1012	2.1 ± 0.26	31	0.8	1.1	NA	NA
MV-67	1147	2.2 ± 0.22	62	1.1	1.8	NA	NA
MV-69	1638	3.7 ± 0.28	83	1.5	1.7	0.05	0.03
MV-70	1758	4.6 ± 0.29	62	1.6	1.2	0.12	0.08
MV-72	1320	1.2 ± 0.28	45	1.2	1.2	0.07	0.06
MV-76	1551	2.3 ± 0.26	39	1.3	0.9	0.07	0.06
TC1						0.14[f]	0.07[f]
TC2						0.17[f]	0.1[f]
TC3						0.17[f]	0.1[f]
TC4						0.16[f]	0.08[f]
TC6						0.1[f]	0.05[f]
TC7						0.09[f]	0.06[f]
TC8						0.15[f]	0.08[f]
TC9						NA[f]	NA[f]
TC10						0.16[f]	0.08[f]
237	923						0.03[g]
241	1117						0.05[g]

[a] Supported ^{210}Pb = ^{210}Pb$_{total}$ - ^{210}Pb$_{excess}$.

[b] The theoretical flux is the sum of atmospheric fallout (0.3 dpm cm^{-2} y^{-1}) and ^{226}Ra water-column production from GEOSECS Western Pacific data [*Chung and Craig*, 1980].

[c] Ratio of core-derived flux (dpm cm^{-2} y^{-1}) estimated from measured ^{210}Pb$_{excess}$ inventory (dpm cm^{-2}) to theoretical flux (dpm cm^{-2} y^{-1}) given as *R*.

[d] Lead-210-derived apparent sediment accumulation rates calculated by least-squares fit of the analytical solution to the equation, assuming accumulation is dominant over bioturbation (D_b=0). These accumulation rates, therefore, represent a maximum estimate.

[e] *MAR* (g cm^{-2} y^{-1}) = $(1-\varphi)\,\rho_s$ *SAR* (cm y^{-1}) where φ is the average porosity for the entire length of each core, and ρ_s is the density of sediment grains (assumed to be 2.65 g cm^{-3}).

[f] *SAR* and *MAR* from *Walsh and Nittrouer* [2003].

[g] MAR from *Brunskill et al*. [2003].

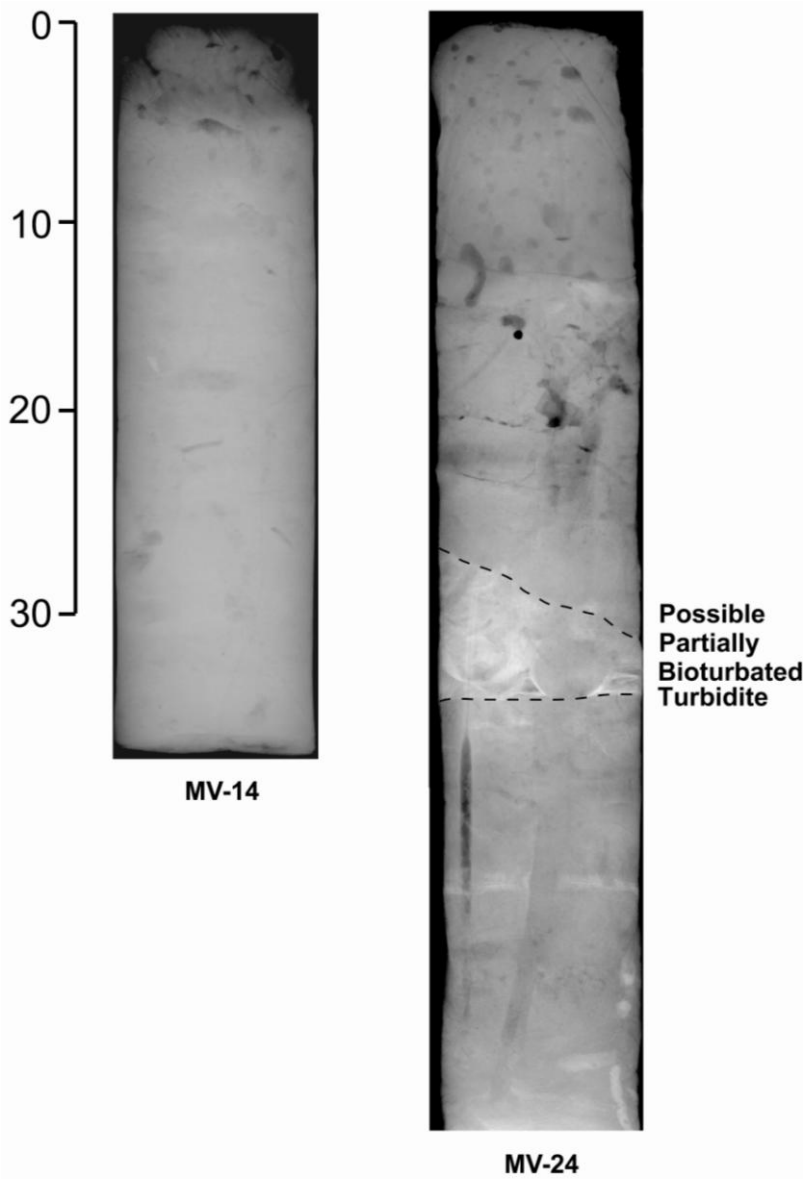

Figure 2.3. X-radiographs from multicores show sedimentary structure of seabed from GoP (scale in centimeters). The core on left (MV-14; water depth = 760 m) was from Ashmore Trough showing bioturbation and absence of any physical structures. This is typical of biogenic fabric observed in X-radiographs of most cores. The image on right (MV-24; water depth = 2102 m) taken from the Moresby Trough shows possible turbidite layers partially destroyed by bioturbation.

decreasing from ~0.22 g cm^{-2} y^{-1} at 230-270 m water depth to 0.06 g cm^{-2} yr^{-1} at 961 m water depth.

Significant variability exists across depositional facies at comparable depths, however. Pandora Trough core MV-56 (water depth = 450 m; **Figure 2.2**) was collected on the upper slope within a channel (based on multibeam data) (**Figure 2.2**). The seabed at this core location consists of coarse carbonate sands (> 250 μm), and the *SAR* for this core is less than 0.1 cm y^{-1} (**Table 1**). Core MV-47, collected from soft mud deposits at a comparable water depth (399 m) farther to the northeast, yields a similar *SAR* of 0.28 cm y^{-1}. In the southwestern Pandora Trough at water depths exceeding 1600 meters, accumulation rates measured for two cores, MV-60 and MV-70 are 0.07 cm y^{-1} (0.04 g cm^{-2} y^{-1}) and 0.12 cm y^{-1} (0.08 g cm^{-2} y^{-1}) respectively (**Figure 2.2**).

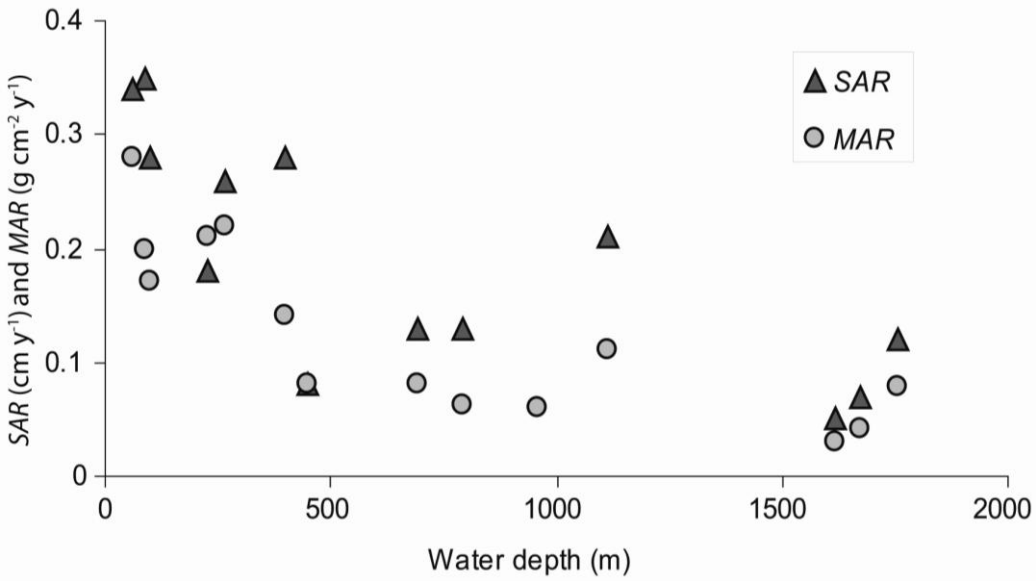

Figure 2.4. Sediment accumulation rate (*SAR*, cm y^{-1}) and mass accumulation rate (*MAR*, g cm^{-2} y^{-1}) of samples versus water depth in the northern Pandora Trough. The *SAR* and *MAR* decrease with increasing distance from the shelf and increasing water depth.

In the Ashmore Trough and southwestern Pandora Trough, upper limits of accumulation rates measured are between 0.05 cm y^{-1} and 0.23 cm y^{-1}. Excess ^{210}Pb profiles show simple distributions where excess ^{210}Pb activities decrease with depth. Core MV-59 (water depth = 577 m; **Figure 2.1**) was taken on the upper slope within a channel (based on multibeam data). The seabed at this core location consists of coarse carbonate sands (> 250 μm) and the penetration depth was only ~10 cm.

In the Moresby Trough, cores taken from water depths greater than 2000 m in a prominent channel and the mouth of Moresby Canyon display similar excess ^{210}Pb profiles, and yield upper limits for accumulation rates of 0.07-0.14 cm y^{-1} (0.04-0.07 g cm^{-2} y^{-1}; **Figure 2.2**). Primary stratification evident in core MV-24 (**Figure 2.3**) suggests that either bioturbation has been slower at this locale than elsewhere, or that sediment accumulation here has been more rapid (thus allowing preservation of primary fabric).

Excess ^{210}Pb inventories in the northeastern Pandora Trough range between 29 and 267 dpm cm^{-2} with highest inventories generally on the northeastern shelf, decreasing to the southwest (**Table 2.1** and **Figure 2.5**). One exception is core MV-18, collected from the upper slope near the mouth of a submarine canyon at 267 m water depth, which yielded the highest inventory at 413 dpm cm^{-2}. Inventories in the Ashmore Trough and southwestern Pandora Trough range between 31 and 83 dpm cm^{-2}, with the highest values generally occurring closest to the shelf edge, and lower values in deeper water, farther from the shelf edge. Excess ^{210}Pb inventories in the Moresby Trough channel are relatively uniform, covering a range of 63-87 dpm cm^{-2}.

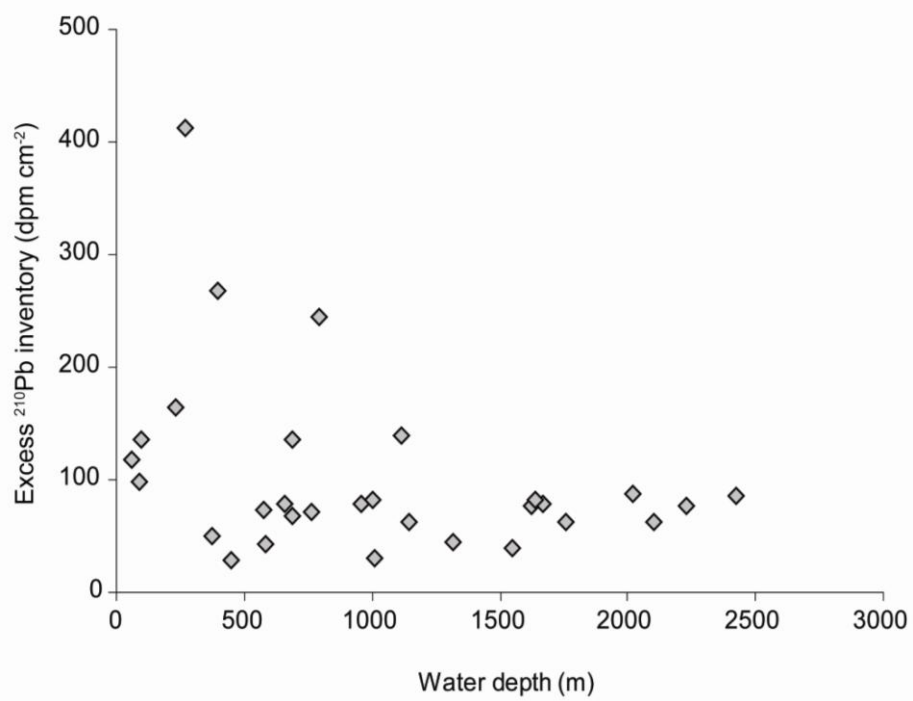

Figure 2.5. Excess ^{210}Pb inventory versus water depth in the northern Pandora Trough shelf break and slope region in GoP.

2.5 Discussion

2.5.1 Sediment Mass Accumulation Rates

2.5.1.1 Northern Pandora Trough

Patterns of sediment accumulation in the Pandora Trough seabed are consistent with this region's intermediate location in the GoP dispersal system, between shelf depocenters, and deep-sea fans farther south in the Coral Sea Basin (the ultimate sinks in this dispersal system; **Figure 2.1**) [*Winterer*, 1970]. Accumulation rates are highest on the outer-shelf and upper-slope region of the northeastern Pandora Trough (**Figure 2.2**), and decrease beyond the upper slope toward deeper water (**Figure** 2.**4**). Cores taken from the shelf-break (MV-42, MV-43, and MV-44) exhibit measured *SAR* values at least twice as large as *SAR* on the middle slope (MV-38, MV-39, MV-50 and MV-53). This decrease in accumulation rate from the shelf-break to the middle slope

could be in part due to a decrease in particle flux with increasing distance from the river source. However, *SAR* and *MAR* appear to decrease along isobaths to the southwest, closer to the Fly River, suggesting that the northeast shelf edge is a location of sediment focusing.

Cores MV-60 (*SAR* = 0.07 cm y^{-1}) and MV-32 (*SAR* = 0.05 cm y^{-1}) located on the lower open slope suggest that accumulation of terrigenous sediment is negligible on a 100-year timescale.

All cores collected from the Pandora Trough display wholly biogenic sedimentary fabric and lack any physical stratification, suggesting that sediment accumulation occurs slowly and steadily, allowing bioturbation to readily overprint primary depositional fabric [e.g., *Bentley et al*., 2006b].

2.5.1.2 Ashmore Trough and Southwestern Pandora Trough

Apparent *MARs* are generally low for cores in Ashmore Trough and the southwestern Pandora Trough (0.03-0.10 g cm^{-2} y^{-1}). A *MAR* value of 0.20 g cm^{-2} y^{-1} for core MV-14 is likely an upper limit due to bioturbation. The geomorphology of this region is dominated by a drowned barrier-reef system at the northern shelf edge which transitions into a relatively smooth seafloor toward south [*Francis et al.*, 2008]. Although channels are present in several places, seismic and piston-core data show uniformly thin pelagic and hemipelagic drapes that are primarily carbonate in composition [*Francis et al.*, 2008]. The low *SAR*'s and *MAR*'s for this area (**Table 1**; **Figures 2.1** and **2.2**) suggest terrigenous sediment accumulation is negligible on a 100-year timescale. The sedimentary fabric in the Ashmore Trough is wholly biogenic (e.g., MV-14) as revealed on X-radiograph (**Figure 2.3**), consistent with low accumulation rates and thorough bioturbation. The shelf reaches a maximum width of 150 km near the Ashmore Trough (**Figure 2.1**), and outer-shelf sediments include calcareous algal bioherms, suggesting that little terrigenous

sediment is crossing or accumulating in this region at present [*Harris et al.*, 1996]. Collectively, all information suggests that limited fluvial sediment reaches Ashmore Trough now.

2.5.1.3 Moresby Trough

To evaluate potential gravity-driven sediment delivery from the shelf into the deepest basin of the study area, we took cores from a prominent submarine channel in the Moresby Trough (**Figure 2.1**). This channel was identified during our multibeam and seismic surveys, and extends from the base of the northerneastern Pandora Trough slope to the Moresby Canyon in the southeastern part of the GoP [*Francis et al.*, 2008]. This channel is a likely conduit for long-term sediment delivery into the Moresby Canyon, as indicated by thick sequences of siliciclastic sediment in the Coral Sea Basin [*Ewing el al.*, 1970; *Winterer*, 1970; *Francis et al.*, 2008].

Cores collected from a channel in the Moresby Trough, downslope from the Pandora Trough, have low apparent *MARs* between 0.04 and 0.07 g cm^{-2} yr^{-1} (**Figure 2.2**). One core (MV-24) from this channel displays stratification suggesting possible turbidity-current deposition (**Figure 2.3**). Excess ^{210}Pb was detected in this core in samples at 12-14 cm, suggesting that the uppermost stratified bed could have been deposited in the past century or so. However, the presence of cross-cutting burrows in the X-radiograph of this core (**Figure 2.3**) also suggests that this excess ^{210}Pb activity could have been transported to these sediment depths via bioturbation, meaning that the bed is older. A jumbo piston core (MV-22) collected nearby from the same channel-levee complex has been studied by *Patterson et al*. [2006], and is composed of similar muddy turbidites in the upper ~2 m of core. The ages of the uppermost muddy turbidites in MV-22 have not been established, but the highly porous muddy sediment texture suggests that the turbidites are relatively recent [*Patterson et al*., 2006]. These observations suggest that this channel is probably a conduit of sediment transport southward

from the shelf edge by means of turbidity currents, and further suggest that such sediment delivery could continue farther into the deep basin via Moresby Canyon.

2.5.1.4 Sediment Accumulation in the Pandora Trough

In order to estimate apparent annual mass accumulation across the Pandora Trough (the region for which we have the most extensive core coverage), we have calculated a regionally weighted average for mass accumulation rates. A region extending from core MV-43 on the northeastern GoP shelf edge to the northeast corner of Eastern Fields Reef, and then to Portlock Reef and the adjacent shelf edge was outlined using GIS software (**Figure 2.7**). Values of *MAR* from **Table 1** were gridded at 5-km resolution using an inverse-square-distance interpolation algorithm, to produce a region of 19,800 km^2 with a spatially averaged *MAR* of 0.12 g cm^{-2} y^{-1}, and total annual apparent mass accumulation rate of ~23.7×10^6 tonnes per year. If the carbonate fraction of our total mass accumulation is ~40% of total sediment mass (**Figure 2.6**), the terrigenous fraction would thus account for ~14×10^6 tonnes per year, or ~5% of the estimated annual fluvial sediment flux to the GoP (~300×10^6 tonnes per year) [*Harris et al*., 1993; *Milliman*, 1995 ; *Milliman et al*., 1999].

We also estimated the sediment budget for the northern Pandora Trough using more localized averaging of *MAR* (**Figure 2.7**), to explore *MAR* variability associated with seabed morphology and locale. The surface area of each accumulation-rate region in **Figure 2.7** was determined using ArcGIS (ESRI) software. Spatially averaged *MARs* were determined using linear inverse-distance weighting. Using the localized *MAR* approach, we estimate a total sediment budget of ~11.3×10^6 tonnes per year, yielding a terrigenous fraction of ~7×10^6 tonnes per year over an area 60% the size of the regional budget area described above. This method highlights the fact that approximately 85% of terrigenous sediment delivery occurs in a relatively

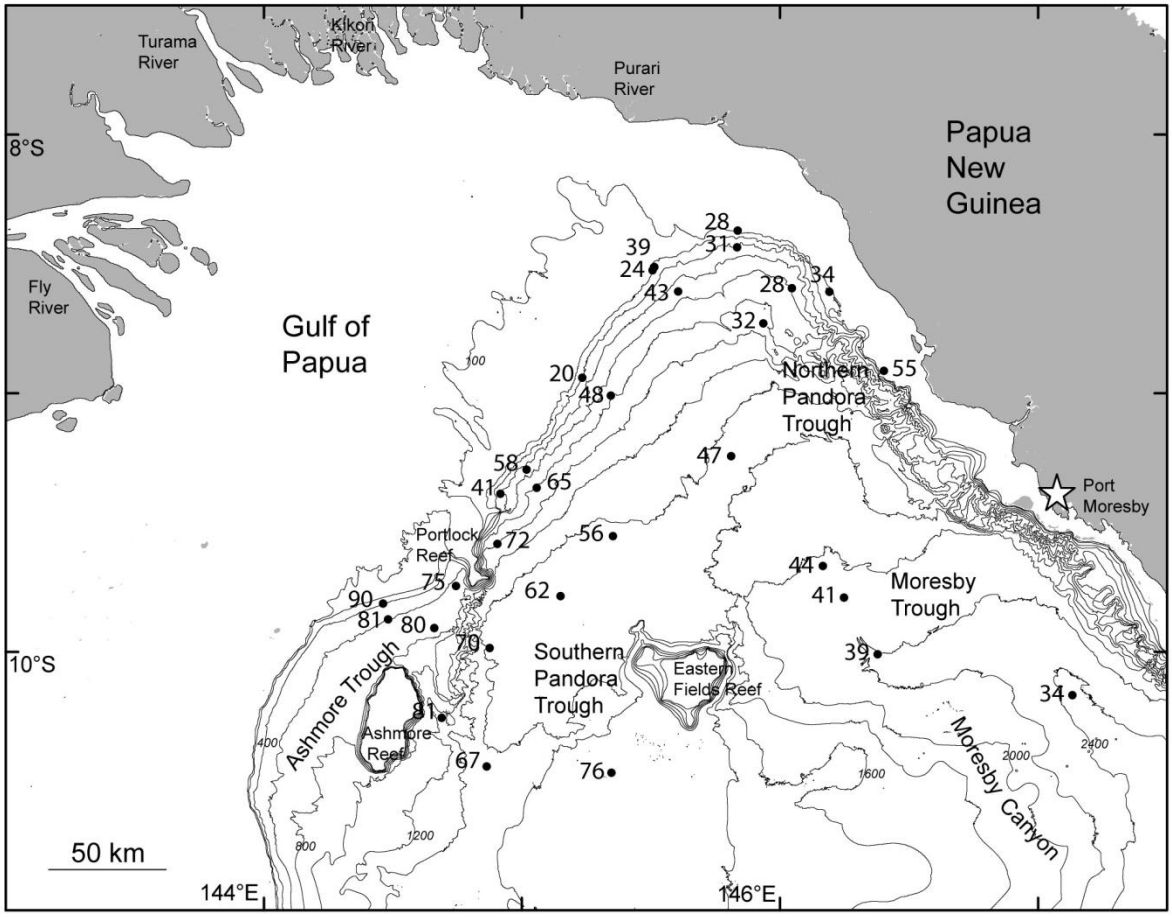

Figure 2.6. Map of calcium-carbonate concentrations (% by mass) from core tops, after *Febo et al*. [2006]. Lowest carbonate concentrations occur in the region with the highest sediment accumulation rates, and most enriched ^{210}Pb inventories (i.e., northernmost continental slope).

small area, along the northeast shelf and upper slope of the study area. Possible sources of error include the values of ^{210}Pb accumulation rates, which we acknowledge to be maximum estimates, as well as *MAR* variability in regions we did not sample, or sampled only sparsely.

Using a mass accumulation rate of 0.08 g cm^{-2} y^{-1} over a smaller region (~8,500 km^2), *Walsh and Nittrouer* [2003] estimated a regional accumulation rate of about 6.8×10^6 tonnes of sediment per year, or ~2.3% of the annual terrigenous sediment flux. Considering the uncertainties involved with the above calculations, we consider our results broadly consistent with those of *Walsh and Nittrouer* [2003]. However, we have chosen to exclude areas with

observed sediment accumulation in the Moresby Trough (**Figures 2.2**), due to the small number of cores spanning a large and heterogeneous seafloor region. If that region were included, the total quantity of annual sediment accumulation in the deep basins of the Gulf of Papua would be greater than the above estimates.

2.5.2 ^{210}Pb Fluxes

Inventories of excess ^{210}Pb vary markedly across the GoP, although they generally decrease with increasing water depth (**Figure 2.5**). This spatial variation can be understood by comparing the sources of ^{210}Pb in the region with the fluxes of ^{210}Pb required to support excess ^{210}Pb inventories at steady-state conditions (Equation 2.4).

The primary sources of ^{210}Pb to waters above the shelf break and slope are atmospheric fallout of ^{210}Pb to surface water, and production from decay of ^{226}Ra [*Cochran*, 1982; *Cochran et al.*, 1990]. By comparison, inputs of dissolved ^{210}Pb from rivers are small, mainly because of rapid scavenging of dissolved Pb by suspended sediments [*Benninger*, 1978]. Assuming efficient trapping of river-borne sediments on the inner shelf, the total expected inventory of excess ^{210}Pb deposited on the distal seabed is the sum of the two primary sources mentioned above. We refer to the sum of flux from these two sources as the theoretical flux (*T*).

The mean annual atmospheric flux of ^{210}Pb, measured in rainfall at Townsville, northeastern Australia, between 1964 and 1970, was 0.22 dpm cm^{-2} y^{-1} [*Bonnyman and Molina-Ramos*, 1975]. This average atmospheric ^{210}Pb flux is in good agreement with the ^{210}Pb flux of 0.23 ± 0.07 dpm cm^{-2} y^{-1} reported by *Turekian et al*. [1977] from the same area. However, J. Pfitzner (unpublished data, 2001) measured ^{210}Pb fluxes in rain collections at the Australian Institute of Marine Sciences (Townsville) and reported a ^{210}Pb flux of 0.33 dpm cm^{-2} y^{-1}. We note that temporal and spatial variations in rainfall cause fluctuations in the atmospheric ^{210}Pb

flux, and we use a value of 0.3 dpm cm^{-2} y^{-1} [*Brunskill et al.*, 2003; *Pfitzner et al*., 2004] as representative atmospheric ^{210}Pb flux for our study area.

We did not measure ^{226}Ra activities in the water column from the study area. Consequently, we estimate water-column inventory of ^{226}Ra based on measurements from GEOSECS Station 263 located at 16°40´S; 167°05´W in the southwestern Pacific, integrated over the depth range at each core location. The profile of ^{226}Ra at this station increases to a maximum above 1500 m water depth, decreases below 2000 m, and activity of ^{226}Ra ranges between 6.0 ± 0.7 and 27.3 ± 0.6 dpm 100 kg^{-1} from surface to 2500 m water depth [*Chung and Craig*, 1980]. Water-column generation of ^{210}Pb from ^{226}Ra is calculated as the product of ^{226}Ra water-column inventory and the ^{210}Pb decay constant (assuming negligible loss of the intermediate decay product ^{222}Rn).

For the present discussion, we will define the ratio between the core-calculated flux (F) (Equation 4) and theoretical flux (T) as $R = F/T$. If $R = 1$, then observed inventories are consistent with vertical scavenging of ^{210}Pb from the water-column inventory, whereas values of $R > 1$ suggest focusing or lateral import of ^{210}Pb to the area. Similarly, a value of $R < 1$ indicates lateral export of ^{210}Pb from that area [e.g. *Buesseler et al*., 1985/86; also see *Baskaran and Santschi*, 2002].

The highest values of R occur along the upper slope and shelf edge of the northeastern Pandora Trough, where $R \geq 10$ for six cores in water depths of 90-1100 m, and $R > 5$ for three additional cores in the area (**Figure 2.2**, **Table 1**). In the Ashmore Trough, intermediate values of $2 \leq R \leq 5$ suggest modest enrichment of ^{210}Pb flux with respect to vertical scavenging of in situ production. These cores (MV-10, MV-12, MV-14, and MV-16) were collected seaward of escarpments of Portlock, Boot, and Ashmore reefs. Cores from the Moresby Trough, southwestern Pandora Trough, and the Eastern Plateau display the lowest values of

R ($0.9 \leq R \leq 2$), suggesting that in these areas, approximate equilibrium exists between in-situ water-column production, and seabed inventories. These cores are from the deepest basins, and are the most remote from the shelf edge and escarpments, in our study (**Table 1**, **Figure 2.1**).

One potential source of additional ^{210}Pb is the northern extension of the Coral Sea Current [*Wolanski et al*., 1995], which could provide ^{210}Pb through the process of "boundary scavenging" [*Anderson et al*., 1994; *Moore et al*., 1996; *Baskaran and Santschi,* 2002]. This tropical oceanic water mass is likely to be very low in suspended particulates that could scavenge dissolved ^{210}Pb for export to the seabed. Because GoP is a semi-enclosed basin, circulation is strongly influenced by the bathymetry and the coastal geometry, with substantial transport across depth contours [*Wolanski et al*., 1995; Ogston et al., 2008; Slingerland et al., 2008b]. More abundant biogenic and lithogenic particles found closer to the GoP shelf could thus scavenge this dissolved ^{210}Pb advected from offshore waters, and then the particles could settle to the seabed. Boundary scavenging of ^{210}Pb from such horizontally advected water masses might be further enhanced by along-slope barriers to flow, such as the escarpments surrounding Ashmore Trough (**Figure 2.2**), and, in the northeastern Pandora Trough, the sharp bend in the shelf edge and pronounced steepening of the slope to the southeast (**Figures 2.1**, **2.2**, and **2.7**), the two regions where the greatest relative enrichments of ^{210}Pb flux are observed. G. J. Brunskill and J. Pfitzner (unpublished data, 2006) measured an inventory of excess ^{210}Pb from sediment traps at the base of the continental slope that was 10-20 times the expected atmospheric input plus in-situ decay supply rates, consistent with our core observations and calculations in **Table 2.1**.

An additional potential source of ^{210}Pb to seabed inventories is sediment focusing, as observed in mud deposits off some rivers [e.g., *Bruland et al*., 1974; *Krishnaswami et al*., 1975; *Carpenter et al*., 1981; Buesseler et al., 1985/86; *Thorbjarnarson et al*., 1986; *Smoak et al*.,

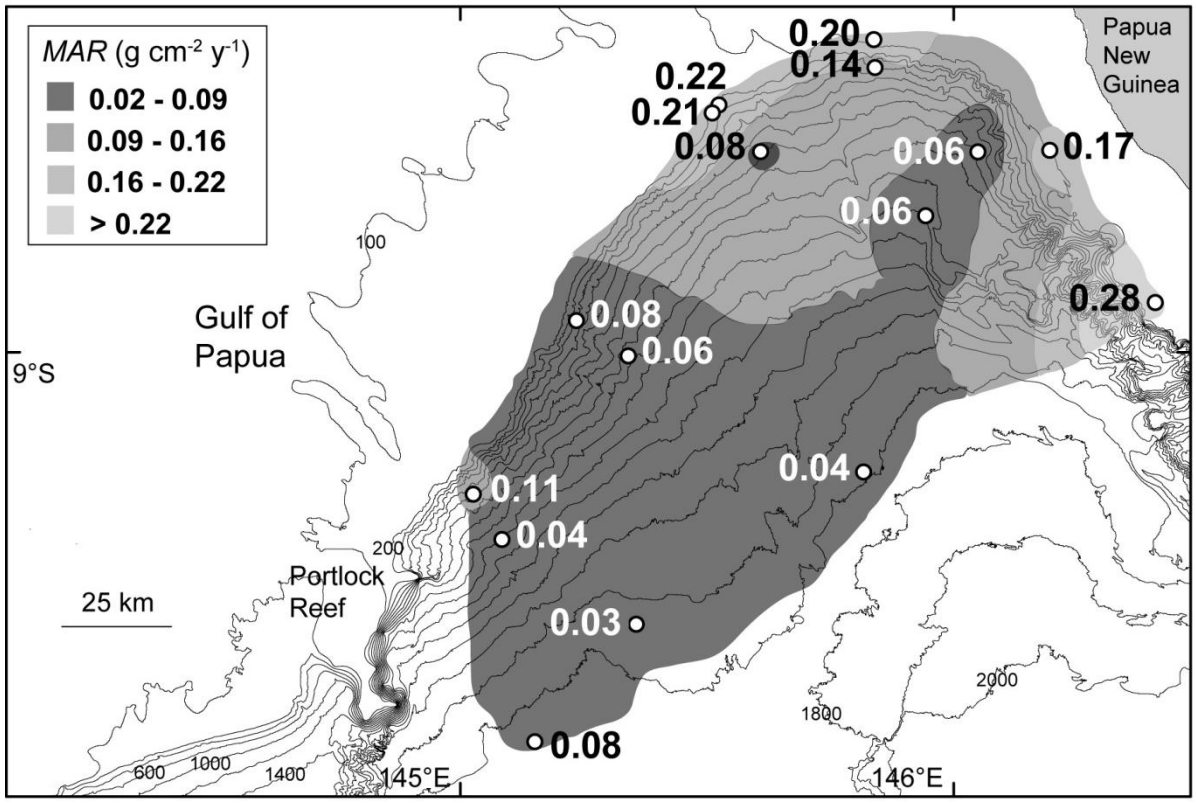

Figure 2.7. Pandora Trough sediment budget using *MAR* values divided into 4 regions. *MAR* values decrease with increasing water depth and reflect hemipelagic sedimentation seaward of the upper slope.

1996; *Kuehl et al.*, 2004]. Inventories of ^{210}Pb and *SAR* tend to display positive correlations in these settings, producing sediment depocenters with ^{210}Pb inventories elevated above values expected from the theoretical vertical flux. Sediment focusing is probably a factor in the northeast Pandora Trough (where *SARs* are relatively high), more so than in the Ashmore Trough (where *SARs* are very low). If *in situ* decay of ^{226}Ra in the water column is a dominant source of ^{210}Pb, inventories would be expected to increase progressively offshore, assuming accumulation rates were uniform. Therefore, from the Pandora Trough into the deeper Moresby Trough, the observed relative downslope decrease in estimated ^{210}Pb fluxes is interpreted to reflect a similar decrease in apparent sediment accumulation rates, resulting from sediment focusing and retention along the shelf edge.

On the basis of recent studies, bathymetric data, and seismic profiles of the shelf and troughs [e.g. *Febo et al*., 2008; *Francis et al*., 2008; *Patterson et al*., 2006; this study], the primary source of siliciclastic material for both Pandora and Moresby troughs appears to originate from the northeastern corner of the GoP. For example, calcium carbonate content in multi-core tops in the GoP illustrate that the lowest carbonate contents (< 45 wt %) are observed on the shelf edge and upper slope of the northeast corner of Pandora Trough (pelagic production of carbonate), and along a channel in Moresby Trough (**Figure 2.6**) [*Febo et al.*, 2006]. In contrast, calcium carbonate exceeds 55-60% in the southwestern Pandora Trough and amounts to as much as 90% in the northern Ashmore Trough (sources of both neritic and pelagic carbonate) (**Figure 2.6**). This pattern is generally consistent with sediment focusing in the northeastern Pandora Trough and decreasing siliciclastic particle flux towards the carbonate-dominated Ashmore Trough (**Figures 2.6** & **2.8**). The most likely source of this sediment is the aforementioned extensive subaqueous clinoform of the GoP inner shelf (**Figure 2.1**), produced by fluvial sediment discharged from the Fly, Kikori, and Purari rivers, among others [*Walsh et al*., 2004]. The shelf-edge depocenter, described above near locations of cores MV-42 and MV-47 is probably fed by oceanic transport of inner-shelf sediment from the northwest. Sediment accumulation near the shelf edge and steep upper slope may lead to episodic production of turbidity flows that move downslope, towards the channel in the Moresby Trough, as recorded in cores MV-24 (**Figure 2.2**) and MV-22 [*Patterson et al.*, 2006].

A network of submarine channels in the Pandora and Moresby troughs, capable of delivering gravity-driven flows from the shelf edge to deeper basins, is shown in **Figure 2.8**, along with values of *R* for individual cores (**Table 2.1**). The channel network [from *Patterson et al*., 2006] was extracted from the bathymetric grid of *Daniell* [2008] using RiverTools© software (RIVIX LLC) for DEM analysis. The resulting channel network identifies potential

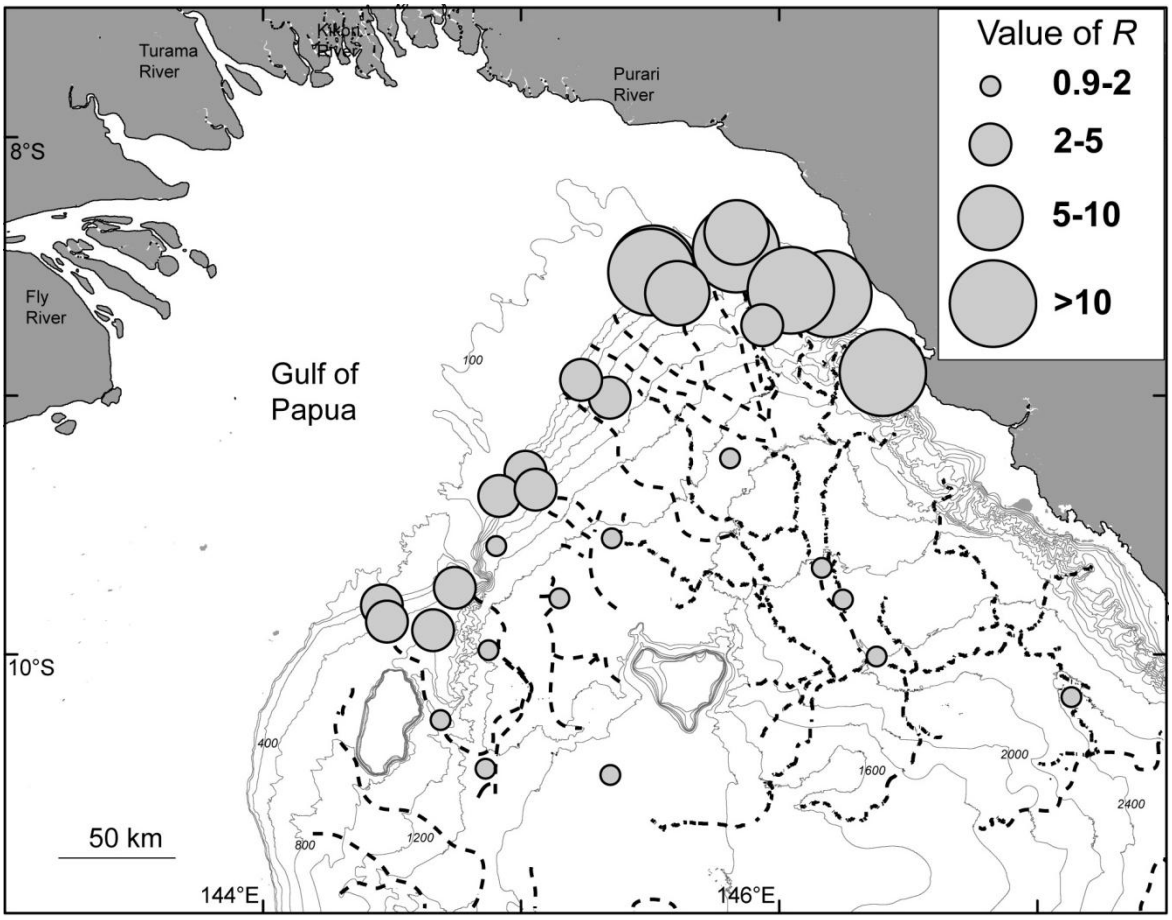

Figure 2.8. Map of relative enrichment in excess ^{210}Pb inventories from Equation 5 and Table 1, showing submarine channel network derived from DEM analysis (channel network data from *Patterson et al*. [2006] with permission). The largest dots indicate highest relative levels of ^{210}Pb enrichment, primarily on the shelf edge and upper slope of the northeast GoP. Patterns of ^{210}Pb enrichment and channel networks outline important sediment transport pathways from the shelf edge to deep basins.

pathways for sediment transport that link the locations of cores MV-42, MV-47, and MV-24, among others, and gives a representation of possible flow pathways in shelf and slope settings where particles may move into the basin by gravity-flow transport [*Bird et al.*, 1995].

2.5.3 A Sediment Transport Scenario

Sediment focusing and boundary scavenging of oceanic ^{210}Pb are both likely sources for producing elevated ^{210}Pb inventories on the shelf break and upper slope. Both processes are probably active in the northeastern Pandora Trough, but boundary scavenging is probably

dominant to the southwest, in regions of lower suspended-sediment flux. Spatial distribution of ^{210}Pb flux observed at the seabed can be attributed to downslope and lateral particle transport and variation in bottom topography. This phenomenon has been observed in a number of continental-slope environments, e.g.: Quinault Canyon [*Carpenter et al.*, 1981; *Thorbjarnarson et al.*, 1986], California margin [*Huh et al*., 1990; *Alexander and Venherm*, 2003] and the eastern and southeastern US continental margin [*Biscaye et al*., 1988; *DeMaster et al*., 1991]. A certain proportion of particles may be transported from shelf to open-slope waters and then down slope, and the rest may be carried by alongshelf currents to canyon heads, settling into canyons, thus facilitating down-canyon transport [e.g. *Biscaye and Anderson*, 1994].

The northeastern GoP shelf edge is marked by several locations that could be major escape routes for sediments from the shelf to deeper basins (**Figure 2.8**; see **Figure 2.1** for core locations). For example, cores MV-18 and 19 are situated at the head of an intraslope canyon as shown by analysis of seafloor bathymetries and channel networks (**Figures 2.2** and **2.8**). Further, the highest measured excess ^{210}Pb inventory from this study is located at MV-18, along with low surficial calcium-carbonate content (**Figures 2.6** and **2.8**). Cores MV-42 and MV-47 also occur along a channel extending from shelf to basin, and both cores exhibit enriched ^{210}Pb inventories and relatively high *SAR*. Farther down the same channel network, core MV-50 (795 m water depth) exhibits the same characteristics, suggestive of sediment focusing and downslope transport. Combined seafloor bathymetry and radionuclide data thus suggest that these locations are major conduits for sediment supply to deeper basins. These observations, combined with evidence from core MV-24, further suggest that sediment transport occurs in both nepheloid layers and turbidity flows.

2.6 Conclusions

Examination of ^{210}Pb activities on the continental margin and basin of the GoP has given some insight into the behavior of ^{210}Pb and the processes that control sediment transfer on the continental margin. Patterns of sediment accumulation (0.05-0.35 cm y^{-1}; 0.05-0.28 g cm^{-2} y^{-1}) and inventory-derived ^{210}Pb fluxes (1-12.8 dpm cm^{-2} y^{-1}) display regional variations, decreasing seaward, and along isobaths away from the northeastern shelf edge. The amount of terrigenous sediment load being discharged annually from the shelf and accumulating in Pandora Trough is approximately 7-14×10^6 tonnes, generally consistent with previous findings. However, the existence of possible turbidity-current transport and deposition have been documented in a deep basin, Moresby Trough, suggesting that additional downslope export and sediment accumulation may be occurring in deeper parts of the Coral Sea. High excess ^{210}Pb fluxes estimated from seabed inventories at the shelf break and upper slope are consistent with the combined effects of sediment focusing and boundary scavenging of oceanic water masses. Sediments may be transported from inner-shelf depocenters by oceanic processes, focused in depocenters near the northeastern GoP shelf edge, and distributed downslope through a combination of nepheloid-layer flow and possible turbidity-currents.

2.7 References

Alexander, C. R., and C. Venherm (2003), Modern sedimentary processes in the Santa Monica, California continental margin: sediment accumulation, mixing and budget, *Mar. Environ. Res.*, *56*, 177– 204.

Anderson, R. F., M. Q. Fleischer, P. E. Biscaye, N. Kumar, B. Dittrich, P. Kubik, and M. Suter (1994), Anomalous boundary scavenging in the Middle Atlantic Bight: evidence from ^{230}Th, ^{231}Pa, 10Be and ^{210}Pb, *Deep Sea Res., Part II*, *41*, 537–561.

Appleby, P. G., and F. Oldfield (1992), Application of lead-210 to sedimentation studies, in *Uranium-Series Disequilibria: Applications to Earth, Marine, and Environmental Sciences*, edited by M. Ivanovich and R. S. Harmon, pp. 731– 778, Clarendon, Oxford, U.K.

Baskaran, M., and P. H. Santschi (2002), Particulate and dissolved 210Pb activities in the shelf and slope regions of the Gulf of Mexico waters, *Cont. Shelf Res.*, *22*, 1493–1510.

Benninger, L. K. (1978), ^{210}Pb balance in Long Island Sound, *Geochim. Cosmochim. Acta*, *42*, 1165–1174.

Benninger, L. K., R. C. Aller, J. K. Cochran, and K. K. Turekian (1979), Effects of biological sediment mixing on the ^{210}Pb chronology and trace metal distribution in a Long Island sound sediment core, *Earth Planet. Sci. Lett.*, *43*, 241–259.

Bentley, S. J., Z. Muhammad, L. J. Patterson, A.W. Droxler, G. R. Dickens, L. C. Peterson, and B. N. Opdyke (2006a), Modern and Pleistocene turbidite sedimentation in the Gulf of Papua S2S study area: Implications for modulation of sediment sources by oceanic and climatic processes, paper presented at 2006 Annual Convention, Am. Assoc. of Pet. Geol., Houston, Tex., 9 –12 April.

Bentley, S. J., A. Sheremet, and J. M. Jaeger (2006b), Bioturbation, event sedimentation, and preserved sedimentary fabric: Field and model comparisons in three contrasting marine settings, *Cont. Shelf Res.*, *26*, 2108–2124.

Bird, M. I., G. J. Brunskill, and A. R. Chivas (1995), Carbon isotope composition of sediments from the Gulf of Papua, *Geo Mar. Lett.*, *15*, 153– 159.

Biscaye, P. E., and R. F. Anderson (1994), Fluxes of particulate matter on the slope of the southern Middle Atlantic Bight: SEEP-II, *Deep Sea Res., Part II*, *41*, 459– 509.

Biscaye, P. E., R. F. Anderson, and B. L. Deck (1988), Fluxes of particles and constituents to the eastern United States continental slope and rise: SEEP-I, *Cont. Shelf Res.*, *8*, 855– 904.

Bonnyman, J., and J. Molina-Ramos (1975), Concentrations of lead-210 in rainwater in Australia during the years 1964– 1970, Commonwealth X-ray and Radium Lab., Dep. of Health, Melbourne, Australia.

Bruland, K. W., M. Koide, and E. D. Goldberg (1974), The comparative marine geochemistries of lead-210 and radium-226, *J. Geophys. Res.*, *79*, 3083– 3086.

Brunskill, G. J., K. J. Woolfe, and I. Zagorskis (1995), Distribution of riverine sediment chemistry on the shelf, slope, and rise of the Gulf of Papua, *Geo Mar. Lett.*, *15*, 160–165.

Brunskill, G. J., I. Zagorskis, and J. Pfitzner (2003), Geochemical mass balance for lithium, boron, and strontium in the Gulf of Papua, Papua New Guinea (Project TROPICS), *Geochim. Cosmochim. Acta*, *67*, 3365– 3383.

Buesseler, K. O., H. D. Livingston, and E. R. Sholkovitz (1985), ^{239,240}Pu and excess ^{210}Pb inventories along the shelf and slope of the northeast U.S.A., *Earth Planet. Sci. Lett.*, *76*, 10–22.

Carpenter, R., J. T. Bennett, and M. L. Peterson (1981), ^{210}Pb activities in and fluxes to sediments of the Washington continental slope and shelf, *Geochim. Cosmochim. Acta*, *45*, 1172–1981.

Chung, Y., and H. Craig (1980), ^{226}Ra in the Pacific Ocean, *Earth Planet. Sci. Lett., 49,* 267–292.

Cochran, J. K. (1982), The oceanic chemistry of the U-and Th-series nuclides, in *Uranium Series Disequilibrium: Applications to Environmental Problems*, edited by M. Ivanovich and R. S. Harmon, pp. 384– 430, Clarendon, Oxford, U.K.

Cochran, J. K., T. McKibbin-Vaughan, M. M. Dornblaser, D. Hirschberg, H. D. Livingston, and K. O. Buesseler (1990), ^{210}Pb scavenging in the North Atlantic and North Pacific oceans, Earth *Planet. Sci. Lett., 97,* 332– 352.

Cutshall, N. H., I. L. Larsen, and C. R. Olsen (1983), Direct analysis of Pb-210 in sediment samples: Self-absorption corrections, *Nucl. Instrum. Methods Phys. Res., 206,* 309– 312.

Daniell, J. J. (2008), Development of a bathymetric grid for the Gulf of Papua and adjacent areas: A note describing its development, *J. Geophys. Res., 113*, F01S15, doi:10.1029/2006JF000673.

DeMaster, D. J., D. C. Brewster, B. A. McKee, and C. A. Nittrouer (1991), Rates of particle scavenging, sediment reworking, and longitudinal ripple formation at the HEBBLE site based on measurements of ^{234}Th and ^{210}Pb, *Mar. Geol., 99,* 423– 444.

Ewing, J. I., R. E. Houtz, andW. J. Ludwig (1970), Sediment distribution in the Coral Sea, *J. Geophys. Res., 75,* 1963– 1972.

Febo, L. A., S. J. Bentley, G. R. Dickens, A. W. Droxler, L. C. Peterson, and B. N. Opdyke (2006), Recent to late Pleistocene sedimentary organic matter in the Gulf of Papua, poster presented at 2006 Annual Convention, Am. Assoc. of Pet. Geol., Houston, Tex., 9 –12 April.

Febo, L. A., S. J. Bentley, J. H. Wrenn, A. W. Droxler, G. R. Dickens, L. C. Peterson, and B. Opdyke (2008), Late Pleistocene and Holocene sedimentation, organic carbon delivery, and paleoclimatic inferences on the continental slope of the northern Pandora Trough, Gulf of Papua, *J. Geophys. Res.*, doi:10.1029/2006JF000677.

Francis, J. M., J. Daniell, A. W. Droxler, G. R. Dickens, S. J. Bentley, L. C. Peterson, B. N. Opdyke, and L. Beaufort (2008), Deep-water geomorphology of the mixed siliciclastic-carbonate system, Gulf of Papua, *J. Geophys. Res.*, doi:10.1029/2007JF000851.

Goldberg, E. D., and M. Koide (1962), Geochronological studies of deep sea sediments by the ionium/thorium method, *Geochim. Cosmochim. Acta, 26,* 417– 450.

Harris, P. T., E. K. Baker, A. R. Cole, and S. A. Short (1993), Preliminary study of sedimentation in the tidally dominated Fly River Delta, Gulf of Papua, *Cont. Shelf Res., 13,* 441–472.

Harris, P. T., C. B. Pattiaratchi, J. B. Keene, R. W. Dalrymple, J. V. Gardner, E. K. Baker, A. R. Cole, D. Mitchell, P. Gibbs, and W. W. Schroeder (1996), Late Quaternary deltaic and carbonate sedimentation in the Gulf of Papua foreland basin: Response to sea-level change, *J. Sediment. Res., 66*, 801– 819.

Huh, C. A., L. F. Small, S. Niemnil, B. P. Finney, B. M. Hickey, N. B. Kachel, D. S. Gorsline, and P. M. Williams (1990), Sedimentation dynamics in the Santa Monica-San Pedro basin off Los Angeles: Radiochemical, sediment trap and transmissometer studies, *Cont. Shelf Res., 10*, 137– 164.

Koide, M., A. Soutar, and E. D. Goldberg (1972), Marine geochronology with ^{210}Pb, *Earth Planet. Sci. Lett., 14*, 442– 446.

Krishnaswami, S., B. L. K. Somayajulu, and Y. Chung (1975), ^{210}Pb/^{226}Ra disequilibrium in the Santa Barbara Basin, *Earth Planet. Sci. Lett., 27*, 388–392.

Krishnaswami, S., L. K. Benninger, R. C. Aller, and K. L. Vondamm (1980), Atmospherically-derived radionuclides as tracers of sediment mixing and accumulation in near-shore marine and lake sediments: Evidence from Be-7, Pb-210, and Pu-239, Pu-240, *Earth Planet. Sci. Lett., 47*, 307–318.

Kuehl, S. A., D. J. DeMaster, and C. A. Nittrouer (1986), Nature of sediment accumulation on the Amazon continental shelf, *Cont. Shelf Res., 6*, 209–225.

Kuehl, S. A., G. J. Brunskill, K. Burns, D. C. Fugate, and T. Kniskern (2004), Nature of sediment dispersal off the Sepik River, Papua New Guinea: Preliminary sediment budget and implications for margin processes, *Cont. Shelf Res., 24*, 2417–2429.

Milliman, J. D. (1995), Sediment discharge to the ocean from small mountainous rivers: the New Guinea example, *Geo Mar. Lett., 15*, 127–133.

Milliman, J. D., K. L. Farnsworth, and C. S. Albertin (1999), Flux and fate of fluvial sediments leaving large islands in the East Indies, *J. Sea Res., 41*, 97–107.

Moore, W. S., D. J. DeMaster, J. M. Smoak, B. A. McKee, and P. W. Swarzenski (1996), Radionuclide tracers of sediment-water interactions on the Amazon shelf, *Cont. Shelf Res., 16*, 645–665.

Nittrouer, C. A., R. W. Sternberg, R. Carpenter, and J. T. Bennett (1979), Use of Pb-210 geochronology as a sedimentological tool: Application to the Washington continental-shelf, *Mar. Geol., 31*, 297–316.

Nittrouer, C. A., D. J. DeMaster, B. A. McKee, N. H. Cutshall, and I. L. Larsen (1984), The effect of sediment mixing on Pb-210 accumulation rates for the Washington continental shelf, *Mar. Geol., 54*, 201– 221.

NSF MARGINS Office (2004), NSF MARGINS Program science plans, 170 pp., Lamont-Doherty Earth Obs., Columbia Univ., Palisades, N. Y.

Ogston, A. S., R. W. Sternberg, C. A. Nittrouer, D. P. Martin, M. A. Goñi, and J. S. Crockett (2008), Sediment delivery from the Fly River tidally dominated delta to the nearshore marine environment and the impact of El Niño, *J. Geophys. Res., 113,* F01S11, doi:10.1029/2006JF000669.

Patterson, L. J., S. J. Bentley, D. H. Henry, G. R. Dickens, A. W. Droxler, L. C. Peterson, and B. N. Opdyke (2006), Petrological and geochemical investigations of deep sea turbidite sands in the Pandora and Moresby troughs, source to sink Papua New Guinea focus area, poster presented at 2006 Annual Convention, Am. Assoc. of Pet. Geol., Houston, Tex., 9 – 12 April.

Pfitzner, J., G. Brunskill, and I. Zagorskis (2004), ^{137}Cs and excess ^{210}Pb deposition patterns in estuarine and marine sediment in the central region of the Great Barrier Reef Lagoon, north-eastern Australia, *J. Environ. Radioact., 76,* 81–102.

Pickup, G. (1984), Geomorphology of tropical rivers: I. Landforms, hydrology, and sedimentation in the Fly and lower Purari, Papua New Guinea, *Catena Suppl., 5,* 18–41.

Slingerland, R. L., N. W. Driscoll, J. D. Milliman, S. R. Miller, and E. A. Johnstone (2008a), Anatomy and growth of a Holocene clinothem in the Gulf of Papua, *J. Geophys. Res.,* doi:10.1029/2006JF000628.

Slingerland, R., R. Selover, A. Ogston, T. R. Keen, N.W. Driscoll, and J. D. Milliman (2008b), Building the Holocene clinothem in the Gulf of Papua: An ocean circulation study, *J. Geophys. Res.,* doi:10.1029/2006JF000680.

Smoak, J. M., D. J. DeMaster, S. A. Kuehl, R. H. Pope, and B. A. McKee (1996), The behavior of particle-reactive tracers in a high turbidity environment: ^{234}Th and ^{210}Pb on the Amazon continental shelf, *Geochim. Cosmochim. Acta, 60,* 2123–2137.

Thomson, J., S. Colley, and P. P. E. Weaver (1988), Bioturbation into a recently emplaced deep-sea turbidite surface as revealed by $^{210}Pb_{excess}$, $^{230}Th_{excess}$ and planktonic foraminifera distribution, *Earth Planet. Sci. Lett., 90,* 157–173.

Thorbjarnarson, K. W., C. A. Nittrouer, and D. J. DeMaster (1986), Accumulation of modern sediment in Quinault submarine canyon, *Mar. Geol., 71,* 107– 124.

Turekian, K. K., Y. Nozaki, and L. K. Benninger (1977), Geochemistry of atmospheric radon and radon products, *Annu. Rev. Earth Planet. Sci., 5,* 227– 255.

Walsh, J. P., and C. A. Nittrouer (2003), Contrasting styles of off-shelf sediment accumulation in New Guinea, *Mar. Geol., 196,* 105– 125.

Walsh, J. P., and C. A. Nittrouer (2004), Mangrove-bank sedimentation in a mesotidal environment with large sediment supply, Gulf of Papua, *Mar. Geol., 208,* 225– 248.

Walsh, J. P., C. A. Nittrouer, C. M. Palinkas, A. S. Ogston, R. W. Sternberg, and G. J. Brunskill (2004), Clinoform mechanics in the Gulf of Papua, New Guinea, *Cont. Shelf Res., 24,* 2487–2510.

Winterer, E. L. (1970), Submarine valley systems around Coral-Sea basin (Australia), *Mar. Geol.*, *8*, 229– 244.

Wolanski, E., and D. M. Alongi (1995), A hypothesis for the formation of a mud bank in the Gulf of Papua, *Geo Mar. Lett.*, *15*, 166– 171.

Wolanski, E., A. Norro, and B. King (1995), Water circulation in the Gulf of Papua, *Cont. Shelf Res.*, *15*, 185– 212.

Wolanski, E., R. J. Gibbs, S. Spagnol, B. King, and G. Brunskill (1998), Inorganic sediment budget in the mangrove-fringed Fly River Delta, Papua New Guinea, *Mangroves Salt Marshes*, *2*, 85–98.

CHAPTER 3
PARTICLE MIXING RATES ON THE SHELF AND SLOPE SEDIMENTS OF THE GULF OF PAPUA

3.1 Introduction

Once sediments are deposited at the seabed, sedimentary strata are formed that may undergo alteration. This alteration of the sedimentary strata may be physical and/or biological in origin [*Moore and Scruton,* 1957; *Nittrouer and Sternberg,* 1981]. The sedimentary stratigraphic record can be greatly influenced by the movement of benthic fauna living in the upper few centimeters of the seabed [*Wheatcroft*, 1990; *Bromley*, 1996]. Termed bioturbation, the organisms can create distinction structures and suites of structures (trace fossils, lebenspurren, ichnofacies, etc.) that provide information about the depositional environment. When sufficiently intense, bioturbation causes a diffusion-like (biodiffusion) movement of sedimentary components downward into the sediment column from the sediment-water interface.

The natural radioactive tracer, ^{210}Pb (half life ~22years) of the ^{238}U decay series, is introduced into the environment from the decay of ^{222}Rn in the atmosphere [*Cochran,* 1982]. This ^{210}Pb is deposited at the seabed in continental margins as unsupported ^{210}Pb and scavenged by particles. In deep waters, the main source of excess ^{210}Pb is dissolved ^{226}Ra, a product of Uranium-series decay [*Cochran,* 1982]. Once deposited at the seabed, ^{210}Pb adhering to the particles can be transported downward into sediments. The distribution of ^{210}Pb in marine sediments, can therefore, be used to assess particle mixing rates [e.g. *Henderson and Anderson*, 2003].

The upper few centimeters of sediment is the region where this mixing is intense because of the availability of detrital food, and the gradients of oxygen and the products of anaerobic respiration restrict the distribution of metazoans [*e.g. Smith et al.,* 1993]. The burrowing, excavation, sediment ingestion and egestion of the benthic fauna are collectively termed

bioturbation. In many instances bioturbation results in discrete sedimentary structures and suites of structures variously termed trace fossils, lebenspurren, ichnofacies, etc. When sedimentation rates, however, are slow relative to the lifespan of benthic organisms, biological traces become self erasing [*Wheatcroft et al*., 1989]. In such cases the net biological displacement of sediment components is manifested as a downward diffusion into the sediment column, biodiffusion. In some cases, ingestion/egestion behavior of certain populations can cause subsurface sediments to be mixed more rapidly than those at the sediment-water interface [*Rhoads and Young*, 1970; *Rice*, 1986; *Boudreau and Imboden*, 1987; *Legeleux et al*., 1994]. A decrease in mixing with depth, however, is more typical. Sediment mixing by these benthic communities can have a profound effect on the sediment cycling of nutrients and flux of carbon to the continental shelf and slope [e.g. *Alperin et al*., 2002; *Burdige*, 2006] and can alter the distribution of tracers used for sediment studies. The rates and depths of mixing can be determined on different time scales by radioactive tracers which are supplied to the seabed through the water column.

The primary approach to constrain patterns of bioturbation is by using models to evaluate patterns of vertical profiles of ^{210}Pb. This radionuclide reflects sedimentary processes occurring on continental margins on 100-year timescale and has been used to quantify sediment accumulation and bioturbation rates. The depth distribution of excess ^{210}Pb activity at the seabed can be used to interpret physical and biological processes. The profile generally consists of an upper region of mixing and a lower region of steady-state accumulation [*Nittrouer et al*., 1979]. *Santschi et al*., [1980] used a numerical model and noted that bioturbation was higher in the surface layer and lower in the lower layer in shelf sediments. *Carpenter et al*., [1982] noted that sediment accumulation rates can be overestimated due to bioturbation/mixing in shelf sediments. However, *DeMaster et al*., [1985] found that particle mixing may be underestimated using steady-state solutions. Mixing intensity in a given marine environment may be related to

abundance of benthic fauna, organic carbon flux and primary productivity [*Legeleux et al*., 1994]. *Bentley et al*., [2006] have shown that episodic sedimentation and depth-dependent bioturbation as important competing factors in the preservation or destruction of primary depositional fabric. In deep waters, the rate of sediment accumulation is slow; however, this radioisotope can yield information about deep sea bioturbation rates [*Nozaki et al*., 1977; *Suckow et al*., 2001]. *Muhammad et al*., [2008] have measured excess ^{210}Pb seabed inventories to estimate ^{210}Pb flux in shelf and slope environments and to infer sediment transport pathways from shelf to slope.

3.2 Background

3.2.1 The Study Area

The distribution of sedimentary facies in the GoP indicates that most of the mud and organic detritus exiting from the major rivers deposits as a narrow band along the inner shelf [*Alongi et al*., 1992; *Alongi and Robertson*, 1995; *Walsh and Nittrouer*, 2003; *Keen et al*., 2006]. Sediments on the outer shelf consist of lithogenic and carbonate sands [*Brunskill et al*., 1995; see also *Slingerland et al*., 2008] and the detrital fraction in sediments decreases with increasing water depth [*Febo*, 2007]. The three major areas of sediment deposition in the GoP are Pandora, Ashmore and Moresby Troughs (**Figure 3.1**). The shelf edge of Pandora Trough is semicircular with scalloped morphology and thick prograding sedimentary packages up to 20 m thick in the north and a smooth, flat sea floor towards the south which is connected to the Moresby Trough [*Patterson*., 2006; *Francis et al*., 2008; *Muhammad et al*., 2008]. The Ashmore Trough is located between the eastern slope of Great Barrier Reef and the western slope of Ashmore-Boot-Portlock Reef complex. The seafloor of the Ashmore Trough deepens towards the east-southeast along the toe of the western slope of the Ashmore-Boot-Portlock Reef complex. The smooth bathymetry of the lower slope and seafloor of the Ashmore Trough is dominated by pelagic and hemipelagic

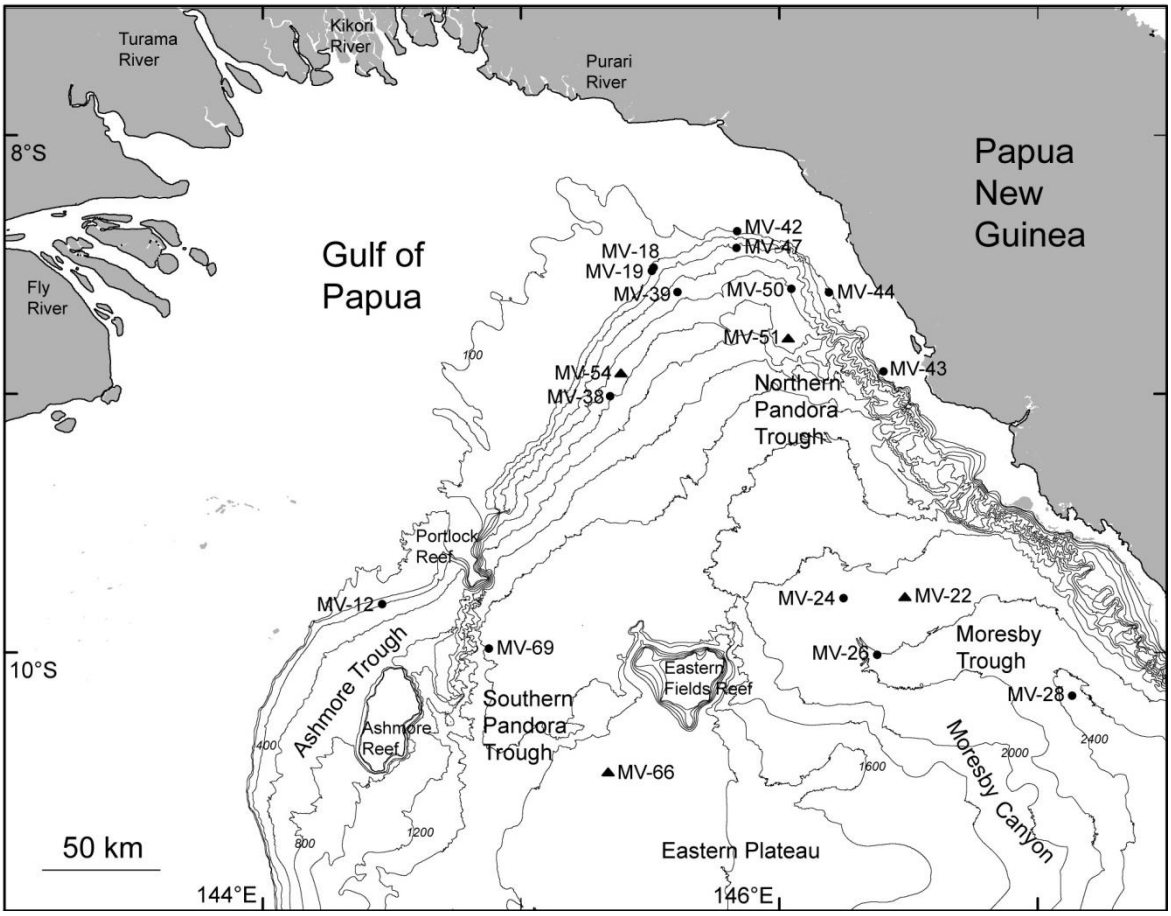

Figure 3.1 Study area showing core locations. Black dots represent multicores from this study while black triangles show piston cores from *Febo et al*., [2008] and *Patterson*, [2006]. Contours are in meters.

sedimentation [*Francis et al*., 2008]. The Moresby Trough is connected to the Pandora Trough in the north and has a narrow shelf on the eastern side varying in width from 10 km to 30 km [*Francis et al*., 2008]. The bathymetry of the Moresby Trough is dominated by a channel which trends southeast into the Moresby Canyon [*Winterer*, 1970; *Francis et al*., 2008].

Sediment dispersal from river to shelf to slope is strongly influenced by the ocean current regime. The GoP experiences two dominant wind-driven currents influenced by seasonal monsoon and trade winds [*Wolanski et al.*, 1995; *Walsh et al*., 2004]. The monsoon season winds from northwest last from December to March and are generally weak (1–2 m s^{-1}) [*Slingerland et*

al., 2008]. During this relatively calm weather with limited fetch, the sediment from the rivers settles out on the inner shelf because the tidal currents are too weak to resuspend the sediment [*Wolanski and Alongi*, 1995]. Trade winds during May to October are strong (4–5 m s^{-1}), sustained, and from the southeast and with a large fetch over the GoP [*Walsh et al*., 2004; *Slingerland et al*., 2008]. During the strong southeast trade winds, sediment from the rivers is resuspended by wave action and prevailing currents can carry some mud southeastward beyond the slope in deeper waters [*Wolanski and Alongi*, 1995].

3.2.2. Assessing Biodiffusion

Biodiffusion is the result of small random movements of sediment over very short timescales, mimicking diffusion. Strictly speaking, mixing of sediments by different animals is not diffusive, but for modeling purposes, diffusion is a conservative and appropriate approximation [*Wheatcroft*, 1990; also see *Wheatcroft et al*., 1990]. In this chapter, we refine estimates of sediment accumulation rates based on assessment of biodiffusion on the observed ^{210}Pb profiles in sediment cores taken from the Gulf of Papua (GoP) shelf and slope during the PANASH cruise [*Muhammad et al*., 2008].

3.3 Methods

A multicorer was used to collect samples from the shelf and slope regions of the northern GoP during the PANASH cruise of the R/V *Melville* during March–April 2004 [*Muhammad et al*., 2008] (**Figure 3.1**). Down-core variability of textural characteristics was analyzed by taking X-radiographs of cores during the cruise and by post-cruise analyses that included grain size and radioisotopic measurements [*Muhammad et al*., 2008]. For grain size and radioisotopic analyses, cores were subsampled at 1 cm interval for the top 6 cm and 2 cm interval below 6 cm to the base.

3.3.1 Analyses

Cores were imaged onboard using a Thales Flashscan 35 digital X-ray detector panel, illuminated with a Medison Acoma PX15HF X-ray generator. Images were archived as 14-bit-gray scale images with 127 μm pixel resolution [*Muhammad et al*. 2008]. Cores were then shipped to Rosenstiel School of Marine and Atmospheric Science (RSMAS), University of Miami, repository for post-cruise analyses.

Grain size measurements were performed at 1-cm and 2-cm intervals from subsamples obtained from multicores. Subsamples were disaggregated with 0.05 % sodium hexametaphosphate solution followed by immersion in an ultrasonic bath. Granulometric measurements were carried out on cores MV-12, MV-24, MV-26, MV-28, MV-38, MV-39, MV-42, MV-43, MV-44, MV-47, MV-50, MV-69 using a Micromeritics 5100 Sedigraph following the methods of *Coakley and Syvitski* [1991]. Cores MV-18 and MV-19 were analyzed for grain size by wet-sieving at 63 μm and drying at 60°C for 24-hr to determine weight percent of sand and mud. Grain size analyses were undertaken to identify changes in particle size that could influence distributions of ^{210}Pb activity, as large grain size is associated with low excess ^{210}Pb activity [e.g. *Bentley et al*., 2002].

Samples for ^{210}Pb measurements were counted for 24 hours on Canberra low-background planar gamma detectors using the method of *Cutshall et al.* [1983] to correct for self-absorption [*Muhammad et al*., 2008]. Total ^{210}Pb for each interval was determined by measurement of the 46.5 keV ^{210}Pb gamma peak from which excess (unsupported) ^{210}Pb was determined by subtracting total ^{210}Pb activity from supported ^{210}Pb activity. Supported ^{210}Pb from the decay of its parent, ^{226}Ra (half life ~ 1.6 ky) in sediments, was determined by measurement of the granddaughters of ^{226}Ra, ^{214}Pb (at 295 and 352 keV) and ^{214}Bi (at 609 keV). The minimum detection limit for excess ^{210}Pb was 1 dpm g^{-1}.

Cruise duration and shipping time for the samples from offshore to the laboratory did not allow analyses of cores for ^{234}Th, which has a half-life of 24 days. In the present study, ^{137}Cs was not detectable above the detection limit of 0.05 dpm g^{-1} in our detectors.

3.4 Results

3.4.1 Particle Mixing Numerical Model Development

Particle mixing rates can be determined from one-dimensional, steady state models developed using the general diagenetic equation (1) [*Goldberg and Koide*, 1962; *Berner*, 1980]. The model used in the present study assumes steady-state conditions of sediment accumulation and biodifussion. This numerical model is used here to evaluate possible scenarios in the sedimentary environment which could result in a given profile of excess ^{210}Pb activity at the seabed. Although it is unlikely that these conditions are met in all the cores in the present study, the approach of steady-state is a reasonable choice. The model assumes that the flux of ^{210}Pb in the steady area has been steady on a 100-yr timescale, that ^{210}Pb is bound irreversibly to the particles, and that sediment mixing is analogous to diffusive mixing [e.g. *Alperin et al*., 2002]; the model also does not consider non local mixing [e.g. *Smith et al*., 1986].

In the present study, biodiffusion coefficient values, denoted here as D_b, were estimated using a two-layer numerical model in which the upper layer mixes at a faster rate than the lower layer, i.e. $D_{b1}>D_{b2}$ [e.g. *Benninger et al*., 1979]. The model is used to interpret excess ^{210}Pb profiles in which activities decrease from sediment-water interface downward. The net downward transport of ^{210}Pb could be due to sediment accumulation and/or biodiffusion or a combination of both. The model consists of single sedimentation rate for each profile and two layers of mixing below which there is no mixing of sediments. For a two- layer model, we have the following equations at steady state:

layer 1:

$$\frac{\partial A}{\partial t} = \frac{\partial}{\partial x}(D_{b1}\frac{\partial A}{\partial x}) - S\frac{\partial A}{\partial x} - \lambda A = 0 \quad (1)$$

layer 2:

$$\frac{\partial A}{\partial t} = \frac{\partial}{\partial x}(D_{b2}\frac{\partial A}{\partial x}) - S\frac{\partial A}{\partial x} - \lambda A = 0 \quad (2)$$

where A = activity of excess ^{210}Pb (dpm g^{-1})at any depth, x cm; S = sedimentation rate (cm y^{-1}); D_{b1} and D_{b2} = biodiffusion coefficient for layer 1 and layer 2, respectively (cm^2 y^{-1}); and λ = decay constant for ^{210}Pb = 0.031 y^{-1}.

The two-layer model is an appropriate choice because limited bioturbation of the deeper layer may result in particle flux comparable to that produced by sedimentation/advection. For the upper layer, we hypothesize that $S^2 << 4D_{b1}$ and for the lower layer, $S^2 \sim 4D_{b1}$ or $< 4D_{b1}$ [*Aller*, 1982]. The appropriate boundary conditions at the sediment-water interface ($x = 0$) are $A = A_0$ where A_0 is the excess ^{210}Pb activity of most recently deposited sediment, while the bottom boundary conditions are, $A \rightarrow 0$ as $x \rightarrow \infty$ (in this study, there is no excess ^{210}Pb below the core depths of 40 cm).

Equations (1) and (2) were solved in MATLAB using the finite difference method [*Boudreau*, 1997]. Equation (1) consists of first and second order partial derivatives which are replaced with algebraic difference quotients. In this approach, excess ^{210}Pb activities on the horizontal-axis and core depth on the vertical-axis are broken down into a grid of continuous intervals in which x_i represents an arbitrary depth which corresponds to the i-th point on the grid where excess ^{210}Pb activity is given as A_i. The series of algebraic equations formed can then be solved for the given input parameters at specific grid points. The derivation of those algebraic equations is given below.

The partial derivatives in Equation (1) are represented by linear algebraic equations over a given space domain. Let the depth in core be represented by j and excess ^{210}Pb activity be given by A at some arbitrary point. Consider two points adjacent to j given by j+1 and j-1. Excess ^{210}Pb activity at j+1 is $A_{(j+1)}$ and at j-1 is $A_{(j-1)}$. The mid-points of j+1 and j and j and j-1 are given by j+(1/2) and j-(1/2) respectively, separated by a distance Δx (**Figure 3.2**).

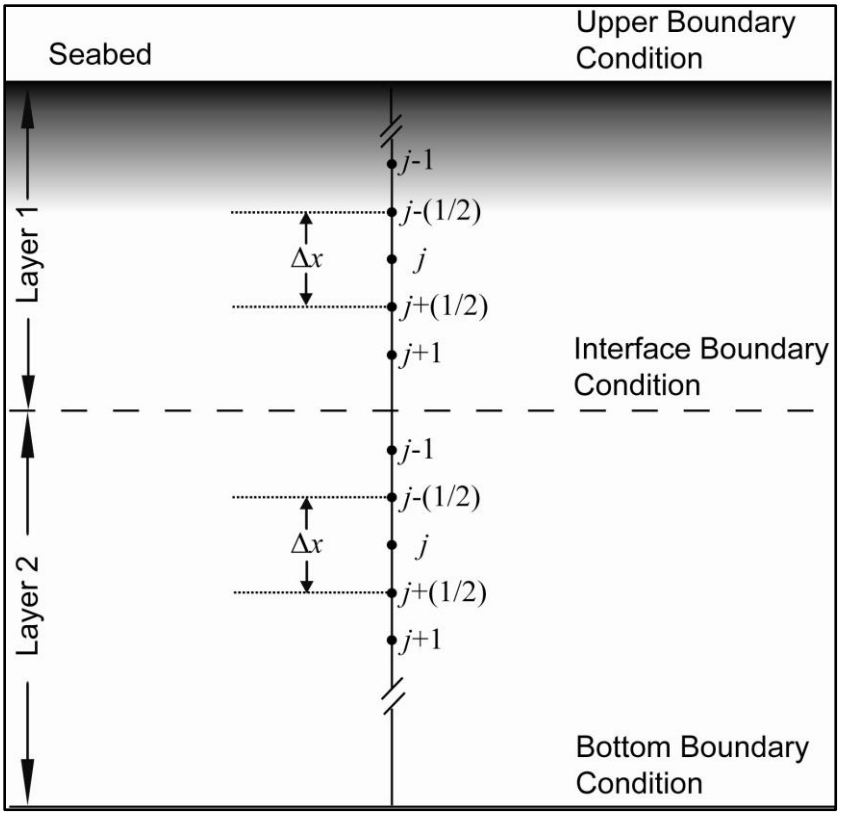

Figure 3.2 Numerical grid with depth intervals for a two-layer model on which equations (1) and (2) are valid.

Equation (1) contains a second-order partial derivative term given by

$$\frac{\partial}{\partial x}(D_{b1}\frac{\partial A}{\partial x}) \tag{3}$$

and a first-order partial derivative term given by

$$S\frac{\partial A}{\partial x} \tag{4}$$

Expanding the partial derivatives of both these terms give linear algebraic equations.

For the second-order partial derivative:

$$\frac{\partial}{\partial x}\left(D_{b1}\frac{\partial A}{\partial x}\right) = \left\{D_{b1}\ \frac{\partial A}{\partial x}\right\}_{\left(j+\frac{1}{2}\right)}\frac{1}{\Delta x} - \left\{D_{b1}\frac{\partial A}{\partial x}\right\}_{\left(j-\frac{1}{2}\right)}\frac{1}{\Delta x} \tag{5}$$

the right-hand side of the above equation can be further expanded

$$\left\{D_{b1\left(j+\frac{1}{2}\right)}\frac{A_{(j+1)} - A_j}{\Delta x}\right\}\frac{1}{\Delta x} - \left\{D_{b1\left(j-\frac{1}{2}\right)}\frac{A_j - A_{(j-1)}}{\Delta x}\right\}\frac{1}{\Delta x} \tag{6}$$

and rearranged to separate terms containing excess ^{210}Pb activity at $A_{(j-1)}$, A_j and $A_{(j+1)}$

$$\left\{D_{b1\left(j+\frac{1}{2}\right)}A_{(j+1)}\right\}\frac{1}{\Delta x^2} - \left\{D_{b1\left(j+\frac{1}{2}\right)}A_j + D_{b1\left(j-\frac{1}{2}\right)}A_j\right\}\frac{1}{\Delta x^2} + \left\{D_{b1\left(j-\frac{1}{2}\right)}A_{(j-1)}\right\}\frac{1}{\Delta x^2} \tag{7}$$

$$\left\{\frac{D_{b1\left(j+\frac{1}{2}\right)}}{\Delta x^2}\right\}A_{(j+1)} - \left\{\frac{D_{b1\left(j+\frac{1}{2}\right)} + D_{b1\left(j-\frac{1}{2}\right)}}{\Delta x^2}\right\}A_j + \left\{\frac{D_{b1\left(j-\frac{1}{2}\right)}}{\Delta x^2}\right\}A_{(j-1)} \tag{8}$$

Similarly, for the first order partial derivative:

$$S_j\left(\frac{\partial A}{\partial x}\right)_j = \left\{S_{(j)}\frac{A_j - A_{(j-1)}}{\Delta x}\right\} \tag{9}$$

the right-hand side of the above equation can be further expanded and rearranged:

$$\left(\frac{S_j}{\Delta x}\right)A_j - \left(\frac{S_j}{\Delta x}\right)A_{(j-1)} \tag{10}$$

The partial-derivatives have now been converted to linear algebraic equations. Combining all the terms for $A_{(j+1)}$, A_j, $A_{(j-1)}$ and including the term for the radioactive decay constant:

$$\left\{\frac{D_{b1\left(j+\frac{1}{2}\right)}}{\Delta x^2}\right\}A_{(j+1)} - \left\{\frac{D_{b1\left(j+\frac{1}{2}\right)} + D_{b1\left(j-\frac{1}{2}\right)}}{\Delta x^2}\right\}A_j + \left\{\frac{D_{b1\left(j-\frac{1}{2}\right)}}{\Delta x^2}\right\}A_{(j-1)}$$

$$- \left(\frac{S_j}{\Delta x}\right)A_j - \left(\frac{S_j}{\Delta x}\right)A_{(j-1)} - \lambda_j A_j = 0 \tag{11}$$

Also, for the steady-state model; $D_{b1(j+1/2)} = D_{b1(j-1/2)} = D_{b1j} = D_{b1}$, $S_j = S$ and $\lambda_j = \lambda$

By rearranging all the terms for $A_{(j-1)}$, A_j and $A_{(j+1)}$, we get:

$$\left(\frac{D_{b1}}{\Delta x^2}\right)A_{(j+1)} - \left(\frac{2D_{b1}}{\Delta x^2}\right)A_j + \left(\frac{D_{b1}}{\Delta x^2}\right)A_{(j-1)} - \left(\frac{S}{\Delta x}\right)A_j - \left(\frac{S}{\Delta x}\right)A_{(j-1)} - \lambda A_j = 0 \tag{12}$$

$$\left(\frac{D_{b1}}{\Delta x^2}\right)A_{(j+1)} - \left(\frac{S}{\Delta x} + \frac{2D_{b1}}{\Delta x^2} + \lambda\right)A_j + \left(\frac{D_{b1}}{\Delta x^2} + \frac{S}{\Delta x}\right)A_{(j-1)} = 0 \tag{13}$$

The interior-point form of the above equation is given as:

$$a_j A_j = b_j A_{(j+1)} + c_j A_{(j-1)} + d_j \tag{14}$$

where

$$a_j = \left(\frac{S}{\Delta x} + \frac{2D_{b1}}{\Delta x^2} + \lambda\right); b_j = \left(\frac{D_{b1}}{\Delta x^2}\right); c = \left(\frac{D_{b1}}{\Delta x^2} + \frac{S}{\Delta x}\right); d = 0$$

A set of equations generated between 1 and *n* for each point on an even grid can be solved using the tri-diagonal matrix algorithm (TDMA). TDMA has non-zero elements only in the main diagonal, one diagonal below, and one diagonal above the main diagonal.

$$\begin{bmatrix} b_1 & c_1 & & & & \\ a_2 & b_2 & c_2 & & & \\ & a_3 & b_3 & c_3 & & \\ & & \cdots & \cdots & .. & \\ & & & a_{n-1} & b_{n-1} & c_{n-1} \\ & & & & a_n & b_n \end{bmatrix} \begin{bmatrix} A_1 \\ A_2 \\ A_3 \\ \cdots \\ A_{n-1} \\ A_n \end{bmatrix} = \begin{bmatrix} d_1 \\ d_2 \\ d_3 \\ \cdots \\ d_{n-1} \\ d_n \end{bmatrix} \tag{15}$$

The explicit formulas for this method are:

$$A_i = pA_{(i+1)} + q_i \qquad i = 1,2,3,\ldots n \tag{16}$$

where:

$$p_i = \frac{b_i}{a_i - c_i p_{(i-1)}} \tag{17}$$

$$q_i = \frac{d_i - c_i q_{(i-1)}}{a_i - c_i p_{(i-1)}} \tag{18}$$

A goodness-of-fit coefficient, r^2, was determined by varying the parameters (given below) shown in **Table 2.1**. This r^2 is given by:

$$r^2 = 1 - \frac{\sum [A - A_{model}]^2}{\sum [A - A_{mean}]^2} \tag{19}$$

where A = measured excess ^{210}Pb activity; A_{model} = modeled excess ^{210}Pb activity, and A_{mean} = mean of measured excess ^{210}Pb activity for a given profile.

Adjustable parameters in the models are sediment accumulation rates (S), and biodiffusion coefficients, D_{b1}, and D_{b2} for the upper layer, layer 1, and lower layer, layer 2, respectively. Layer 1 is from 0 to L_1 (L_1 = 3-10 cm) where mixing is at a rapid rate and layer 2 is from L_1 to L_2 (L_2 = 6-30 cm) where mixing is slow, but at a non-zero rate. The boundary between layer 1 and layer 2 is estimated from inflection point on excess ^{210}Pb profiles.

As a first approximation, the model assumes S values from *Muhammad et al*., [2008] and mixing in layer 1 only while ignoring mixing in layer 2. With this approach, we can estimate a simple case for layer 1 where both sediment accumulation and mixing are taking place while only sediment accumulation is taking place in layer 2. Then, using D_{b1} from the first approximation, D_{b2} is estimated assuming S = 0. Finally, S values are estimated using D_{b1} and

D_{b2} values obtained from the first and second approximations. In all the three cases, the adjustable parameters were varied to arrive at model solutions that maximize the values of r^2.

3.4.2. ^{210}Pb Profiles

Depth distribution of measured excess ^{210}Pb is shown as circles while solid curves show modeled excess ^{210}Pb profiles (**Figure 3.3**) which are produced using the particle mixing numerical model representing sedimentation, biodiffusive mixing and radioactive decay of excess ^{210}Pb.

Model profiles are shown for two conditions; the first condition is of biodiffusion in layer 1 and sediment accumulation in layers 1 and 2 (dashed line), and the second condition is of biodiffusion and sediment accumulation in both layers (solid line). Horizontal dashed line in the figures shows the boundary between layer 1 and layer 2.

Results for model sediment accumulation rates (S), bioturbation coefficients, D_{b1} and D_{b2} for cores used in this study are given in **Table 2.1**. Best model profiles are produced when D_{b1} and D_{b2} are considered with S (r^2 average 0.9287) than without S (r^2 average 0.3149). The parameters are D_{b1} values are in the range of 0.007-60 $cm^2\ y^{-1}$ and D_{b2} values are in the range of 0.002-5 $cm^2\ y^{-1}$. Model derived S values range from 0.04-0.32 $cm\ y^{-1}$.

3.5 Discussion

On the GoP shelf, X-radiographs of the cores show sandy mud and muddy bioturbated fabric. Core MV-43 has a sandy mud fabric and bivalves, gastropods and shell fragments are common. Cores MV-42 and MV-44 have a mottled muddy texture with discrete burrows, bivalves and shell fragments distributed downcore. The bioturbated muds for these cores are predominantly silt and clay with a sand fraction that predominantly comprises foraminifera tests. This sand content decreases from 11 (core MV-43) to ~4% (core MV-44) with increasing water

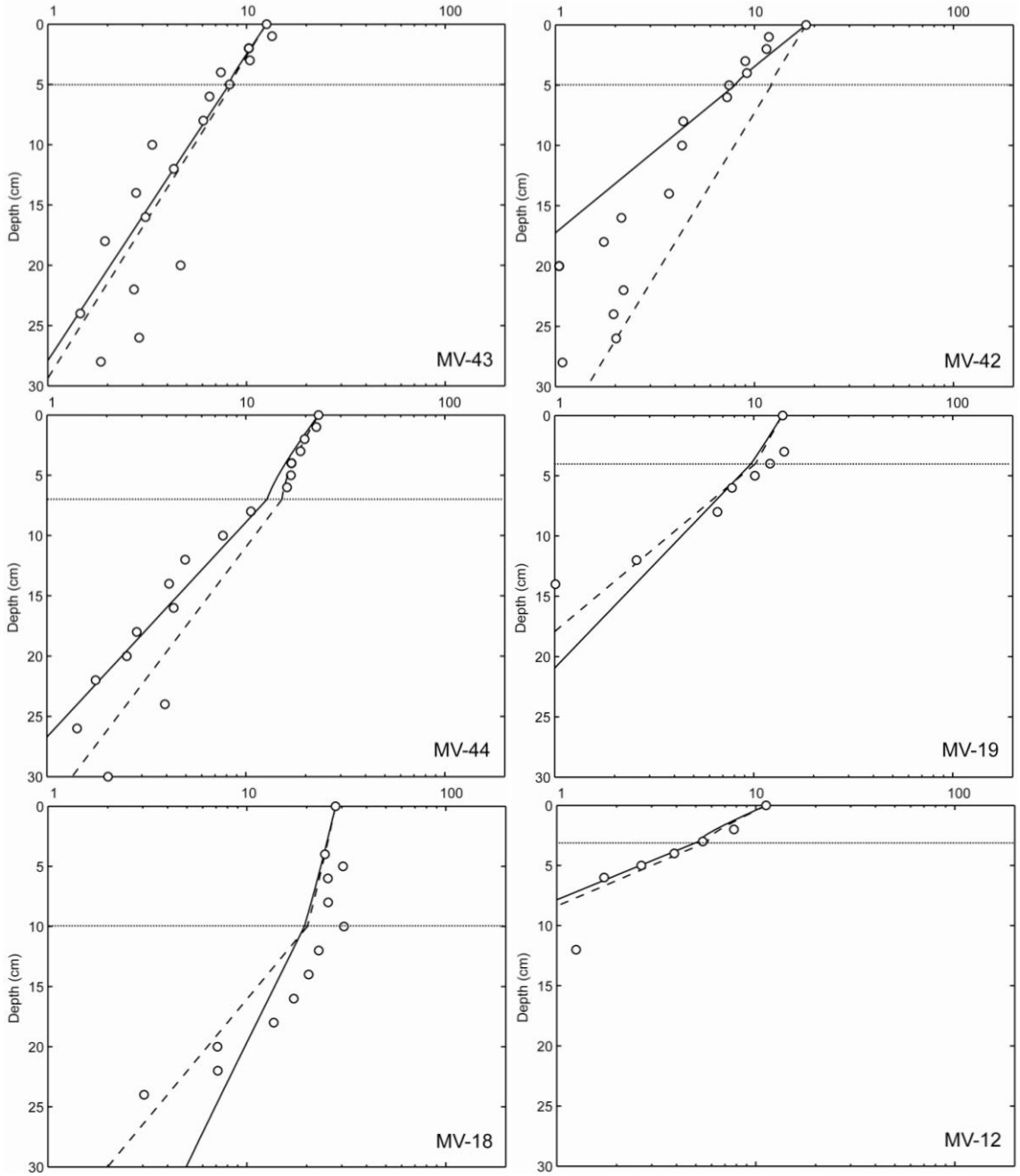

Figure 3.3 Profiles of excess ^{210}Pb in selected cores taken from the shelf and slope of GoP region. Core locations are shown in Figure 1and profiles are shown here in order of increasing water depth. Dashed line profiles are for D_{b1} in 0-L_1 and S in 0-L_1 and L_1-L_2 with D_{b2} = 0. Solid line profiles are for D_{b1} in 0-L_1, D_{b2} in L_1-L_2 and S in 0-L_1 and L_1-L_2. Horizontal dotted line in the figures shows the boundary between 0-L_1 and L_1-L_2.

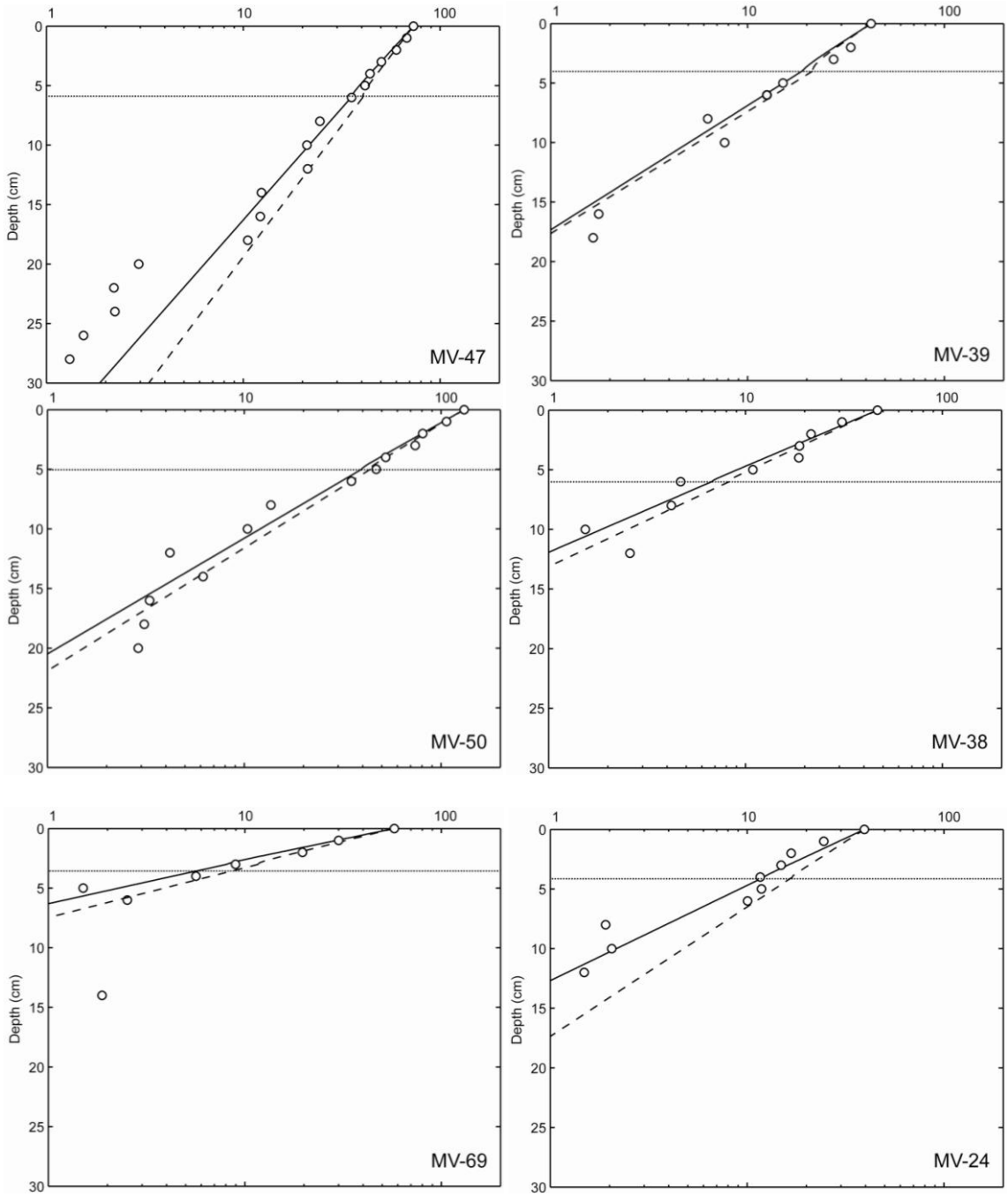

Figure 3.3 continued.

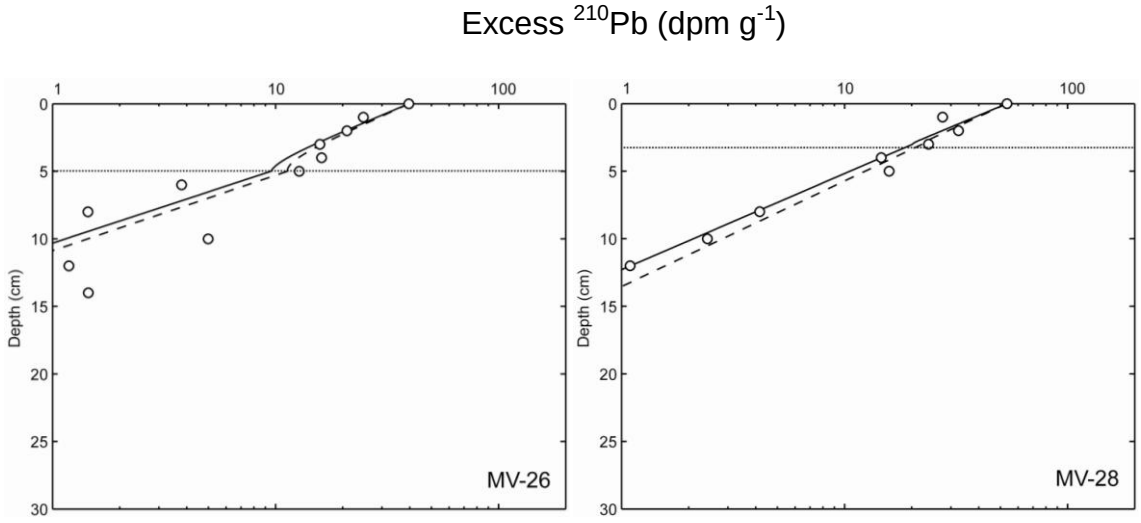

Figure 3.3 continued.

Table 3.1 Core water depths with adjustable parameters and goodness of fit, r^2 values. The adjustable parameters are D_{b1}, D_{b2}, and S, which were optimized based on assumptions of high sedimentation rates, zero sedimentation, and the intermediate case, shown below.

Core ID	Water depth (m)	D_{b1} (cm^2 y^{-1})	D_{b2} (cm^2 y^{-1})	S (cm y^{-1})	L_1 (cm)	L_2 (cm)	r^2
MV-12	372	0.07	0.02	0.08	3	9	0.9589
MV-18	267	60	5	0.1	10	14	0.6883
MV-19	229	2.9	0.5	0.16	4	10	0.8565
MV-24	2102	0.01	0.005	0.1	4	8	0.9428
MV-26	2232	0.1	0.02	0.06	5	9	0.9533
MV-28	2426	0.007	0.002	0.09	3	9	0.9212
MV-38	961	0.01	0.005	0.09	6	6	0.9661
MV-39	690	0.1	0.06	0.12	4	14	0.9602
MV-42	91	0.1	0.06	0.16	5	23	0.9083
MV-43	62	0.15	0.05	0.32	5	23	0.9076
MV-44	99	1.0	0.3	0.19	7	23	0.9706
MV-47	399	0.1	0.05	0.23	6	30	0.9918
MV-50	795	0.02	0.009	0.12	5	15	0.9883
MV-69	1638	0.008	0.005	0.04	3	11	0.9884

depth (**Figure 3.4**). Model S values vary from 0.16-0.3 cm y^{-1} Model D_{b1} values vary from 0.1-1.0 cm^2 y^{-1} and D_{b2} values vary from 0.05-0.3 cm^2 y^{-1} at these core locations.

For the upper 6 cm of a core taken from the northeastern GoP shelf (water depth ~50 m), *Walsh et al*., [2004] have reported D_b value of ~22 cm^2 y^{-1} using ^{234}Th (half-life ~24 d). This D_b value is an order of magnitude higher than the D_{b1} = 0.19 cm^2 y^{-1} for core MV-43 in the upper 8 cm because of the differences in half-lives of radioisotopes used in these studies [e.g. *Aller*, 1982]. The difference in measured D_b from two radioisotopes with different half-lives could be attributed to variations in infaunal abundance and activity [e.g. *Alperin et al*., 2002].

For cores MV-18 and MV-19 taken from the upper slope, X-radiographs display a bioturbated sandy mud fabric with few biogenic structures. Grain size analyses for these cores were done by sand-mud ratio. Sand fraction in MV-19 is ~80% while in core MV-18, sand fraction is more than 25% (**Figure 3.5**). Excess ^{210}Pb profiles for these cores display two clearly distinguishable segments, with a nearly uniform ^{210}Pb activity in the upper layer 0-L_1. For core MV-18, D_{b1} = 60 cm^2 y^{-1} is the highest value reported in all the cores taken for this study. For core MV-19, D_{b1} = 2.9 cm^2 y^{-1} which is also more than an order of magnitude higher than D_{b1} values for cores MV-47, MV-39, MV-38, MV-50, MV-69, MV-24, MV-26 and MV-28, taken from the slope and deeper GoP basin (**Figure 3.1**). For core MV-18, D_{b2} = 5 cm^2 y^{-1} and for core MV-19, D_{b2} = 0.5 cm^2 y^{-1}. The two segments of excess ^{210}Pb activity likely represent a change in the intensity of biodiffusion with depth because these cores have lower measured S value and higher seabed inventories as compared to cores MV-42, MV-43 and MV-44 close to the shelf edge. Also, the X-radiographs show no evidence of a major depositional event. The two sources of excess ^{210}Pb in the GoP basin are atmospheric input and ^{226}Ra decay from the water column [*Muhammad et al*., 2008]. Based on bathymetric and channel network data, this location could be a possible conduit for sediments transported from the shelf to deeper basins [*Muhammad et al*.,

(a)

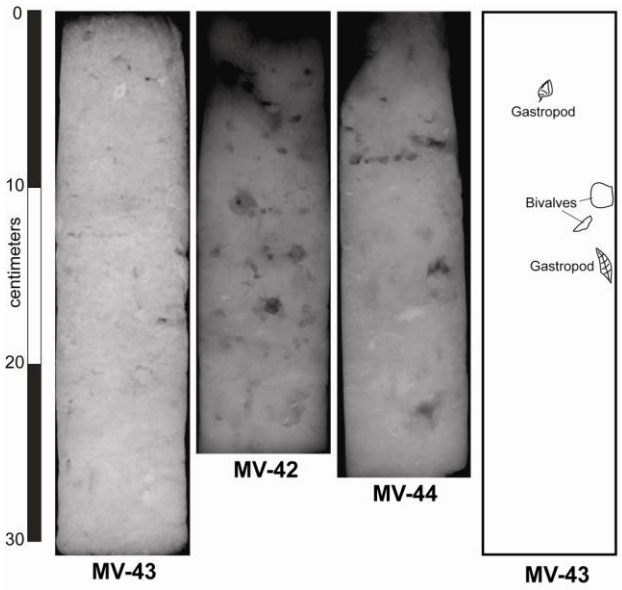

(b)

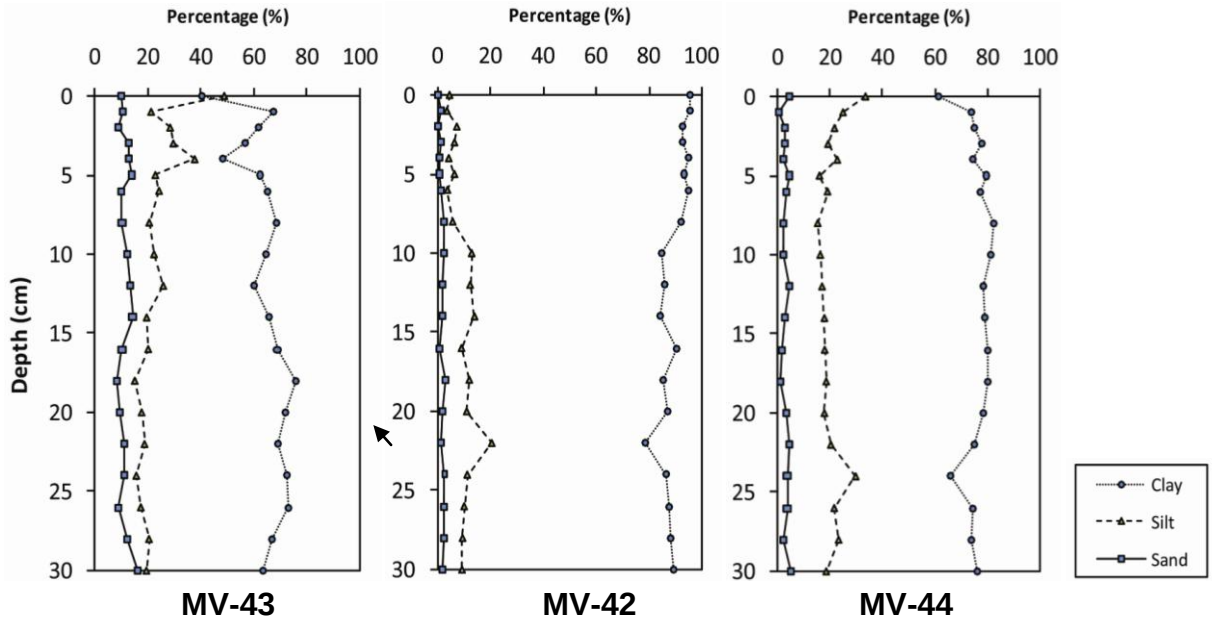

Figure 3.4 (a) X-radiographs and (b) grain size distribution of cores MV-43, MV-42 and MV-44, taken from the shelf edge. X-radiograph negatives with sand and shell structures exhibit light texture (core MV-43) while mud shows a dark texture (cores MV-42 and MV-44). Drawing to the right of core MV-43 in (a) illustrates distribution of biogenic elements.

(a)

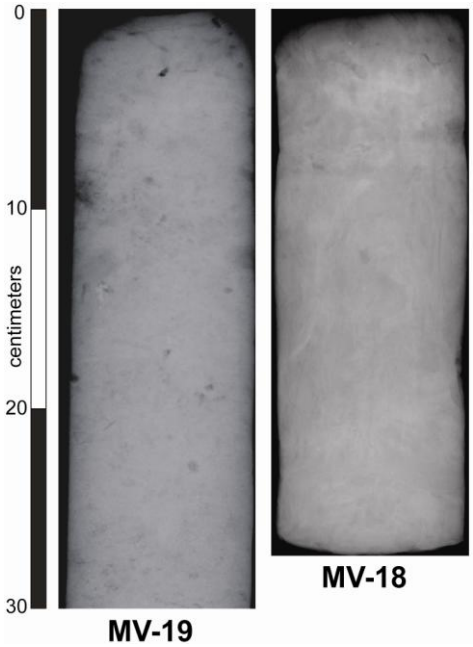

(b)

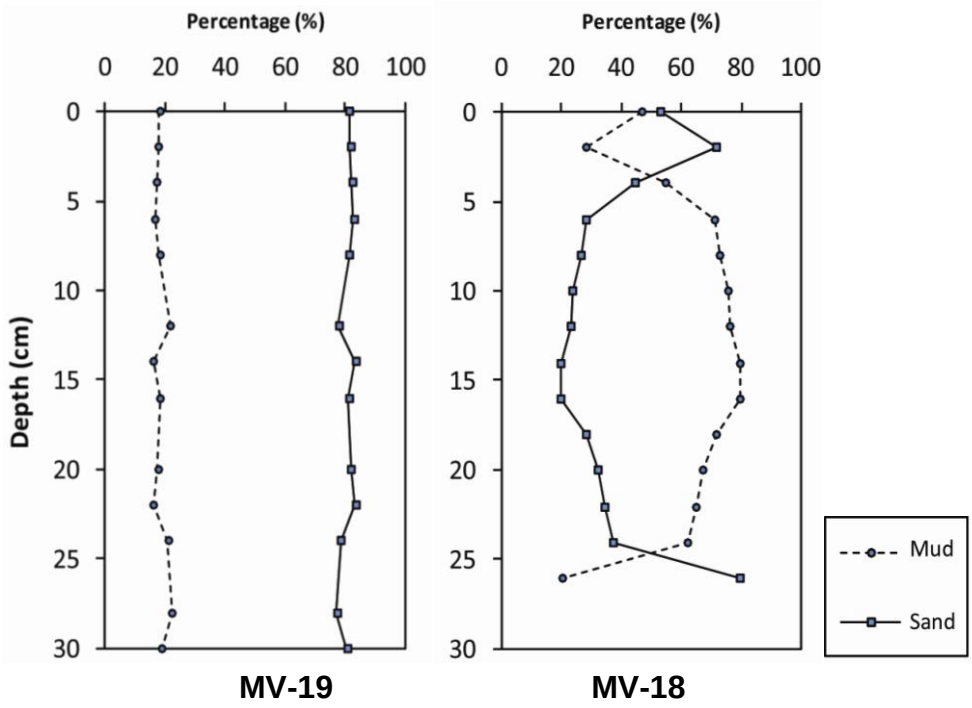

Figure 3.5 (a) X-radiographs and (b) grain size distribution for cores MV-19 and MV-18 on the upper slope.

2008]. However, higher seabed ^{210}Pb inventories can, in part, be due to higher biodiffusion coefficients [e.g. *Aller et al*., 1980; *Santschi et al*., 1980].

Cores taken from the upper and middle slope in the Pandora Trough are MV-47, MV-38, MV-39, MV-50 and MV-69 (**Figure 3.1**). There is little change across the slope in the sedimentary structure of cores. The sedimentary fabrics of cores MV-47, MV-38, MV-39 and MV-50 are mottled to homogenous muds with discrete burrows. These bioturbated muds have a clay content that exceeds 60% and a sand fraction of ~2%. Samples analyzed in the 0-2 cm from these cores show that carbonate content in these sediments exceeds 30% [*Febo*, 2007] (**Figure 3.6**). These five cores show an exponential decrease in excess ^{210}Pb activities downcore. D_{b1} values at these five core locations are in the range of 0.008-0.1 cm^2 y^{-1} and D_{b2} values are in the range of 0.005-0.06 cm^2 y^{-1} and L_2 varies from 9-31 cm. Except for core MV-47, excess ^{210}Pb penetrates to a depth of less than 20 cm or less in these cores (**Figure 3.3**). These core locations have also reported highest surface excess ^{210}Pb activities suggesting efficient particle scavenging from the water column [*Muhammad et al*., 2008]. The slope of the profiles of these cores decreases with increasing water depth, consistent with a decrease in model *S* values with increasing water depth (**Table 3.1**). In core MV-47, the rapid decrease in excess ^{210}Pb activity between the 16-18 cm interval could be a result of depositional event or more tiering of bioturbation [e.g. *Bentley et al*., 2002; also see *Bromley*, 1996]. A piston core (MV-46) at the site of MV-47 gives an AMS ^{14}C dated sediment accumulation rate of 0.03 cm y^{-1} in the upper 2 m of the sediments (see chapter 4) which is an order of magnitude lower than the model *S* value of 0.23 cm y^{-1} (**Table 3.1**). AMS ^{14}C dated sediment accumulation rates taken from a piston core MV-54 (8°56' 145°23', 923 m) from an open slope non-channelized location has a sediment accumulation rate of 0.01 cm y^{-1} in the upper 2 m [*Febo et al*., 2008]. This sediment accumulation rate is an order of magnitude lower than the model *S* value of 0.09 cm y^{-1} for MV-

(a)

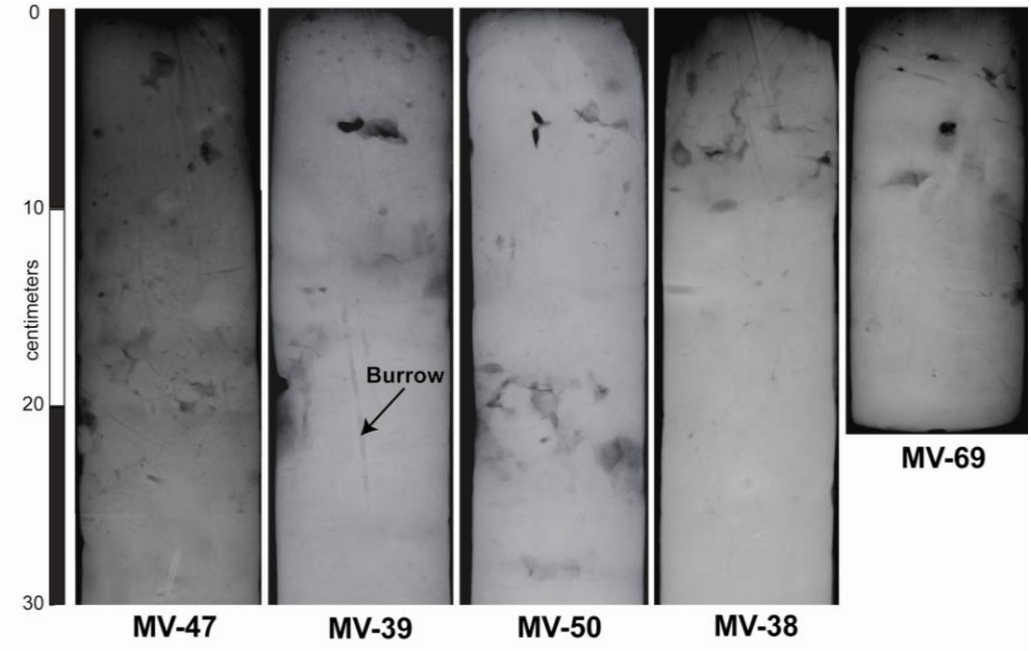

(b)

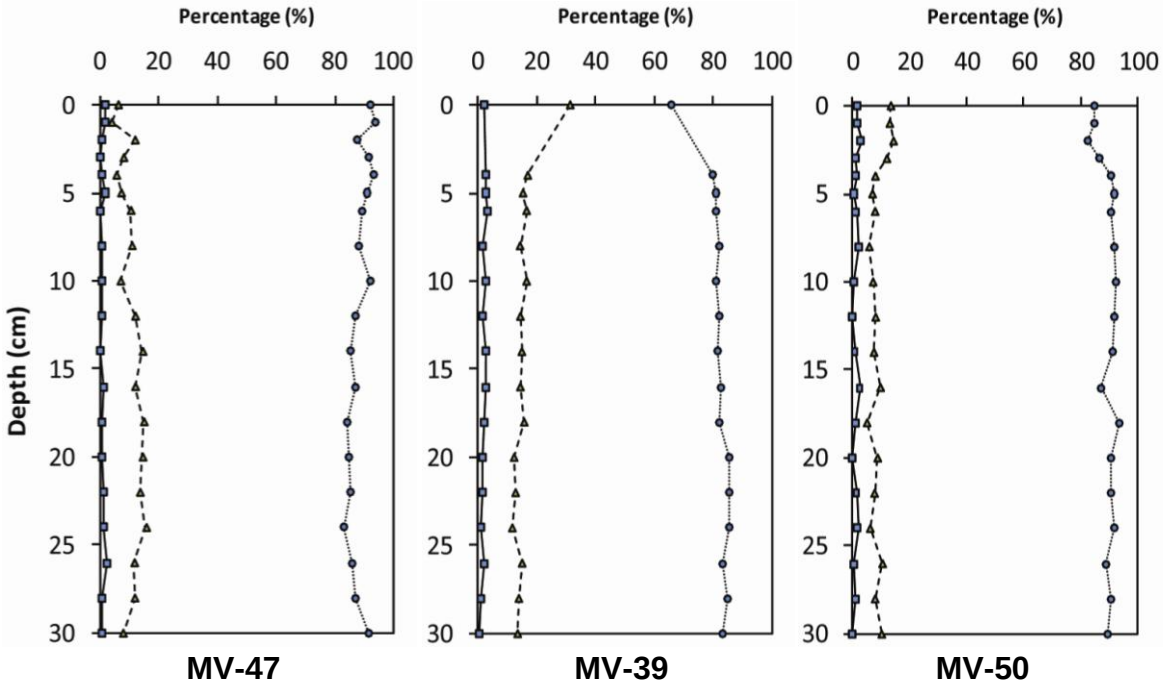

Figure 3.6 Representative cores from the upper and middle slope region in the Pandora Trough showing (a) X-radiographs and (b) grain size distribution for cores MV-47, MV-39, MV-50, MV-38 and MV-69.

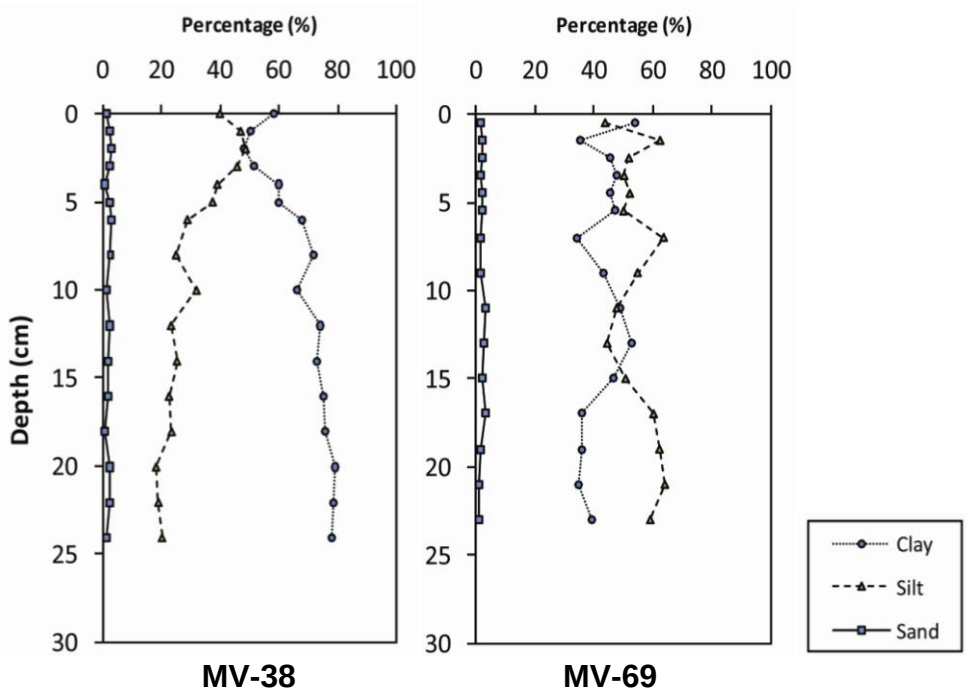

Figure 3.6 continued.

38 which was taken from a nearby channelized location (see **Figure 3.1** for core locations). Another piston core, MV-66 (10°00' 145°9', 1793 m), taken from the flat-floored basin in the southern Pandora Trough has an AMS ^{14}C sediment accumulation rate of 0.04 cm y^{-1} in the upper 8 m of the seabed [*Patterson*, 2006].

Only one core from the Ashmore Trough (MV-12) has been used in the present study (**Figure 3.7**). For this core, excess ^{210}Pb is present in the sediment to a depth of 12 cm with activities below the detection limit of 1 dpm g^{-1} between 6 and 12 cm. Core MV-12 has a homogenous muddy fabric with some mottling in the upper 10 cm and discrete traces of biological activity are rare. Sand content is less than 4% and the carbonate component analyzed in the upper 0-2 cm exceeds 70% [*Febo et al*., 2008]. Model D_{b1} = 0.07 cm^2 y^{-1} and D_{b2} = 0.02 cm^2 y^{-1}. Model S = 0.08 cm y^{-1} which is comparable to sediment accumulation rates of 0.05-0.23 cm y^{-1} for other cores in the Ashmore Trough [*Muhammad et al*., 2008].

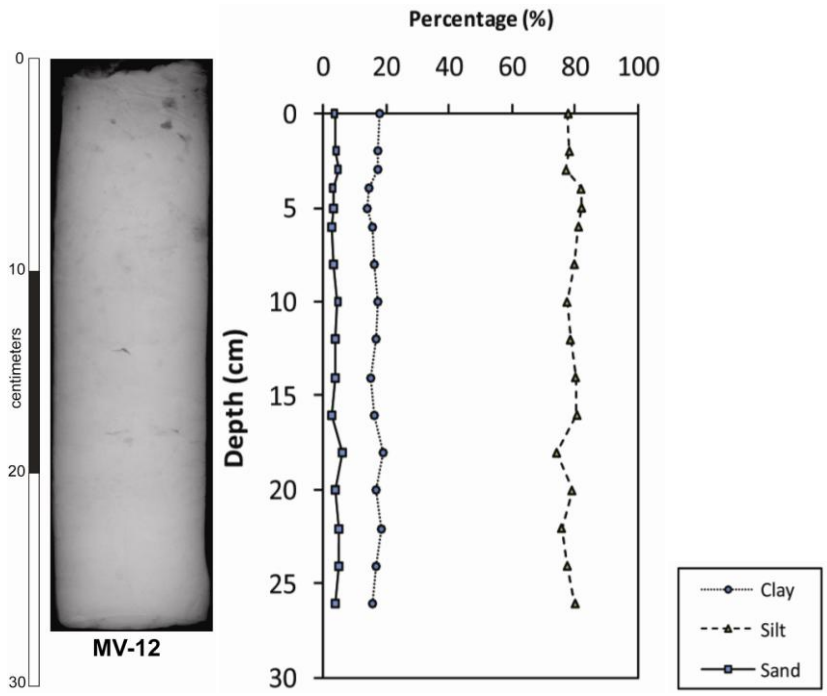

Figure 3.7 X-radiograph and grain size distribution for core MV-12 taken from the Ashmore Trough.

X-radiographs for cores MV-24, MV-26 and MV-28 taken from the Moresby Trough reveal a bioturbated sedimentary fabric (**Figure 3.8**). The upper 20 cm of core MV-24 are mottled while vertical burrows are visible in the bottom section of the core. Core MV-24 is located in a prominent channel shows sandy laminated texture at 24-30 cm, which is interpreted as a possible turbidite that has been partially bioturbated [*Muhammad et al.*, 2008]. Cores MV-26 and MV-28 have a relatively homogenous muddy texture. The biogenic structure below the 30 cm in core MV-28 is interpreted as a spiral burrow. These sediments consist primarily of clay and silt with a sand fraction of 4% or less. D_{b1} values are in the range of 0.007-0.1 $cm^2\ y^{-1}$ and D_{b2} values are in the range of 0.002-0.02 $cm^2\ y^{-1}$. Excess ^{210}Pb is present in the upper 15 cm in these cores (**Figure 3.3**). The exponential excess ^{210}Pb decay profiles are typical as would be expected in deep water environments where sediments are undergoing steady-state deposition.

(a)

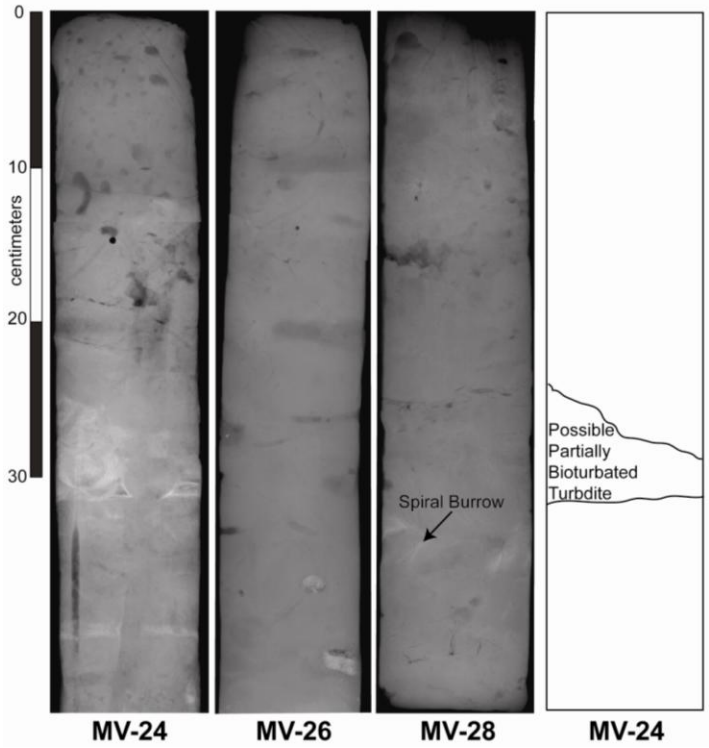

(b)

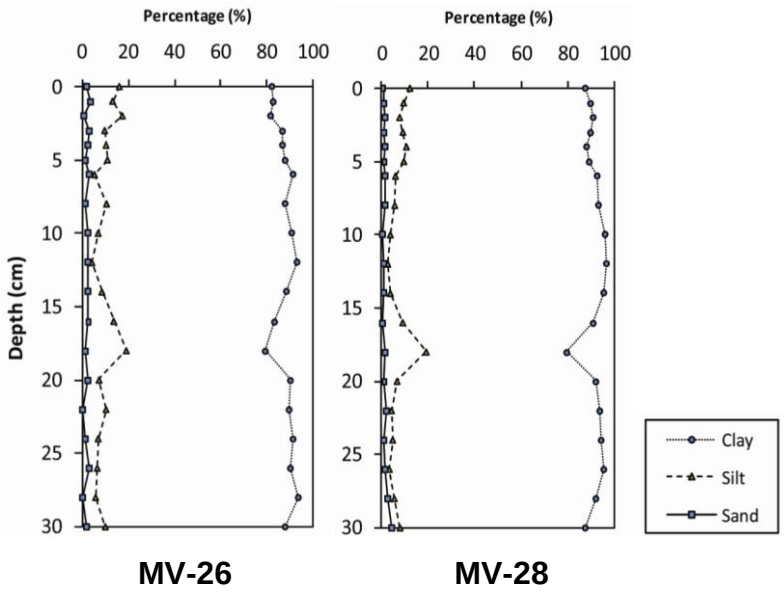

Figure 3.8 (a) X-radiographs for cores MV-24, MV-26 and MV-28 and (b) grain size distribution for cores MV-26 and MV-28 from the Moresby Trough. Dark regions in X-radiographs are mud while light regions represent sandy texture. Drawing on the right illustrates possible partially bioturbated turbidite in core MV-24.

The ratio of core-calculated ^{210}Pb and theoretical ^{210}Pb flux for these deep water cores also indicate steady-state conditions at these water depths [*Muhammad et al*., 2008]. Model *S* values for these cores are in the range of 0.06-0.1 cm y^{-1}.

Plotting the water depth versus D_{b1} values for all the cores taken in the study area shows a linear relationship ($R^2 = 0.4334$) where D_{b1} values decrease with increasing water depth (**Figure 3.9**). Core MV-18 has been excluded from regression because of high D_{b1} of 60 cm^2 y^{-1}. The relationship of decreasing D_{b1} values with increasing water depth seems consistent with the observations in other continental margin settings [e.g. *Boudreau*, 1994] where biomass and numbers of benthic fauna decrease with increasing water depth [*Rex et al*., 2006]. Bioturbation rates are generally higher on the shelf and upper slope regions than in deep waters probably because of greater amounts of fresh detritus are available to the benthos as a source of food [e.g. *Carney*, 1989].

Although D_{b1} and *S* were not estimated independently, there appears to be a general trend of decreasing D_{b1} with decreasing *S* (**Figure 3.10**). The best fit gives $R^2 = 0.2603$, plotted as a solid line with core MV-18 excluded from regression. The scatter in the present data is probably due to bioturbation at different water depths. Total organic carbon (TOC) distribution in surface sediments shows a high (landward) to low (seaward) trend in GoP [*Febo*, 2008].
In all profiles, a better correlation between measured and modeled data is achieved with lower *S* values than reported by *Muhammad et al*., [2008]. Taking an average of model *S* values and *SAR* values of *Muhammad et al*., [2008], results of this study suggest that *SAR* estimates in *Muhammad et al*., [2008] are overestimated by a factor of ~1.4. Sedimentation rates can be overestimated in a region of slow sediment accumulation as a result of biological mixing [e.g. *Benninger et al*., 1979].

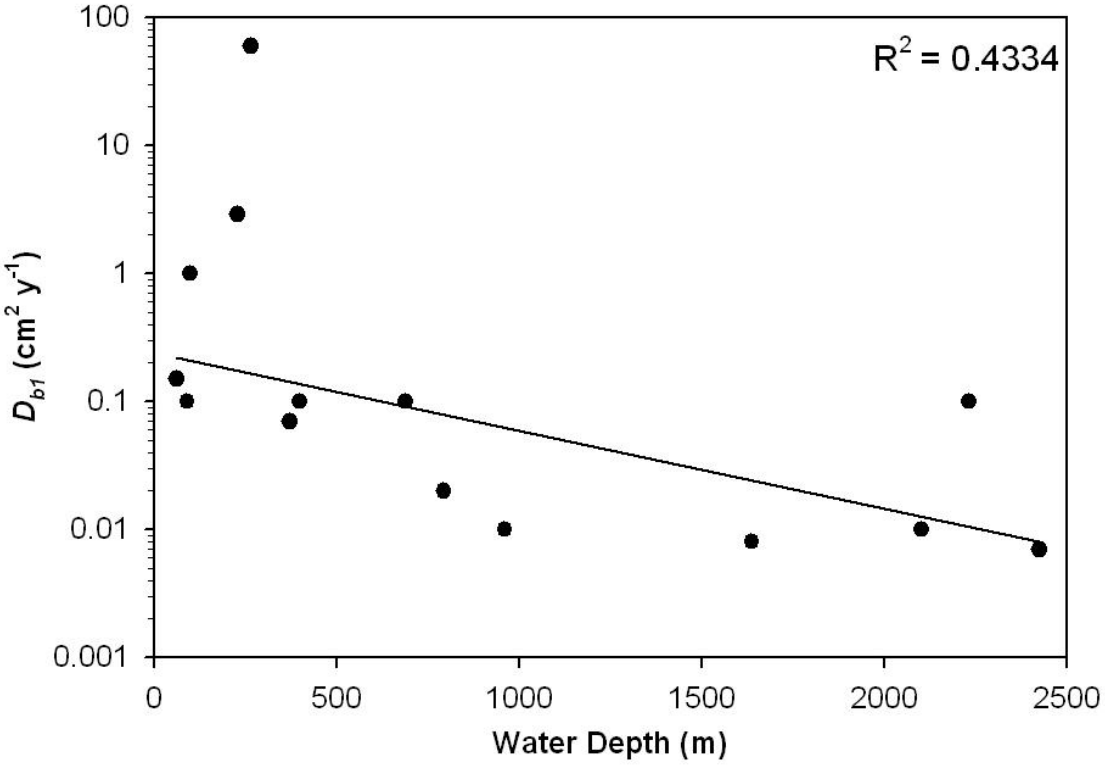

Figure 3.9 Plot of water depth versus D_{b1} values on semi-log scale for cores in the study area. The solid line is the best fit for all the cores except MV-18.

This suggests that the sediment mass accumulation rates reported by *Muhammad et al*., [2008] is probably overestimated and the processes shaping ^{210}Pb distributions in sediments include a combination of biodiffusion and slow sediment accumulation. Radiocarbon dates obtained from piston cores in the study are lower than model *S* values by a factor of 10. The difference between these sedimentation rates is because of ~250 time differences in decay timescales between the two isotopes [e.g. *Sadler*, 1981; *Alexander et al*., 1991]. Particle fluxes in GoP over 100 yr timescales are relatively well constrained from this study, given the small number of cores over a large area.

Additional information might be gained from additional tracers such as ^{234}Th or time-dependent tracers such as ^{137}Cs (or ^{239,240}Pu), which could be used to confirm the model *S* estimates from this study.

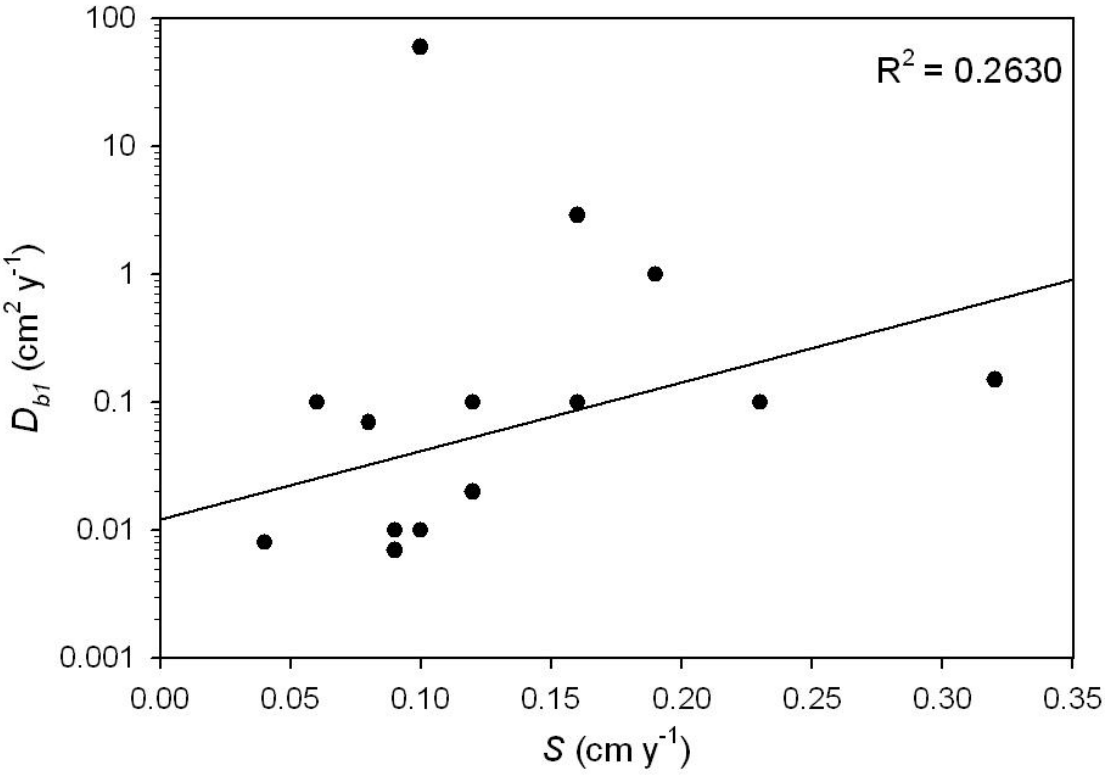

Figure 3.10 Plot of S versus D_{b1} values on semi-log scale for all cores in the study area. The solid line is the best fit for all cores except MV-18.

3.6 Conclusions

Bioturbation and sediment accumulation rates estimated from model results show that D_b and S in GoP shelf and slope vary by an order of magnitude. Model D_{b1} values are in the range of 0.007-60 cm^2 y^{-1} and D_{b2} values are in the range of 0.002-2.9 cm^2 y^{-1}. Model S values range from 0.04-0.32 cm y^{-1}. For the cores locates on the upper slope and middle slope in the Pandora Trough, biodiffusion coefficients and mixing depths exhibit a decreasing trend with increasing water depth consistent with similar observations in other studies. Sediment mass accumulation rates for the Gulf of Papua region may have been overestimated in *Muhammad et al*., [2008] by a factor of ~1.4.

3.7 References

Aller, R. C., L. K. Benninger, and J. K. Cochran (1980), Tracking particle associated processes in nearshore environments by use of $^{234}Th/^{238}U$ disequilibrium, *Earth Planet. Sci. Lett.*, *47*, 161-175.

Aller, R. C. (1982), The effects of macrobenthos on chemical properties of marine sediment and overlying water in *Animal-Sediment Relations*, edited by P. L. McCall and M. J. S. Tevesz, pp. 53-102, Plenum, New York, NY.

Alongi, D. M., P. Christoffersen, F. Tirendi, A.I. Robertson (1992), The influence of freshwater and material export on sedimentary facies and benthic processes within the Fly Delta and adjacent Gulf of Papua (Papua New Guinea), *Cont. Shelf Res*., *12*, 287-326.

Alongi, D. M., and A. I. Robertson (1995), Factors regulating benthic food chains in tropical river deltas and adjacent shelf areas, *Geo-Mar. Lett*. *15*, 145-152.

Alperin, M. J., I. B., Suayah, L. K. Benninger, and C. S., Martens (2002), Modern organic carbon burial fluxes, recent sedimentation rates, and particle mixing rates from the upper continental slope near Cape Hatteras, North Carolina (USA), *Deep-Sea Res. II, 49*, 4645–4665.

Andersen, T. J., O. A. Mikkelsen, A. L. Møller, and M. Pejrup (2000), Deposition and mixing depths on some European intertidal mudflats based on ^{210}Pb and ^{137}Cs activities, *Cont. Shelf Res.*, *20*, 1569-1591.

Benninger, L. K., R. C. Aller, J. K. Cochran, and K. K. Turekian (1979), Effects of biological sediment mixing on the ^{210}Pb chronology and trace metal distribution in a Long Island sound sediment core, *Earth Planet. Sci. Lett.*, *43*, 241–259.

Bentley. S, J., T. R. Keen, C. A. Blain, and W. C. Vaughan (2002), The origin and preservation of a major hurricane event bed in the Northern Gulf of Mexico: Hurricane Camille, 1969, *Mar. Geol*., *186*, 423–446.

Bentley, S. J., A. Sheremet, J. M. Jaeger (2006), Event sedimentation, bioturbation, and preserved sedimentary fabric: Field and model comparisons in three contrasting marine settings, *Cont. Shelf Res.*, *26*, 2108-2124.

Berner, A. R. (1980), *in Early Diagenesis: A Theoretical Approach*, Princeton University Press, pp. 241.

Boudreau, B. P. (1986), Mathematics of tracer mixing in sediments: I. Spatially-dependent, diffusive mixing, *Am. J. Sci*., *286*, 199-238.

Boudreau, B. P., and D. M. Imboden (1987), Mathematics of tracer mixing in sediments: III. The theory of nonlocal mixing within sediments, *Am. J. Sci*., *287*, 693-719.

Boudreau, B. P. (1994), Is burial velocity a master parameter for bioturbation?, *Geochim. Cosmochim. Acta*, *58*, 1243–1249.

Boudreau, B. P. (1997), in *Diagenetic Models and Their Implementation*, Springer-Verlag, pp. 414.

Bromley, R. G. (1996), in *Trace Fossils: biology, taphonomy and applications* (2nd edition), Chapman & Hall, London, pp. 361.

Brunskill, G. J., K. J. Woolfe, and I. Zagorskis (1995), Distribution of riverine sediment chemistry on the shelf, slope and rise of the Gulf of Papua, *Geo. Mar. Lett.*, *15*, 160–165.

Burdige, D. J. (2006), in *Geochemistry of Marine Sediments*, Princeton University Press, New Jersey, pp. 609.

Carney, R. S. (1982), Bioturbation and biodeposition, in *Principles of marine benthic paleoecology*, edited by A. J. Boucaut, pp. 357-400, Academic press, New York.

Carney, R. S. (1989), Examining relationships between organic carbon flux and deep-sea deposit feeding, in *Ecology of Marine Deposit Feeders*, edited by G. Lopez et al., pp. 24-58, Springer-Verlag, New York.

Carpenter, R., M. L. Peterson, and J. T. Bennett (1982), ^{210}Pb-derived sediment accumulation and mixing rates for the Washington continental slope, *Mar. Geol.*, *48*, 135-164.

Coakley, J. P and J. P. M. Syvitski (1991) Sedigraph technique. In: Syvitski J. P. M. (Ed.), Principles, Methods, and Application of Particle Size Analysis. Cambridge: Cambridge University Press, 368 pp.

Cochran, J. K. (1982), The oceanic chemistry of the U-and Th-series nuclides, in *Uranium Series Disequilibrium: Applications to Environmental Problems*, edited by M. Ivanovich and R. S. Harmon, pp. 384–430, Clarendon, Oxford, U.K.

Cochran, J. K. (1985), Particle mixing rates in sediments of the eastern equatorial Pacific: evidence from ^{210}Pb, ^{239,240}Pu, and ^{137}Cs distributions at MANOP sites, *Geochim. Cosmochim. Acta*, *49*, 1195–1210.

Cutshall, N. H., I. L. Larsen, and C. R. Olsen (1983), Direct analysis of Pb-210 in sediment samples: Self-absorption corrections, *Nucl. Instrum. Methods Phys. Res.*, *206*, 309–312.

DeMaster, D. J., B. A. McKee, C. A. Nittrouer, D. C. Brewster, and P. E. Biscaye (1985), Rates of sediment reworking at the HEBBLE site based on measurements of Th-234, Cs-137 and Pb-210, *Mar. Geol.*, *66*, 133-148.

Goldberg, E. D., and M. Koide (1962), Geochronological studies of deep sea sediments by the ionium/thorium method, *Geochim. Cosmochim. Acta*, *26*, 417–450.

Febo, L. A. (2007), Paleoceanography of the Gulf of Papua using multiple geophysical and micropalentological proxies, PhD thesis, 163 pp., Louisiana State U.

Henderson, G. M., and R. F. Anderson (2003), TheU-series Toolbox for Paleoceanography in *Uranium-Series Geochemistry*, edited by B. Bourdon et al., pp. 493–532, Mineralogical Society of America, *Reviews in Mineralogy*, *52*, Washington D.C.

Keen, T. R., D. S. Ko, R. L. Slingerland, S. Riedlinger, and P. Flynn (2006), Potential transport pathways of terrigenous material in the Gulf of Papua, Geophys. Res. Lett., 33, L04608, doi:10.1029/2005GL025416.

Legeleux, L., J. Reyss and S. Schmidt (1994), Particle mixing rates in sediments of the northeast tropical Atlantic: Evidence from $^{210}Pb_{xs}$, ^{137}Cs, $^{228}Th_{xs}$ and $^{234}Th_{xs}$ downcore distributions, *Earth Planet. Sci. Lett., 128,* 545-562.

Moore, D. G., and P. C. Scruton (1957), Minor internal structures of some recent unconsolidated sediments, *Am. Assoc. Petrol. Geol. Bull., 41,* 2723-2751.

Muhammad, Z., S. J. Bentley, L. A. Febo, A. W. Droxler, G. R. Dickens, L. C. Peterson, and B. N. Opdyke (2008), Excess ^{210}Pb inventories and fluxes along the continental slope and basins of the Gulf of Papua, *J. Geophys. Res.*, *113*, doi:10.1029/2006JF000676.

Nittrouer, C. A., R. W. Sternberg, R. Carpenter, and J. T. Bennett (1979), Use of Pb-210 geochronology as a sedimentological tool: Application to the Washington continental-shelf, *Mar. Geol.*, *31*, 297–316.

Nittrouer, C. A., and R.W. Sternberg (1981), The formation of sedimentary strata in an allochthonous shelf environment: the Washington continental shelf, *Mar. Geol. 42*, 201-232.

Nozaki, Y., J. K. Cochran, K. K. Turekian, and G. Keller (1977), Radiocarbon and ^{210}Pb distribution in submersible-taken deep sea cores from Project FAMOUS, *Earth Planet. Sci. Lett., 34*, 167-173.

Patterson, L. J. (2006), Petrological and geochemical investigations of deep sea turbidite sands in the Pandora and Moresby Troughs: Source to sink Papua New Guinea focus area, M. S. thesis, Louisiana State University.

Rex, M. A., R. J. Etter, J. S. Morris, J. Crous, C. R. McClain, N. A. Johnson, C. T. Stuart, J. W. Deming, R. Thies, and R. Avery (2006), Global bathymetric patterbs of standing stock and body size in the deep-sea benthos, *Mar. Ecol. Prog. Ser. 317*, 1-8.

Rhoads, D. C., and D. K. Young (1970), The influence of deposit-feeding organisms on sediment ability and community trophic structure, *J. Mar. Res.*, *28*, 151-178.

Rice, D. L. (1986), Early diagenesis in bioadvective sediments: relationships between the diagenesis of ^{7}Be, sediment reworking, and the abundance of conveyor-belt deposit feeders, *J. Mar. Res.*, *44*, 149-184.

Sadler, P. M. (1981), Sediment accumulation rates and the completeness of stratigraphic sections, *J. Geol*., *89*, 569–584.

Santchi, P. H., Y. H. Li, J. J. Bell, R. M. Trier and K. Kawtaluk (1980), Pu in coastal marine environments, *Earth Planet. Sci. Lett., 51*, 248-265.

Slingerland, R. L., N. W. Driscoll, J. D. Milliman, S. R. Miller, and E. A. Johnstone (2008), Anatomy and growth of a Holocene clinothem in the Gulf of Papua, *J. Geophys. Res.*, doi:10.1029/2006JF000628.

Smith, C. R., R. Pope, D. J. DeMaster and L. Magaard (1993), Age-dependent mixing in deep-sea sediments, *Geochim. Cosmoch. Acta 57*, 1473-1488.

Smith, J. N., B. P. Boudreau, and V. Noshkin (1986), Plutonium and ^{210}Pb distributions in northeast Atlantic sediments: subsurface anomalies caused by non-local mixing, *Earth Planet. Sci. Lett., 81*, 15-28.

Suckow, A. U. Treppke, M. H. Wiedicke, and M. E. Weber (2001), Bioturbation coefficients of deep-sea sediments from the Peru Basin determined by gamma spectrometry of $^{210}Pb_{exc}$, *Deep Sea Res. Part II, 48,* 3569-3592.

Walsh, J. P., and C. A. Nittrouer (2003), Contrasting styles of off-shelf sediment accumulation in New Guinea, *Mar. Geol., 196*, 105–125.

Walsh, J. P., C. A. Nittrouer, C. M. Palinkas, A. S. Ogston, R. W. Sternberg, and G. J. Brunskill (2004), Clinoform mechanics in the Gulf of Papua, New Guinea, *Cont. Shelf Res., 24*, 2487–2510.

Wheatcroft, R. A. (1990), Preservation potential of sedimentary event layers, *Geology*, *18*, 843-845.

Wheatcroft, R. A., P. A. Jumars, C. R. Smith & A. R. M. Nowell (1990), A mechanistic view of the particulate biodiffusion coefficient: Step lengths, rest periods and transport directions. *J. Mar. Res*., *48*, 177-207.

Wolanski, E., A. Norro, and B. King (1995), Water circulation in the Gulf of Papua, *Cont. Shelf Res., 15*, 185–212.

CHAPTER 4
LATE QUATERNARY MARINE SEDIMENT RECORD FROM THE GULF OF PAPUA CONTINENTAL MARGIN

4.1 Introduction

Sediments eroded from the land are transported through fluvial sources and may be deposited eventually at the seabed to become part of the marine sedimentary record. The controls on this sediment supply and deposition range from climate and sea level variations to dynamic processes such as storms and local wave and tide regimes. There is a need to better understand the sedimentary dynamics because of increasing human impact and residence in coastal areas. The preserved sedimentary record in the continental margins can be deciphered to study past sedimentary dynamics and infer future impact on coastal areas from natural hazards and urban development. This study requires selecting a site where there is active transfer of sediments from their source of origin to the seabed where these sediments get deposited. As part of the NSF-MARGINS Source-to-Sink program, the Gulf of Papua (GoP) on the northeastern Australian continental margin provides a unique opportunity to study this transfer of sediments from source-to-sink within a generally closed system.

The GoP experiences a wet-tropical environment with major rivers such as the Fly, Kikori and Purari, along with smaller tributaries currently delivering 200-300 megatonnes (Mt) of terrigenous siliciclastic material each year to adjacent shelf and slope [*Harris et al*., 1993; *Milliman*, 1995]. Most of this terrigenous material presently accumulates in an extensive subaqueous delta on the inner shelf [*Wolanski and Alongi*, 1995; *Walsh et al*., 2004] formed since the Holocene [*Slingerland et al*., 2008a]. Sediment accumulation rates based on ^{210}Pb geochronology exceed ~0.2 cm y^{-1} in cores from the northeasterrn GoP shelf, although less than 5% of the terrigenous fraction escapes beyond the shelf [*Walsh and Nittrouer*, 2003; *Muhammad et al*., 2008]. However, core stratigraphy in deeper seabed region of GoP shows alternating

turbidite and hemipelagic intervals deposited since the Last Glacial Maximum (LGM) [*Jorry et al*., 2008]. The question is if these alternating turbidite and hemipelagic intervals represent periods of variable terrigenous flux to the deeper seabed in the GoP since post-LGM sea level rise. Sediment sinks on the GoP shelf and slope may have varied since the Late Quaternary as a result of changes in the flow regime of multiple fluvial sources delivering sediments in the study area [see Fig 11, *Febo et al*., 2008]. Predicting the behavior of a given sediment dispersal-system has critical implications for a better understanding of the geological processes in a given study area.

To address this issue of variable source-to-sink, the general goal of this research is to examine temporal and spatial variability in sediment accumulation in the GoP since the post-LGM sea level rise. Specific goal of this study is to constrain the origin of the sediment blanket on the shelf edge and upper slope in the northern GoP.

4.2 Background

4.2.1 PNG Geology

The immense flux of siliciclastic sediments being delivered to the GoP shelf and slope has its origin in the high Papuan mountains created by tectonic collision and uplift since the Oligocene [*Davies et al*., 1989]. This siliciclastic sediment load first filled the troughs between already drowned carbonate platforms (formed since the Miocene) and then covered the platform tops with ~2 km of sediments [*Davies et al*., 1989; *Sarg et al*., 1996; *Tcherepanov et al*., 2008]. The shelf edge on the western GoP is located approximately 150 km from the coast while on the eastern side, shelf edge is very close to the coast and narrows to less than 20 km from the coast (**Figure 4.1**) [*Wolanski and Alongi*, 1995; *Walsh and Nittrouer*, 2003]. Sediments delivered from Papua New Guinea (PNG) rivers have accumulated over time in adjacent Ashmore, Pandora, and Moresby Troughs and deeper seabed regions. However, the presence of active carbonate

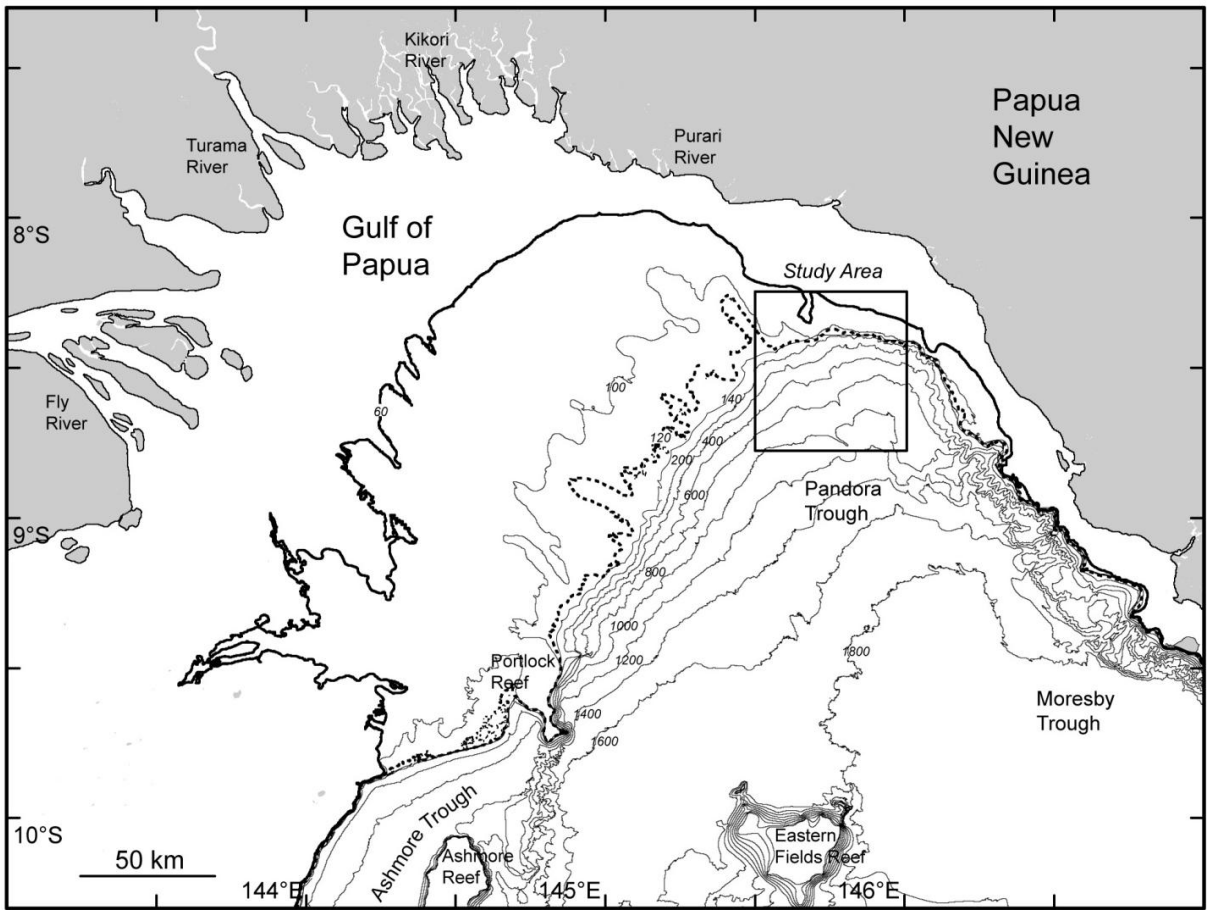

Figure 4.1 Gulf of Papua. The contour intervals are given in meters. The dark line at the 60 m isobath is the seaward extent of prograding Holocene clinoform. The dashed line at the 120 m isobaths shows the LGM coastline while the approximate depth of modern shelf break is at the 140 m isobath. Core locations in the Study Area box are shown in Figure 4.2.

platforms in the southwestern part of GoP suggests that the most active terrigenous sediment flux is confined to the northern Pandora and Moresby Troughs [*Winterer*, 1970; *Harris et al*., 1996; *Walsh et al*., 2004; *Patterson*, 2006].

Subaqueous deltaic stratigraphy has been observed on several continental margins [*Wright and Coleman*, 1973; *Nittrouer et al*., 1986; *Alexander et al*., 1991; *Kuehl et al*., 1997; *Allison et al*., 2000; *Roberts et al*., 2004; *Cattaneo et al*., 2007]. Sedimentary deposits on the continental margins known as clinoforms [*Mitchum et al*., 1977] are considered as one of the fundamental building blocks of stratigraphic record. The sediments deposited by PNG rivers on

the GoP continental shelf since Holocene have formed a clinoform structure **(Figure 4.1)** influenced by a combination of sea level, sediment supply variation, physical oceanography and tectonic subsidence [*Wolanski and Alongi*, 1995; *Walsh et al*., 2004; *Slingerland et al*., 2008a].

4.2.2 Physical Regime

Sediments on to the GoP shelf are delivered by a combination of tidal, wind-driven, and bottom currents [*Wolanski and Alongi*, 1995; *Slingerland et al.*, 2008b]. In the western GoP, close to the Fly river, mean spring tide can be 4 m [*Wolanksi and Eagle*, 1991] while in the eastern GoP, this range can be ~3 m [*Thom and Wright*, 1983].

The GoP shelf experiences two dominant wind-driven currents influenced by seasonal monsoon and trade winds [*Wolanski et al.*, 1995; *Walsh et al*., 2004]. The monsoon winds from northwest last from December to March and are generally weak (1–2 m s^{-1}) [*Slingerland et al*., 2008b]. Trade winds during May to October are strong (4–5 m s^{-1}), sustained, and from the southeast and with a large fetch over the GoP [*Walsh et al*., 2004; *Slingerland et al*., 2008b].

Water circulation in the GoP is driven by the northern component of South Equatorial Current known as the Coral Sea Current (CSC) [*Burrage*, 1993]. The CSC is a large clockwise gyre that sweeps along the outer shelf of the GoP from the south and travels along the southern PNG shelf and slope before exiting the GoP to the east [*Andrews and Clegg*, 1989; *Wolanski and Alongi*, 1995].

Sediments from the PNG rivers are transported to the northern shelf edge and slope of the GoP by clockwise circulation of the water mass in the gulf [*Brunskill et al*., 1995; *Harris et al*., 1996; *Keen et al*., 2006]. Therefore, the northern shelf edge and slope of the GoP provide an ideal location to study the sediment dispersal-system.

4.3 Methods

This study focuses on three jumbo piston cores, MV-41, MV-46 and MV-49 (**Figure 4.2**), recovered from the northern GoP shelf, upper and middle slope, during the R/V Melville cruise in March-April 2004. Seismic data from the PANASH cruise show this region to contain a sediment wedge extending from the shelf edge to the lower slope [*Francis et al.*, 2008]. These cores were taken from this sediment wedge because they are representative of the regional processes active on the northern GoP shelf slope region and potentially have a high-resolution stratigraphic record. Core length and water depth, in meters, for each core are given in **Table 4.1**.

4.3.1 Shipboard Analyses

4.3.1.1 Geophysical Data

The geophysical dataset includes 8000 km of multi-beam, 3.5 kHz seismic collected aboard the R/V Melville (**Figure 4.3**) and a newly created bathymetric grid[*Daniell*, 2008]. The bathymetric grid created for the region included multibeam sonar surveys, hydrographic data sets, and Landsat imagery [*Daniell*, 2008]. Multi-beam surveys of the GoP shelf were conducted using Simrad EM3000 system which has a single acoustic head generating 127 beams that cover a total swath (swath coverage approximately four times the water depth) of 130 degree at a frequency of 300 kHz [*Crockett et al*., 2008]. Slope data were collected with the SEA BEAM 2000 multiple narrow beam 12 kHz swath mapping system which consists of a 120 degree, hull mounted, 12 kHz transducer system and produces bathymetry, depth and cross-track distance (http://shipsked.ucsd.edu/ships/melville/section4.html). Echosounder data were acquired using a Knudsen Engineering Limited system with a 320B/R transceiver unit capable of 10 kW output in 3.5 kHz mode [*Francis et al*., 2008].

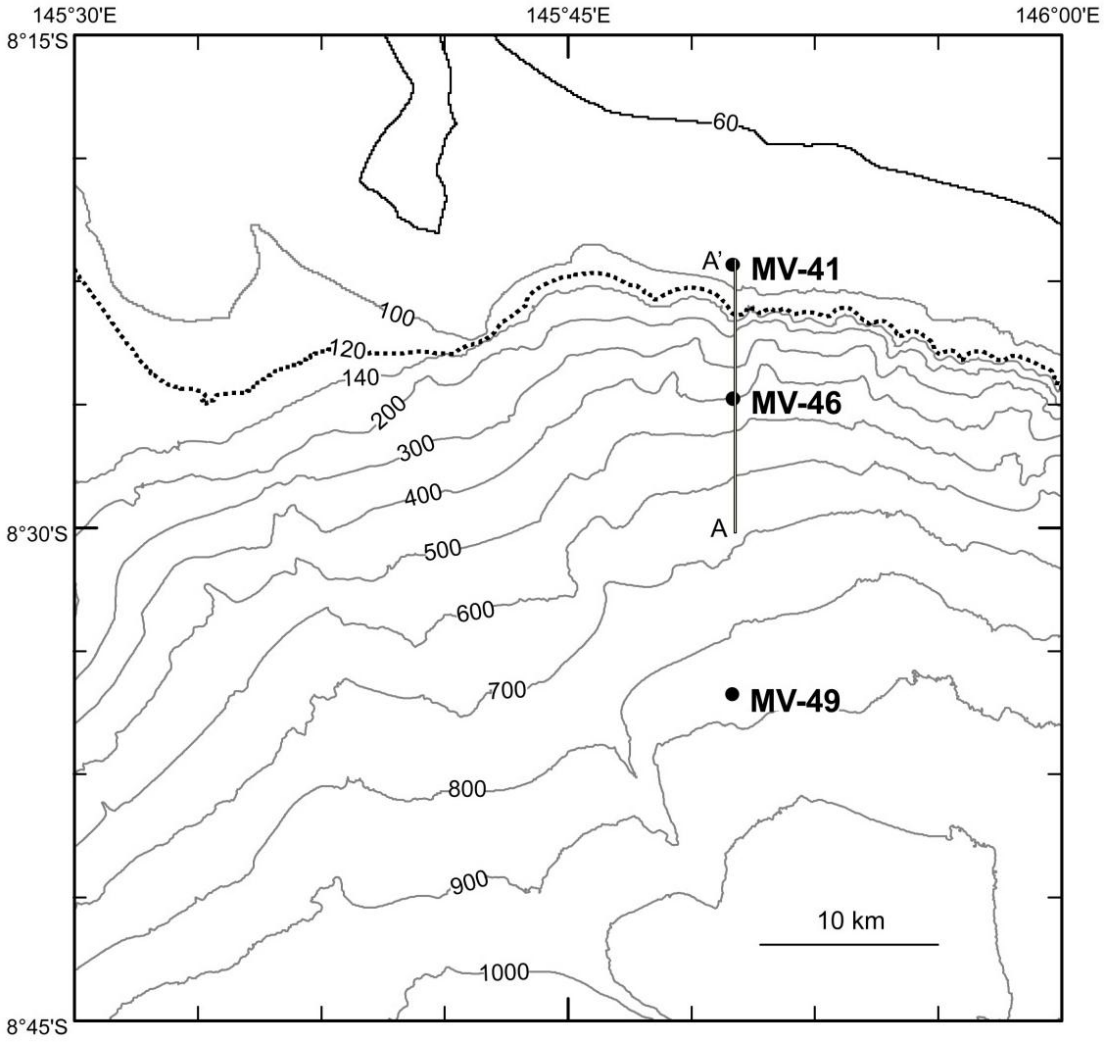

Figure 4.2 Core locations in the study area with contour intervals given in meters. The dark line at the 60 m isobath is the seaward extent of prograding Holocene clinoform. The dotted line at the 120 m isobaths shows the LGM coastline while the approximate depth of modern shelf break is at the 140 m isobath. The dark line on cores MV-41 and MV-46 is the transect AA' seismic profile shown in Figure 4.3.

Table 4.1 Jumbo piston cores collected during PANASH cruise and used this study

Core name	Core length (m)	Latitude	Longitude	Water depth (m)
MV-41	12.84	-8.370	145.867	92
MV-46	14.48	-8.435	145.834	399
MV-49	11.21	-8.585	145.833	859

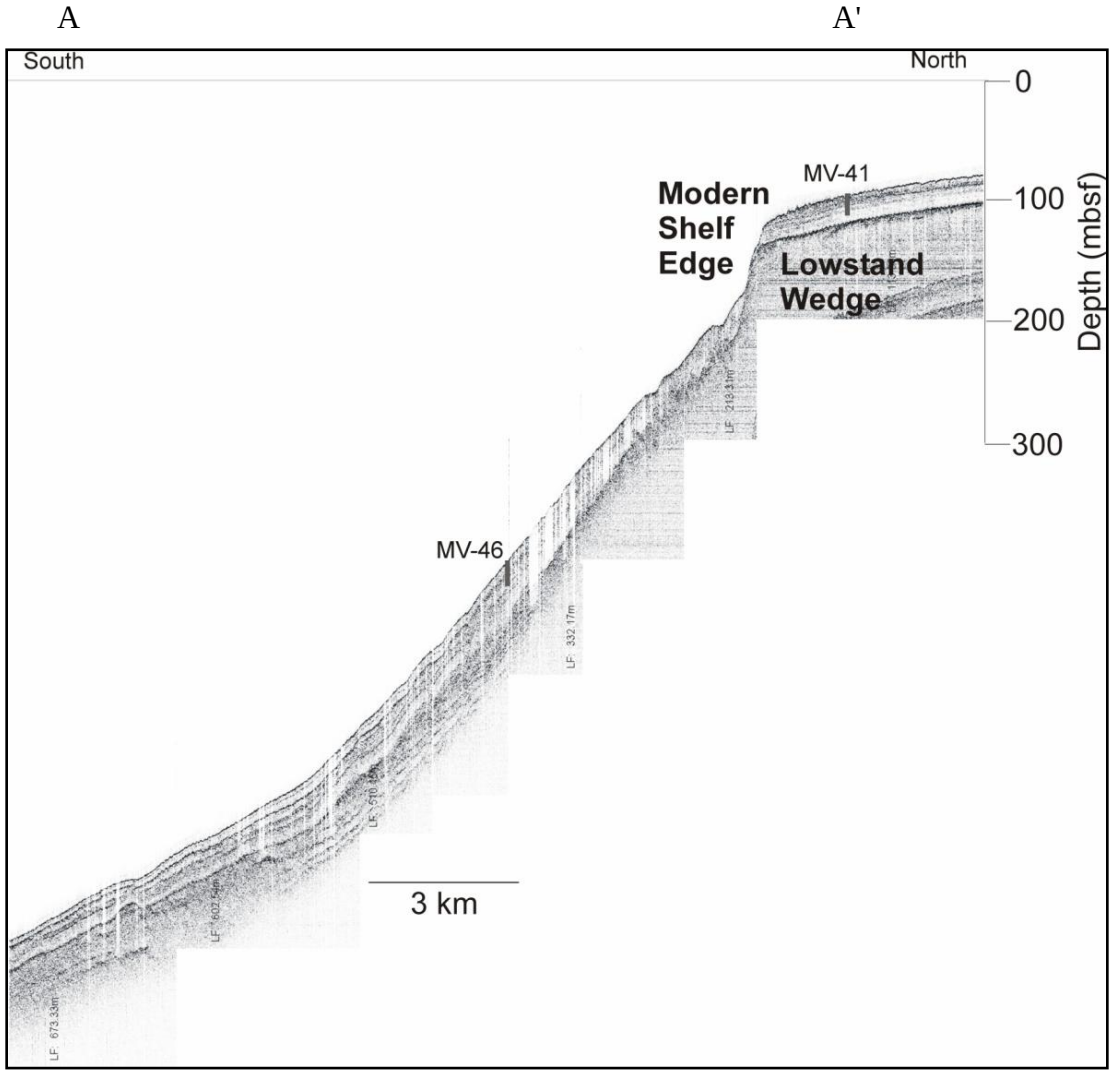

Figure 4.3 Seismic profile acquired from the northern Pandora Trough shelf edge and upper slope region showing the prograding Holocene sediment wedge and cores MV-41 and MV-46.

4.3.1.2 Gamma Density and Magnetic Susceptibility

Unsplit cores were analyzed for gamma density and magnetic susceptibility using a GEOTEK® [*GEOTEK*, 2003] Multi-Sensor Core Logger (MSCL) while aboard ship. Gamma density was calculated from the attenuation of gamma rays emitted from a 10 milli-Curie ^{137}Cs source transmitted through sediment cores. Grain density was assumed to be 2.65 g cm^{-3} and water density assumed as 1.027 g cm^{-3}. GEOTEK® MSCL-derived gamma density units are reported here in g cm^{-3} [*Weber et al*., 1997]. Volume-corrected magnetic susceptibility (MS) measurements, carried out using a loop sensor on R/V Melville, are reported in 10^{-5} SI units.

4.3.2 Postcruise Analyses

4.3.2.1 Digital Imaging

Split piston cores were imaged with a GEOTEK® GEOSCAN high-resolution digital camera system, which provided high-resolution color imagery and multichannel sediment color data (**Figures 4.4, 4.5 and 4.6**). The GEOSCAN collects digital images using a linescan camera linked to the MSCL core conveyor stepper motor to generate synchronous output of image data. The system consists of three individual interference filters located in front of each of three 1024 CCD line arrays inside the camera body. High resolution images are created in terms of three color components (red, blue, green) using a image resolution of 300 dpi (dots per inch) and imaging speed of 5 minutes per 1.5 m core section [*GEOTEK*, 2003]. Output files consist of core images created in BMP format giving cross-platform compatibility with different image processing softwares. Imaging took place after cores were returned to the USA, so colors reflect oxidation processes that occurred during storage and transit.

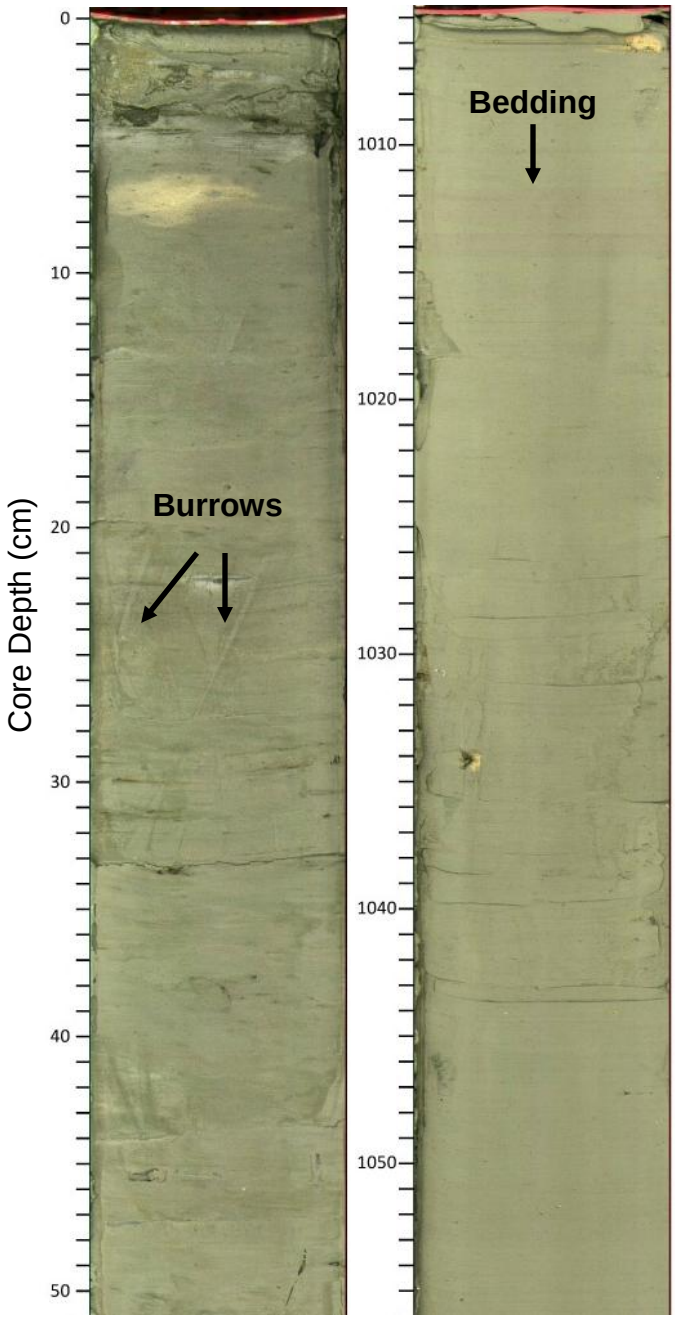

Figure 4.4 Digital images of the sections of core MV-41 showing burrow in the upper 30 cm and bedding between 1010-1020 cm.

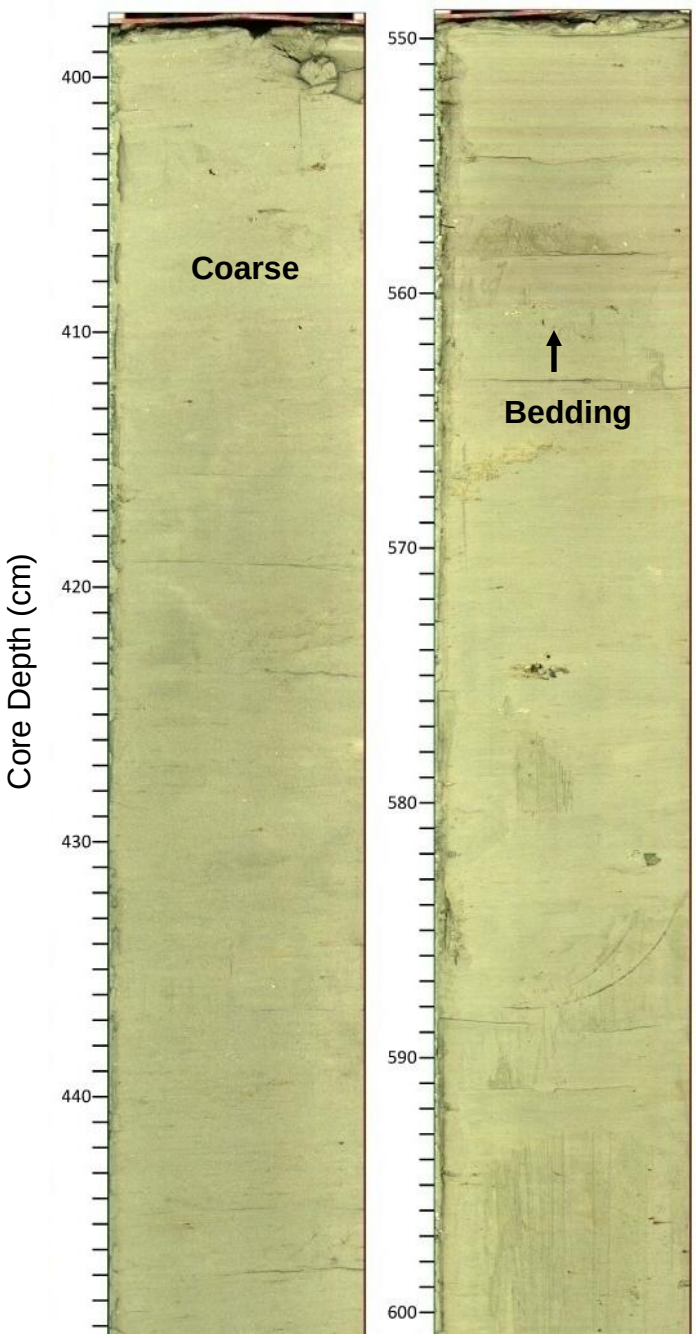

Figure 4.5 Digital images of the sections of core MV-46 showing coarse fraction in the upper 400 cm and bedding between 550-560 cm.

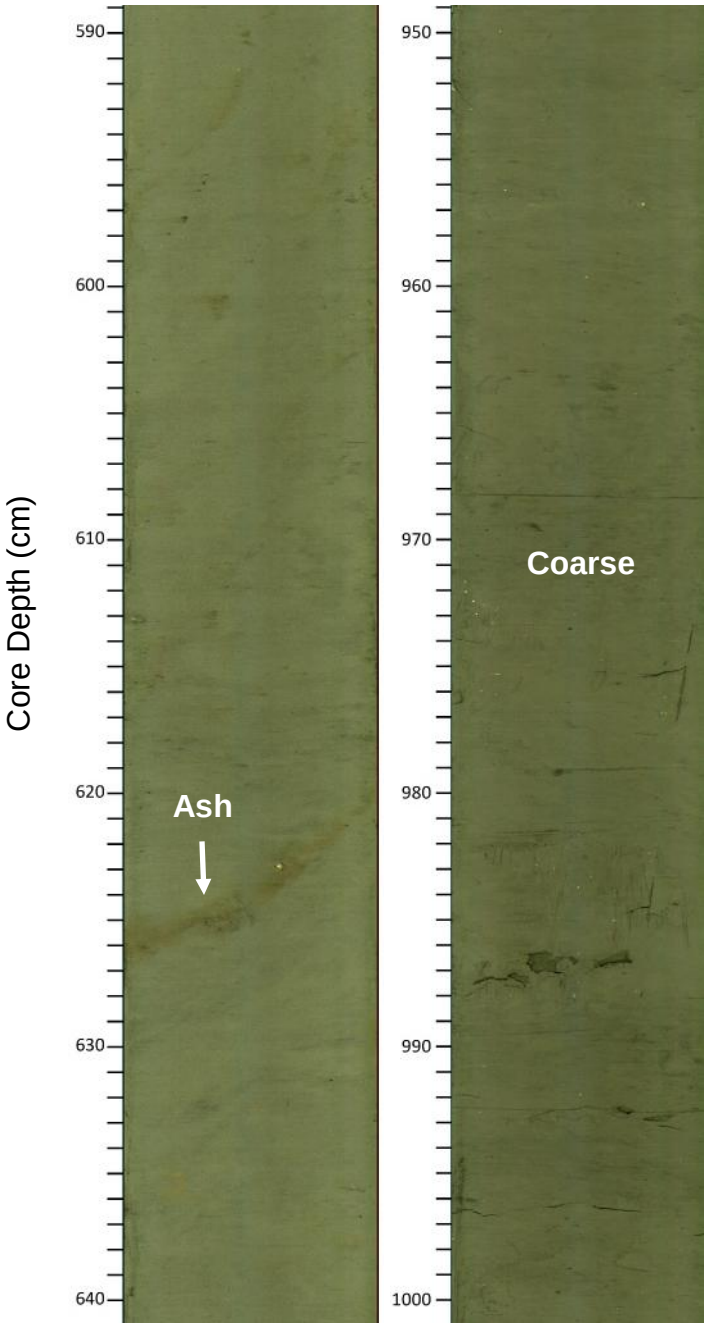

Figure 4.6 Digital images of the sections of core MV-49 showing the ash layer at ~625 cm and coarse fraction between 950-1000 cm.

4.3.2.2 Grain Size

Samples were wet-sieved to separate coarse (> 63 μm) fraction from fine (< 63 μm) fraction. Samples were dried for 24 hours at 60°C and masses were subtracted from total to determine the percentage of coarse and fine fractions.

4.3.2.3 Radiocarbon Analyses

Radiocarbon analyses were carried out on wood samples from cores MV-41, MV-46 and MV-49 at the Woods Hole Oceanographic Institution Accelerator Mass Spectrometery (AMS) facility. Bulk sediment samples were wet-sieved on a 63 μm sieve with deionized water and 5-10 mg of woody organic matter was hand-picked under microscope for analysis. All radiocarbon dates are based on wood samples with a fibrous wood texture visible under the binocular microscope.

Calibration of radiocarbon ages is done to take into consideration secular variations in ^{14}C production in the atmosphere [e.g. *Damon et al*., 1978]. Radiocarbon ages were calculated using 5568 years as the half-life of radiocarbon and calibrated to calendar ages using the Radiocarbon Calibration Program [*Fairbanks et al*., 2005] which uses a hierarchical Bayesian statistical model. Radiocarbon ages are reported in thousands of years before present (ky BP), where present is defined as 1950 AD. Because the wood particles have been transported over time from their terrestrial sources, these ages represent maximum estimates for the deposits under study.

4.3.2.4 Mass Accumulation Rates

Mass accumulation rates (MAR) for the bulk sediment were calculated as:

$$MAR = (1-\Phi)\times\rho_s\times LSR$$

where LSR is the linear sedimentation rate in cm ky^{-1} determined by dividing sediment thickness

of a give interval by time (measured from ^{14}C) where Φ is the average porosity for the core, and ρ_s is the density of sediment grains (assumed to be 2.65 g cm^{-3}).

4.4 Results

4.4.1 Cores Description

All split core sections were visually described for lithology, sedimentary structure and any visible features (**Figure 4.7**).

Core MV-41 was taken from a water depth of 92 m near the shelf edge and recovered approximately 1300 cm of sediment cover and consists of predominantly green mud. The upper 20-30 cm of the core is marked with burrows and shows a gradual color transition from greenish grey to green (**Figure 4.4**). Plant matter and pyrite are distributed along the entire core as observed through a binocular microscope (**Figure 4.8**). Parallel lamination in red-brown mud is well preserved at ~1000 cm (**Figure 4.4**) below which is a dark bluish grey deposit extending to about 1100 cm which gradually changes to green.

Core MV-46 on the upper slope consists of apparently homogenous olive mud as revealed with a sediment recovery of more than 1400 cm. A poorly sorted coarse interval is present at 350-450 cm (**Figure 4.5**). Selected samples were studied under binocular microscope and some of these samples consist of foraminifer-rich mud interpreted as hemipelagics (**Figure 4.9**). Red-brown mud lamination is present at the 550-560 cm overlain by a darker green interval at the 400-500 cm. The void at the 1350-1415 cm could be due to gas hydrates which are formed on continental margins under suitable temperature, pressure and local chemical conditions (**Figure 4.7**).

Core MV-49 taken at a water depth of 859 m recovered ~1100 cm of green mud. Visual observation shows ash layers at ~270, ~390 cm, and ~625 cm intervals (**Figure 4.6**). Between

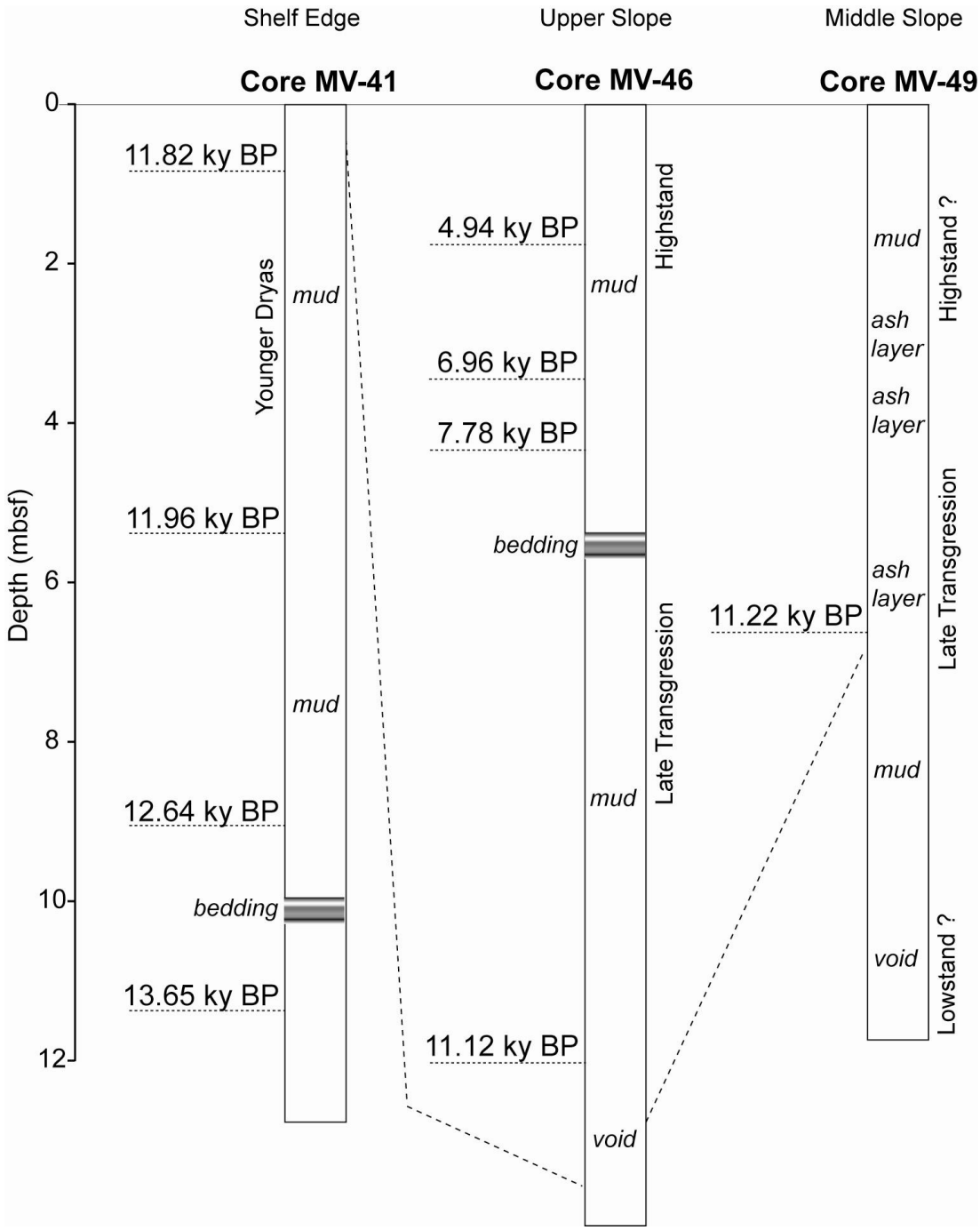

Figure 4.7 Interpretive core logs of the sediments recovered from shelf-edge and upper slope on the Pandora Trough. Age controls are shown by radiocarbon dates and core lengths are given in meters below seafloor (mbsf).

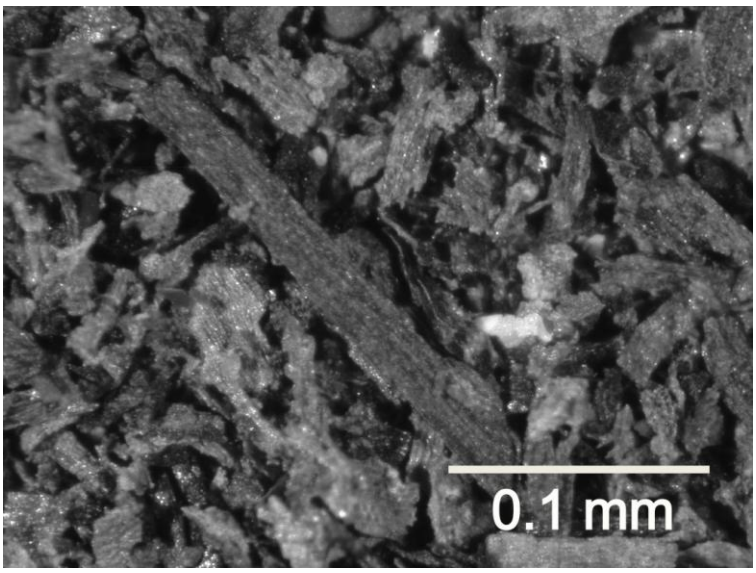

Figure 4.8 Photomicrograph of coarse fraction (> 63 μm) from core MV-41(61-63 cm interval) showing abundant wood pieces.

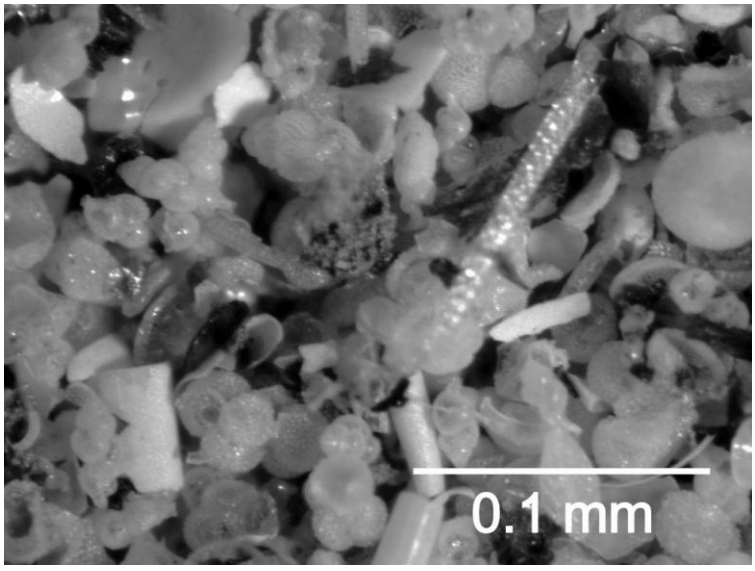

Figure 4.9 Photomicrograph of coarse fraction (> 63 μm) from core MV-46 (413-415 cm interval) showing foraminera-rich fraction.

950-1050 cm interval, visual observations show core lithology marked by poorly sorted coarser grain size (**Figure 4.6**). Basal portion of the core at ~1080 cm has a void that could result from gas hydrates under suitable temperature-pressure conditions similar to the one observed in core MV-46.

4.4.2 Gamma Density and Magnetic Susceptibility

Gamma density (GD) peaks may be indicative of coarser grain size in bulk sediment and magnetic susceptibility (MS) peaks provide evidence for increased concentrations of Fe-containing minerals. In all the three cores, increase in GD in bulk sediment generally seems to closely co-vary with MS peaks. Gaps in GD and MS profiles are due to section breaks in core. The GD profile for core MV-41 profile shows an average value of 1.5 g cm^{-3} with slight variations downcore (**Figure 4.10**). Prominent peaks occur at 250 cm where GD increases to 1.7 g cm^{-3} followed by two more peaks at 378 and 408 cm where GD increases to 1.6 g cm^{-3}. A region of low GD occurs between 950 and 1000 cm followed by an increase further down to the base of the core. The MS profile for core MV-41 shows cyclic patterns with few prominent peaks. Two large peaks occur in the upper 250 cm of core MV-41 below which there is a region of low MS after which MS increases again at ~300 cm with several peaks. From 950 cm to the bottom of the core, MS values stay almost constant at ~20×10^{-5} SI . Except for the upper 300 cm, GD and MS appear to covary.

Core MV-46 shows an increase in GD from 1.6 to 2.2 g cm^{-3} in the upper 400 cm and shows a uniform GD around 2.0 g cm^{-3} below 400 cm with gentle fluctuations (**Figure 4.11**). Between 850 and 1000 cm, GD fluctuates at relatively low values of 1.9 g cm^{-3} before it rises and remains uniform around 2.0 g cm^{-3} below this depth. Another region of relatively low GD occurs between 1350 and 1400 cm where GD decreases to around 1.7 g cm^{-3}. With few peaks in

the upper 1000 cm, MS is relatively uniform around 10×10^{-5} SI. A region of minimum MS occurs around 350 cm followed by a major peak between 400 and 500 cm where MS rises to more than 20×10^{-5} SI. Between 550 and 660 cm, MS decreases to around 5×10^{-5} SI. Another MS peak occurs around 930 cm where MS rises to above22×10^{-5} SI. Below 1000 cm is a region of uniform MS with a minimum at 1350-1400 cm where MS decreases to around 5×10^{-5} SI.

Core MV-49 shows GD almost in the same range as MV-41 although MV-49 has a relatively more uniform profile (**Figure 4.12**). GD values show a downward step-wise increase from 1.3 g cm^{-3} to 1.5 g cm^{-3} in the upper 200 cm and remains around 1.5 g cm^{-3} up to 900 cm. Below 900 cm GD again rises to 1.55 g cm^{-3} and shows a fluctuating pattern from 1030 cm to the bottom of the core. For core MV-49, MS values show higher fluctuations than cores MV-41 and MV-46. A gradual increase in MS is seen from the core top to 400 cm with two prominent peaks at 48.5 cm and 158 cm. In this core section, MS rises to above 40×10^{-5} and then decreases abruptly to a low between 480 and 540 cm, followed by another rise and a prominent peak at 642 cm where MS again rises above 40×10^{-5} SI. With minor fluctuations, MS values stay high in the range of 30-35×10^{-5} SI below 700 cm to the bottom of the core.

4.4.3 Grain Size

Sediments in the northern Pandora Trough shelf edge and slope are predominantly mud (more than 90%) with slight downcore variations.

Mud content in core MV-41 generally exceeds 98% of the bulk sediment (**Figure 4.10**). Younger sediments in the upper 200 cm show two prominent peaks where mud content decreases to ~93% at the 102 and 145 cm intervals. Between 569-621 cm, mud content decreases slightly to 97%. Below this interval, older sediments of the core show a mud content of ~98%.

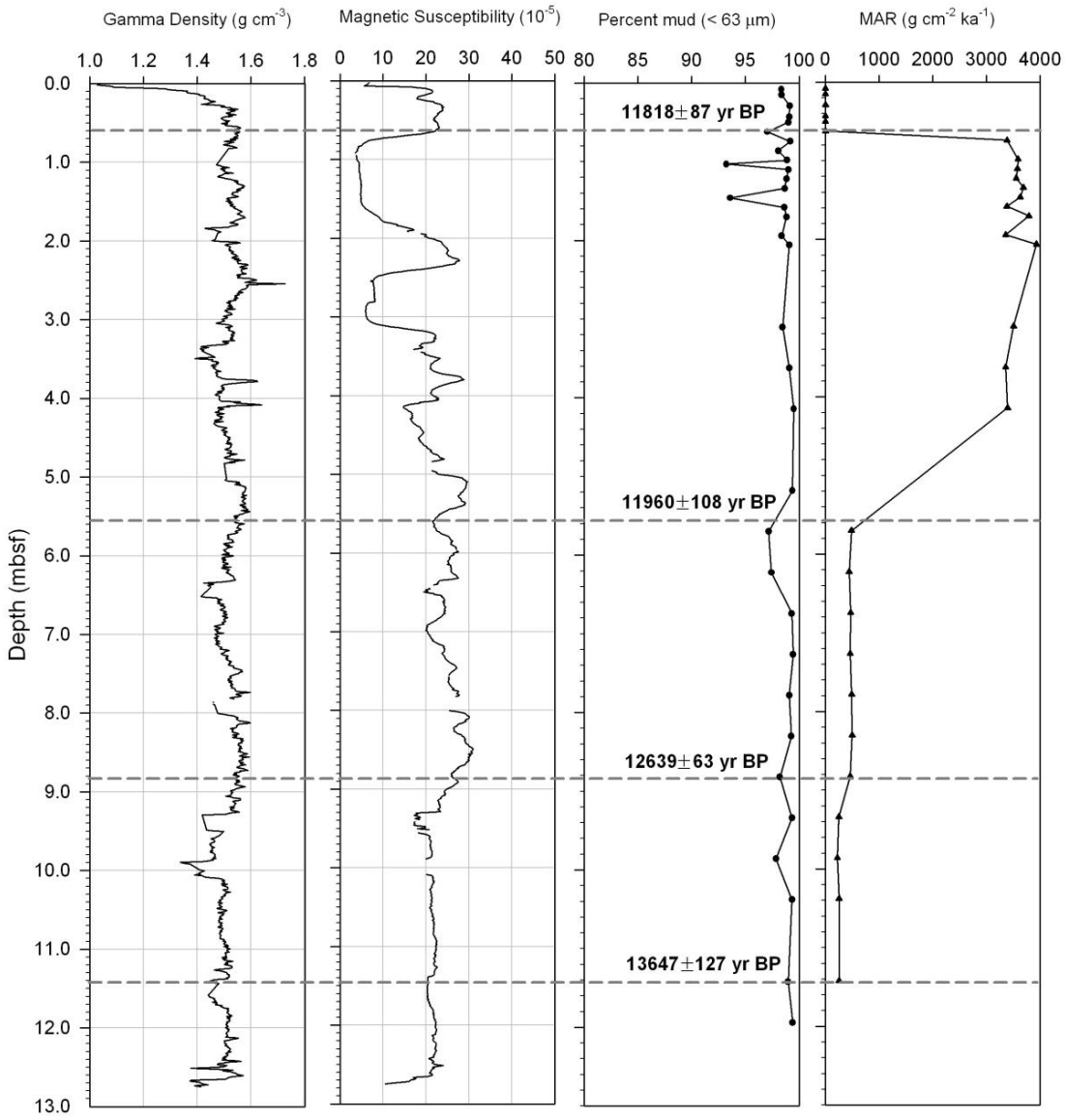

Figure 4.10 Gamma density, magnetic susceptibility, mud content (percent silt and clay (< 63 μm)) and mass accumulation rates (MAR) for the core MV-41used in this study.

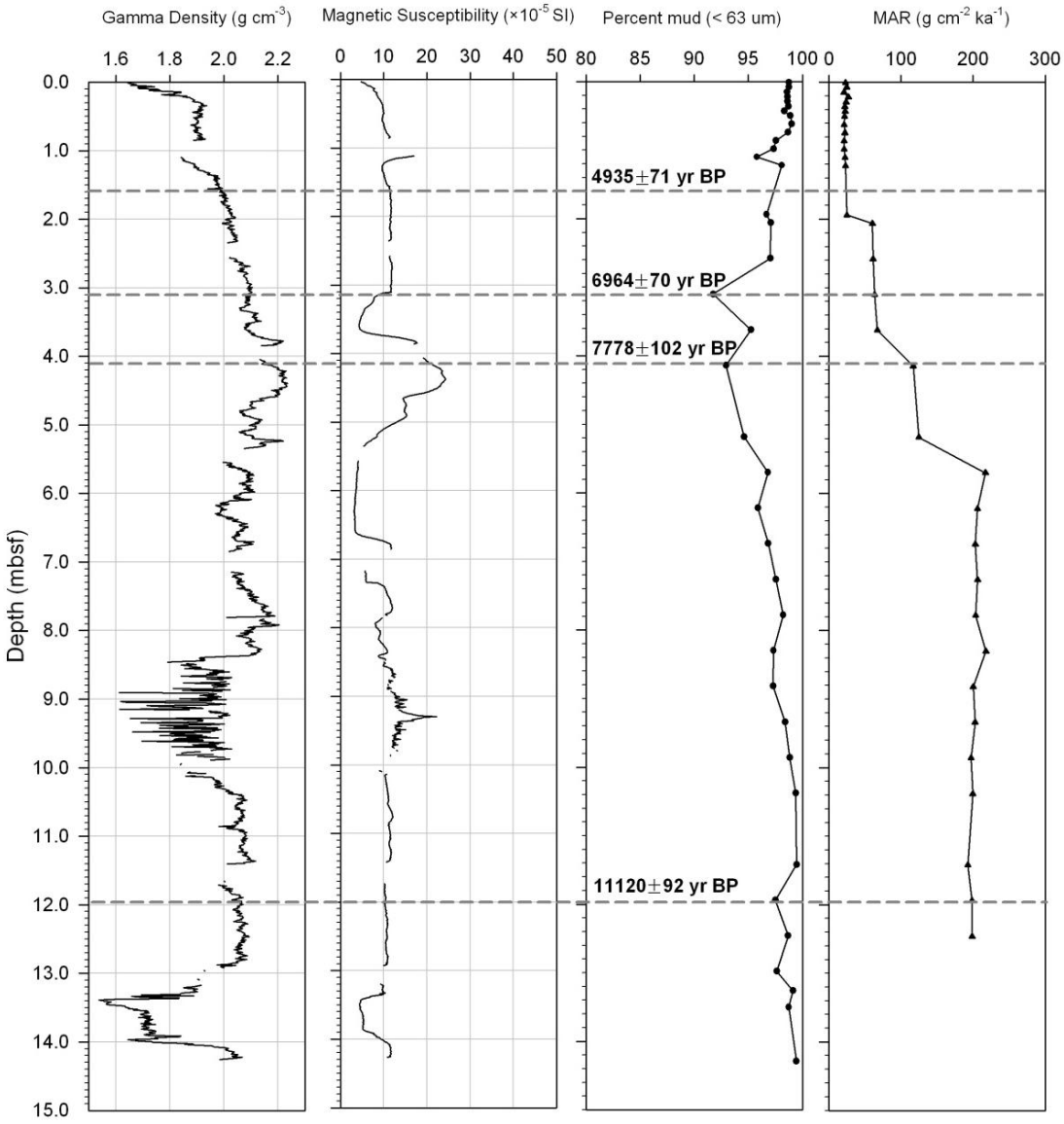

Figure 4.11 Gamma density, magnetic susceptibility, mud content (percent silt and clay (< 63 μm)) and mass accumulation rates (MAR) for the core MV-46 used in this study.

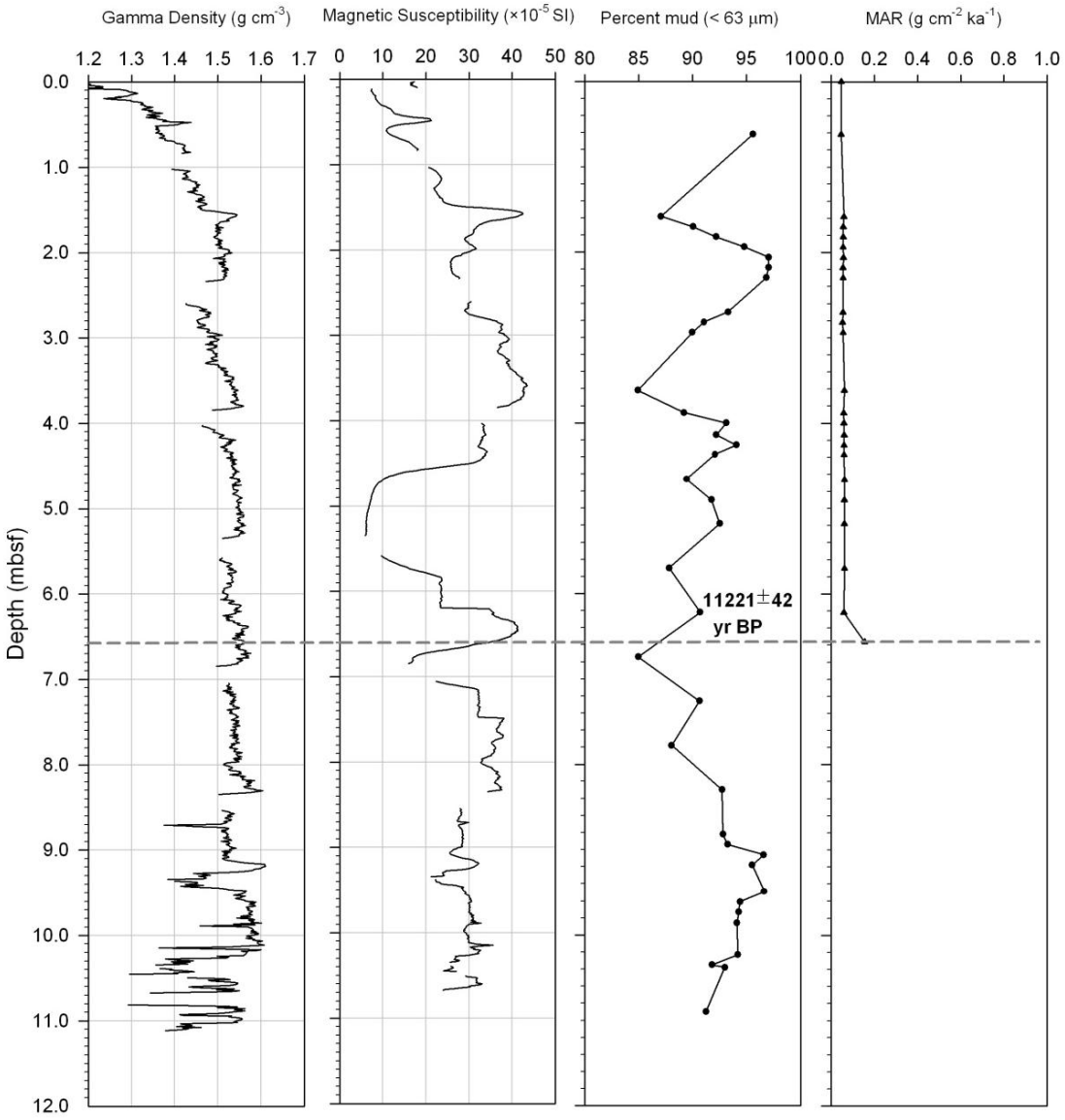

Figure 4.12 Gamma density, magnetic susceptibility, mud content (percent silt and clay (< 63 μm)) and mass accumulation rates (MAR) for the core MV-49 used in this study.

In core MV-46, mud content accounts for more than 90% of the bulk sediment (**Figure 4.11**). The most pronounced increase in grain size occurs from core top to ~300 cm, where the mud content decreases from 97 to 90%. Below this interval, the mud content increases to ~99% below 1000 cm. Basal portion of the core, below 1100 cm, shows a decrease in the mud content to ~97%.

The average mud percent observed in core MV-49 is ~92% of the bulk sediment and fluctuates between 85-95% down the length of the core (**Figure 4.12**). This mud content shows a maximum of 97% at 200 cm depth and ~900 cm depth.

4.4.4 Radiocarbon

Ages are reported as conventional ^{14}C years before present. The cores from this study area span the time range of ~4 to 12 ky (calendar years) BP (**Table 4.2**). Calibrated AMS ^{14}C dates taken from core MV-41 range between 11.82 to 13.65 ky BP while core MV-46 shows a record of 4.94 to 11.12 ky BP. Only one radiocarbon date was obtained from core MV-49 at the 656-657 cm interval dated at 11.22 ky BP.

4.4.5 Age-Depth Model

Sea level curves of the last deglaciation in the New Guinea region have been constructed by means of radiocarbon dating of corals [*Chappel and Polach*, 1991; *Ota et al*., 1993], terrestrial organic matter [*Hanebuth et al*., 2000], and foraminifera [*Yokoyama et al*., 2000] (**Figure 4.13**). From these and other records [*Carter and Johnson*, 1986], the emerging model of the eustatic late-to postglacial sea level rise has been that of a step- wise sea level rise with several pauses or even regression in between [e.g. *Liu et al*., 2004].

The radiocarbon dates from cores MV-41, MV-46 and MV-49 are used to construct an age-depth model to reveal sediment mass accumulation rates on the GoP shelf and slope (**Figure 4.14**). In order to extract the linear sedimentation rate, we assume that the piston core top is the

Table 4.2 Conventional and calibrated radiocarbon ages used in this study from the northeastern Pandora Trough. Radiocarbon ages were calculated using 5568 years as the half-life of radiocarbon. Calibration was done using the *Fairbanks et al*., [2005] method.

Core I.D. (cm)	Core interval (years BP)	^{14}C ages (conventional) (years BP)	^{14}C ages (calibrated)
MV-41	61-63	10150±35	11818±87
MV-41	552-553	10225±58	11960±108
MV-41	881-883	10700±70	12693±63
MV-41	1143-1145	11800±140	13647±129
MV-46	156-157	4380±40	4935±71
MV-46	309-311	6100±50	6964±71
MV-46	413-415	6950±100	7778±102
MV-46	1193-1195	9680±50	11120±92
MV-49	656-657	9810±65	11221±42

sediment surface and has an age of 0 ky BP. Radiocarbon dates from core MV-41 show that the shelf-break experienced an increasing sedimentation rate from 13.65 ky BP to11.82 ky BP (**Figure 4.14**). Assuming that our core top is not reworked, the upper 500 cm of core MV-41 between 11.96 ky BP and 11.82 ky BP experienced a very rapid sedimentation rate of ~3500 cm ky^{-1} which is a maximum estimate.

Sedimentation rates on the upper slope (core MV-46) decreased step-wise from 233 cm ky^{-1} to 32 cm ky^{-1} between 11.12 ky BP and ca. 6.5 ky BP when the sea level reached highstand [*Thom and Roy*, 1983]. Because we have only one radiocarbon date available for the core MV-49, we calculate a constant sedimentation rate of 59 cm ky^{-1} between 11.22 ky BP and present, for the middle slope.

4.4.6 Mass Accumulation Rates

Sediment mass accumulation rates (MAR) for cores MV-41, MV-46 and MV-49 have been plotted along with MSCL data and grain size (see **Figures 4.10**, **4.11**, and **4.12**). At the shelf edge (core MV-41), MAR values show increase between 13.65 and 11.96 ky BP and reach a maximum of ~3900 g cm^2 ky^{-1} between 11.96 and 11.82 ky BP and abruptly decrease to

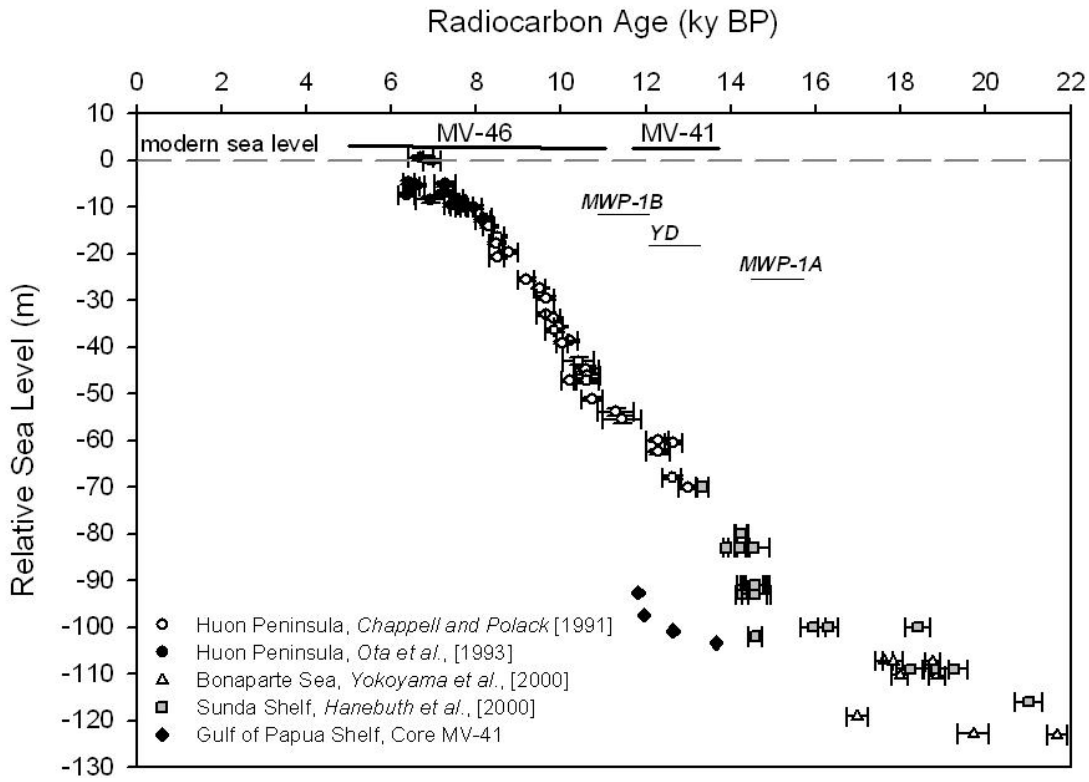

Figure 4.13 Ages and depths of MV-41 samples with post-LGM sea level curve showing data from Huon Peninsula (*Chappell and Polach* [1991]; *Ota et al*., [1993]), Bonaparte Sea (*Yokoyama et al*., [2000]), Sunda Shelf (*Hanebuth et al*., [2000]) and core MV-41 on the shelf edge in the northern Gulf of Papua. Dark horizontal lines above the modern sea level (indicated by a dashed line) show age ranges for cores MV-41 and MV-46. Major meltwater pulse events included were (MWP-1A and 1B) as well as the Younger Dryas (YD). MV-41 dates do not represent sea level, but are shown to place core in the context of sea level and core depth and time of deposition.

5 g cm^2 ky^{-1} above 11.82 ky BP assuming a modern age for the core top. On the upper slope (core MV-46), MAR values decrease step-wise from ~200 g cm^2 ky^{-1} to ~25 g cm^2 ky^{-1} from 11.12 ky BP till after sea level reached its present level, ca. 6.5 ky BP. From 4.94 ky BP to present, MAR average around 23 g cm^2 ky^{-1} on the upper slope. Based on only one radiocarbon date from core MV-49, the average MAR on the middle slope is 0.061 g cm^2 ky^{-1} between 11.22 ky BP and present.

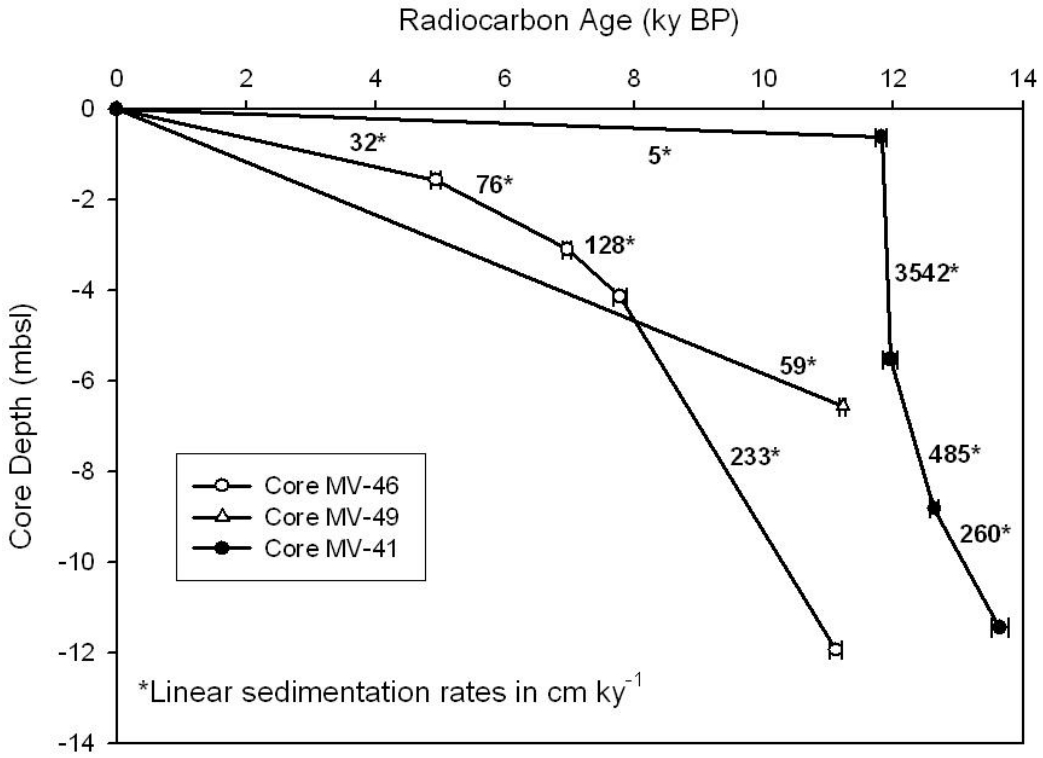

Figure 4.14 Age model curve showing radiocarbon ages versus core depth for cores MV-41, MV-46, and MV-49.

4.5 Discussion

Based on the sedimentary structure, ages and delivery of the sediment flux, and study cores, a post-LGM depositional history can be reconstructed for GoP shelf/slope region. In conjunction with the sea level curves drawn for the western Pacific region, the depositional history from GoP can be linked to the global sea level and climatic changes since the Late Pleistocene.

During the LGM interval, defined here as the time period between 23-19 ky BP, global tropical sea-surface tempateratures dropped by several degrees [*Guilderson et al*., 2000; *Visser et al*., 2003] resulting in a decrease in eustatic sea level below present levels [*Weaver et al*., 2003]. During this period, sea level in the western Pacific dropped to ~ -120 m (**Figure 4.13**) [e.g. *Yokoyama et al*., 2000]. The GoP shelf, which had been receiving terrigenous sediments since

Pliocene [*Gardner*, 1970; *Beiersdorf*, 1989] was subaerially exposed during LGM and PNG rivers delivered terrigenous sediments closer to the modern shelf edge [*Febo et al*., 2008]. Thinly bedded sandy turbidites interlayered with hemipelagic units observed in central Pandora Trough during sea level lowstand suggest gravity flows [*Patterson et al*., 2006; *Jorry et al*., 2008], although the sources of these deposits have not been confirmed. A series of meltwater pulse (MWP) events related to climatic fluctuations and ice dam failures caused the post-LGM sea level to rise in a step-wise pattern in the western Pacific [e.g., *Liu et al*., 2004].

Our cores from the GoP shelf edge (core MV-41) and upper slope (core MV-46) recovered post-LGM sediments. The undated basal portion of core MV-49, recovered from the middle slope, may represent sediments deposited prior to meltwater pulse events or during the LGM. For this study, the time interval for the shelf-upper slope cores is divided into Middle Transgression (14-10 ky BP), and Late Transgression and Highstand (10-0 ky BP).

4.5.1 Middle Transgression (14-10 ky BP)

After the rapid sea level rise of MWP-1A, around 14.6-14.1 ky BP [*Weaver et al*., 2003], during which time sea level rose from -95 to -80 m [*Fairbanks*, 1989; *Hanebuth et al*., 2000], sea level rise slowed down ca. ~12.5 ky BP. This period is also known as Younger Dryas (YD) (ca. 11.9 ky BP) and is associated with an increase in sediment delivery to the GoP shelf region [*Jorry et al*., 2008]. Sea level again rose from -58 to -43 m ca. 11.6 ky BP, also known as MWP-1B [*Fairbanks*, 1989] during more warmer conditions. We apply here the principle of sequence stratigraphy; a rise in sea level decreases the river gradient resulting in reduced fluvial deposition at the shelf edge [*Posamentier and Vail*, 1988; also see *Bhattacharya and Walker*, 1992]. This rapid sea level rise may have essentially shut off sediment supply from northern PNG rivers to the continental shelf also revealed by AMS ^{14}C date of 11.82 ky BP in the upper 61-63 cm in core MV-41.

The transgressive sedimentary deposits on GoP outer shelf suggests a prodelta environment because of proximity to shoreline and a relatively homogenous mud. The age-depth model shows that GoP shelf was an active region of sediment accumulation ca. 14-10 ky BP (**Figure 4.13**). Sediments deposited at the shelf edge after ~13 ky BP show variations in GD and MS values suggesting sediments coming either from the volcanic sources in the eastern PNG [*Davies and Smith*, 1971; *Slingerland et al*., 2008a] or the limestone and aluminosilicate terrain from the western PNG [*Brunskill*, 2004]. These sediments could be deposited from physical processes such as waves, tidal or bottom currents, or high-magnitude but low frequency events such floods [*Slingerland et al*., 2008a], or gravity flows [e.g. *Harris et al*., 1996]. The bedding observed in core MV-41 may have been deposited from such an event (**Figure 4.4**). Assuming that the AMS ^{14}C dates of 11.82 and 11.96 ky BP in upper portion of core MV-41 are not reworked, the extremely high MAR of 3900 g cm^{-2} ky^{-1} in the upper 5 meters of core MV-41 seems to correlate with YD (12.5-11 ky BP) when sea level was approximately 60 meter below its present level [*Jorry et al*., 2008], rivers were delivering terrigenous sediments closer to the shelf edge. At this time, the location of core MV-41 was approximately 10 kilometer seaward of the coastline in relatively shallow water (**Figure 4.2/Table 4.3**). After this short glacial reversal when rivers were delivering sediments close to the continental shelf edge, the sea level began to rise again. This sea level rise may have resulted in river-borne sediments being trapped on the aggrading floodplain resulting in a reduced supply to the prograding delta. If processes influencing sediment accumulation during the YD (i.e., winds, tides, waves) were broadly similar to today [e.g. *Slingerland et al*., 2008a; *Slingerland et al*., 2008b], the water depth and location of MV-41 at that time would have been generally conducive to accumulation, if sediment flux was available.

Using the AMS ^{14}C dates from core MV-41 and sea level data (references in **Figure 4.13)**, the water depth at the time when the sample was deposited can be estimated (**Table 4.3**). These water depths are comparable to the modern water depths of highest sedimentation rates in the foreset region of the GoP clinoform. The 'rollover' line for the modern GoP clinoform lies in 20-30 m of water and the foreset extends to a depth of 60 m [*Slingerland et al*., 2008b] where maximum MAR of 3.7-3.8 g cm^{-2} y^{-1} (on a 100-year timescale) have been reported by *Walsh et al*., [2004]. These MAR values are comparable to our MAR values of 3900 g cm^{-2} ky^{-1} in core MV-41 during the YD.

Table 4.3 Comparison between estimated water depth using data from Figure 3.13 and actual water depth using data from core MV-41.

AMS ^{14}C age (ka BP)	Sample depth (mbsl)	Water depth (m) at AMS^{14}C age
11.81	93	18
11.96	98	23
12.69	101	26
13.65	103	28

The post-LGM mud drape on the upper slope (core MV-46) shows relatively higher GD and lower MS than the shelf edge (core MV-41) and middle slope (core MV-49) during this period. Given the proximity of core MV-46 to the shelf edge, the differences in GD and MS values between the shelf and slope suggest that sediments deposited at these sites may have been accumulating under different delivery processes. The wood samples taken for AMS ^{14}C from core MV-46 on the upper slope suggests that some sediment may have been escaping the shelf edge into the deeper Pandora Trough during YD when northern PNG rivers were delivering sediments closer to the continental shelf.

Although the mud content of sediments on the upper slope and middle slope exceeds 90%, higher MS values for the middle slope suggest a relatively higher amount of terrigenous accumulation on the middle slope than the upper slope. Presence of an ash layer in core MV-49 at ~625 cm suggests sediments were being delivered to GoP basins beyond the upper slope. This sediment flux to the middle slope may have been delivered during the brief glacial reversal of YD prior to MWP-1B as revealed by the single AMS ^{14}C date from core MV-49 at 656-657 cm.

4.5.2 Late Transgression and Highstand (10-0 ky BP)

The Late Transgression (10-6.5 ky BP) saw a major sea level rise when sea level rose from from -36 to -16 m [*Liu et al*., 2004]; a rapid sea-level rise during 9.8 to 9.0 cal ky BP is documented in various sedimentary records from the western Pacific (see **Figure 4.13** and references therein). Global climate reached an optimal interglacial regime in the early Holocene ca. 6.5 ky BP, when sea level rose to within several m of its present level [*Lambeck and Chappell*, 2001] resulting in a reduced terrigenous flux being delivered to deep basins in the GoP [*Harris et al*., 1996].

Before the shoreline retreated landward as a result of sea level rise from ~10 ky BP to present, the estimated water depth at the site of core MV-41 was approximately 18-26 m (**Table 4.3**). In shallower water depths closer to the shelf, sediment dispersal across the continental shelf is influenced by physical processes such as wind-driven flows, waves, buoyant plumes, and bottom boundary processes [*Nittrouer and Wright*, 1994]. This influence of coastal processes to transport sediment across shelf diminishes with increasing water depth and increasing distance from the coast. AMS ^{14}C dates from the shelf edge (core MV-41) suggest that sediment supply to the shelf was suppressed when sea level rise rose again after YD during the interglacial conditions of MWP-1B and the shoreline retreated northwards. This pulse of sea level rise created the accommodation space on the outer shelf and decreased the river gradient. The

sediments were deposited on the inner shelf and floodplains and northeastern GoP shelf was starved of the terrigenous input.

Since sea level reached highstand ca. 6.5 ky BP, terrigenous input to the slope and outer shelf GoP from the northern PNG rivers seems to have reduced [*Pickup and Warner*, 194; *Carter and Johnson*, 1986] as revealed by step-wise decreases in sedimentation rates on the upper slope which mimic the regional sea level curve (**Figures 4.13 & 4.14**). AMS ^{14}C dates in core MV-46 suggest that some sediments continued to escape the shelf edge probably by a combination of physical processes such as nepheloid layers in the water column [*Walsh and Nittrouer*, 2003;] as well as waves, tides and gravity flows [*Harris et al*., 1996; *Slingerland et al*., 2008b] even after sea level reached its present level ca. 6.5 ky BP.

The middle slope (core-MV-49) shows relatively low GD and high MS values as compared to core MV-46 on the upper slope. The volcanogenic component in core MV-49, as shown by MS peaks (**Figure 4.12**) is indicative of the multidirectional sediment transport in GoP because these sediments are likely coming from the northern PNG rivers [*Slingerland et al*., 2008a] and mixing with the sediments from eastern rivers [*Brunskill et al*., 1995].

4.5.3 Sedimentary Depositional History

The upper 12 m of the sediment blanket on the GoP shelf edge and middle slope has formed during the latest Pleistocene and Holocene by a combination of depositional processes. S*lingerland et al*., [2008a] have pointed that the growth of Holocene clinoform in the middle shelf continued during MWP-1C (ca 9.6-9.1 ky BP) as a result of accommodation being available at water depths ranging between 25-95 m [see Figure 10 in *Slingerland et al*., 2008a]. The sediment blanket on the shelf and middle slope may have been formed by a mixture of sediments coming from the Fly and its associated tributaries in the west as well as the Kikori, Purari, and other rivers in the northeast [e.g. *Slingerland et al*., 2008a].

The sediment accumulation rates (measured as MAR) for cores MV-41, MV-46 and MV-49 reflect temporal variations in regional depositional history. During LGM and Early Transgression, defined in this study as the time interval between 19-14 ky BP, MAR were between 81-428 g cm^{-2} ky^{-1} on the northern Pandora Trough depending on local geomorphology and proximity to fluvial sources [*Febo et al*., 2008]. Cores from this study have MAR values 258-485 g cm^{-2} ky^{-1} during Middle Transgression on the shelf edge and ~233 g cm^{-2} ky^{-1} toward the end of Middle Transgression on the upper slope which are comparable to MAR values of *Febo et al*. [2008]. Whereas the shelf edge shows an older depositional history and a very high MAR toward the end of Middle Transgression (also corresponding to the YD), upper slope depositional history reflects a younger sedimentary record formed at lower accumulation rates after YD when sea level rise resumed in the western Pacific [*Liu et al*., 2004; *Jorry et al*., 2008]. The high MAR on the shelf edge could be either due to mass flows, reworking, or may represent rapid new sedimentation. The continental shelf on the northern GoP is very narrow and steep (**Figure 4.1**) and consists of scalloped morphology suggesting that mass wasting may have been an important process [see *Francis et al*., 2008 for figures] when sea level was lower than present. Seismic profiles from PANASH cruise show some channels are partially filled with sediments [see *Francis et al*., 2008].

Decrease in MAR values above the 600 cm interval in core MV-46 correspond to the time interval when the sea-level reached highstand after post-glacial rise and terrigenous supply to the basin decreased. Core MV-46 yields an average MAR of ~23 g cm^{-2} ky^{-1} for the upper 100 cm (on a 1000-year time scale) compared to ^{210}Pb MAR of 140 g cm^{-2} ky^{-1} for the upper 20 cm (on a 100-year time scale) on multi core MV-47 from the same core location [*Muhammad et al*., 2008]. Similarly, core MV-41 yields an average MAR of ~5 g cm^{-2} ky^{-1} for the upper 60 cm (on a 1000-year time scale) compared to ^{210}Pb MAR of 200 g cm^{-2} ky^{-1} for the upper 20 cm (on a

100-year time scale) on multi core MV-42 from the same core location [*Muhammad et al*., 2008]. The difference between these sedimentation rates results from the shorter averaging timescale of ^{210}Pb geochronology, compared to ^{14}C geochronology [e.g. *Sadler*, 1981; *Alexander et al*., 1991].

4.5.4 Fluvial Supply and Geomorphology

Of the total 200 to 365 × 10^6 t y^{-1} of siliciclastic material (e.g., quartz, feldspars, clays) delivered to the shelf of the northern GoP [*Harris et al.*, 1993; *Milliman*, 1995; *Milliman et al.*, 1999], a small fraction (<15 × 10^6 t y^{-1}) is currently accumulating beyond the shelf edge [*Walsh and Nittrouer*, 2003; *Muhammad et al*., 2008]. Northern PNG rivers, such as Purari and Kikori are more close to the northeastern continental shelf and seem to have been supplying much more sediment to the northern Pandora Trough since post-LGM sea level rise than the western Fly River [*Slingerland et al*., 2008a]. The terrigenous input from northern rivers into the GoP basins has not remained the same since the LGM, as a result of climatically induced meltwater pulse events causing sea level rise and coastal retreat [*Jorry et al*., 2008].

4.5.5 Volcaniclastic Deposition

The geology of PNG is very complex and consists of predominantly folded sedimentary rocks in the western part and volcanogenic rocks in the central and eastern region (see *Febo et al*., [2008] and references therein). Pyroclastic sediments have been supplied episodically to the GoP shelf and slope since sea level lowstand [e.g. *Patterson*, 2006). Quaternary volcanics in the eastern PNG have volcanic ash that is distributed throughout the highlands [*Pain and Blong*, 1979]. Mineralogy of other cores from the upper slope of the Pandora Trough reveal presence of paramagnetic minerals (e.g., biotite, pumice, and glass shards) [*Febo et al*., 2008]. Although all the three cores in this study show high MS peaks, ash layers are only visible in core MV-49 on the middle slope. *Pain and Blong* [1979] have pointed that no tephras have been produced during

Holocene although some ashfall layers in the eastern New Guinea have been dated during ~7-15 ky BP [*Ruxton*, 1966]. It is possible that the ash layers observed in core MV-49 could from one of those eastern New Guinea ranges (**Figure 4.7**); however, further geochemical analyses of the ash layers are required before any correlation can be made between the ash layers and their source of origin.

4.5.6 Timing and Formation of the Northeastern GoP Shelf Edge

The sea level rise during warmer climatic conditions created the accommodation space on the northeastern GoP shelf edge resulting in sediment deposition (**Figure 4.3**). Age of the shelf edge deposits on the northeastern GoP shelf can be determined using AMS ^{14}C dates in core MV-41. The upper 12 m of sediment on the shelf edge has deposited in < 12 ky BP after post-LGM sea level rise. A rapid sea level rise prior to the YD drowned the shelf, creating the accommodation space for sediment deposition and also lessening the effects of waves reworking from the seabed. Most of this sediment on the shelf edge was deposited between the time of LGM and YD after a rapid sea level rise had slowed. After the rapid sediment accumulation period during YD, the northeastern shelf edge experienced a decrease in sediment accumulation as revealed by excess ^{210}Pb sedimentation rates [*Walsh and Nittrouer*, 2003; *Muhammad et al*., 2008]. *Walsh et al*., [2004] have reported extremely high accumulation rates of 3.8 g cm^{-2} y^{-1} in the central GoP clinoform at water depth of ~45 m on a 100-yr timescale. If our ages represent deposition and not reworking, these results are consistent with our MAR of 3900 g cm^{-2} ky^{-1} from the shelf edge suggesting that in addition to sea level as a major constraint on sediment accumulation, waves and tidal regimes at the same water depths may have been important during the Holocene for sediment transport alongshelf and across-shelf. However, water column data and seabed analyses show that minimal cross-shelf transport is taking place presently by nepheloid layers [*Walsh and Nittrouer*, 2003; *Muhammad et al*., 2008] on a 100-year timescale.

Fine particles from the major rivers such as Fly, are advected eastward by prevailing water currents which has also contributed to sediment deposition on the northern shelf edge [*Droxler et al*., 2004; *Keen et al*., 2006]. In addition to sediment load from major rivers, combined wave and tidal conditions since the Holocene may have also been responsible for the sediment deposition on the northeastern GoP shelf edge [*Wolanski and Alongi*, 1995; *Walsh et al*., 2004; *Slingerland et al*., 2008b]. The bedding observed in cores MV-41 and MV-46 may represent deposits produced by these processes (**Figure 4.7**). The seismic facies for the transect AA' that show parallel reflectors on the upper slope region in Figure 3.3 suggest either hemipelagic rain with different sedimentation rates or possible bottom-currents with contrasting velocity and density [e.g. *Sangree et al*., 1978]. The presence of poorly sorted coarse fraction in the basal portion of core MV-49 (**Figure 4.6**) suggests gravity flows may have been prevalent on the northern Pandora Trough either during LGM or YD when sea level rise slowed. During interglacial conditions such as MWP 1A and MWP 1B, water circulation in GoP may have played a major role alongwith other physical processes in transporting the suspended sediment in the water column beyond the shelf edge and upper slope to deeper seabed.

The morphology of the shelf in the northeastern GoP differs from the shelf in the in the western part of GoP in terms of available accommodation space, width of continental shelf and proximity to some of the major rivers. The shelf in the northeastern GoP is narrow with a steep slope gradient and close to major rivers such as Kikori and Purari rivers as compared to the shelf in the western GoP, allowing a higher terrigenous load to be delivered close to the shelf. Given the fact that the modern clinoform in the western GoP is undergoing rapid accretion in the foreset region, it is possible that same physical processes such as waves, tides and bottom boundary currents dispersing the sediments across and along the continental shelf now may have been

active in the northeastern GoP during the Holocene, with the same limitations on water depth and current energy near the bed.

4.6 Conclusions

Cores taken from the shelf edge and upper and middle slope in the northern Pandora Trough in GoP show that sediment mass accumulation rates have varied during post-LGM sea level rise. Climatic fluctuations during Late Pleistocene caused step-wise sea level rise resulting in periods of high and low sediment accumulation. Upper 12 m of the sediment on the northeastern shelf edge has deposited in < 12 ky BP after post-LGM sea level rise. The bulk of this mud deposit, with MAR values as high as 3900 g cm^{-2} ky^{-1}, is constrained between the time of LGM and YD. After the rapid sea level rise during MWP-1B, the continental shelf was starved of terrigenous input from PNG rivers, although sediments are still being deposited on the topset region at lower MAR values of 5-23 g cm^{-2} ky^{-1}. The findings from this study suggest that physical processes building the mud wedge on the northeastern GoP shelf were similar to the physical processes acting today building the clinoform in the western GoP shelf.

4.7 References

Alexander, C. R., C. A. Nittrouer, and D. J. DeMaster (1991), Sediment accumulation in a modern epicontinental shelf setting: the Yellow Sea, *Mar. Geol., 98*, 51-72.

Allison, M. A., M. T. Lee, A. S. Ogston, and R. C. Aller (2000), Origin of Amazon mudbanks along the northeastern coast of South America, *Mar. Geol., 163*, 241-256.

Andrews, J. C., and S. Clegg (1989), Coral sea circulation and transport deduced from modal information models, *Deep Sea Res., Part A, 36*, 957–974.

Beiersdorf, H. (1989), Provenance and accumulation rates of Pliocene and Quaternary sediments from the western Coral Sea, *Geol. Rundsch. Z. Allg. Geol., 78*, 987-998.

Bhattacharya, J. P., and R. G. Walker (1992), Deltas, in *Facies models-response to sea level change*, edited by R. G. Walker and N. P. James, Geological Association of Canada, pp. 157-177.

Brunskill, G. J., K. J. Woolfe, and I. Zagorskis (1995), Distribution of riverine sediment chemistry on the shelf, slope and rise of the Gulf of Papua, *Geo Mar. Lett.*, *15*, 160–165.

Brunskill, G. J. (2004), New Guinea and its coastal seas, a testable model of wet tropical coastal processes: An introduction to Project TROPICS, *Cont. Shelf Res.*, *24*, 2273–2295.

Burrage, D. M. (1993), Coral Sea Currents, *Corella*, *17*, 135-145.

Carter, J. M., and D. P. Johnson (1986), Sea-level controls on the post glacial development of the Great Barrier Reef, Queensland, *Mar. Geol.*, *71*, 137-164.

Cattaneo, A., F. Trincardi, A. Asioli, and A. Correggiari (2007), The Western Adriatic shelf clinoform: energy-limited bottomset, *Cont. Shelf Res.*, *27*, 506-525.

Chappell, J., and H. Polach (1991), Post-glacial sea-level rise from a coral record at Huon Peninsula, Papua New Guinea, *Nature*, *349*, 147-149.

Clark, P. U., A. Marshall, A. McCabe, A. C. Mix, and A. J. Weaver (2004), Rapid rise of sea level 19000 years ago and its global implications, *Science*, *304*, 1141–1144.

Crockett, J. S., C. A. Nittrouer, A. S. Ogston, D. F. Naar, and B. T. Donahue (2008), Morphology and filling of incised submarine valleys on the continental shelf near the mouth of the Fly River, Gulf of Papua, *J. Geophys. Res.*, *113*, F01S12, doi:10.1029/2006JF000674.

Damon, P. E., J. C. Lerman, and A. Long (1978), Temporal fluctuations of atmospheric ^{14}C: Causal factors and implications, *Annu. Rev. Earth Planet. Sci.*, *6*, 457-494.

Daniell, J. J. (2008), Development of a bathymetric grid for the Gulf of Papua and adjacent areas: A note describing its development, *J. Geophys. Res.*, *113*, F01S15, doi:10.1029/2006JF000673.

Davies, H. L. and I. E. Smith (1971), Geology of Eastern Papua, *Geol. Soc. Am. Bull.*, *82*, 3299-3312.

Davies, P. J., P. A. Symonds, D. A. Feary, and C. J. Pigram (1989), The evolution of the carbonate platforms of northeast Australia, in *Controls on Carbonate Platform and Basin Development*, edited by P. D. Crevello, Spec. Publ. SEPM Soc. Sediment. Geol., 44, 233–258.

Droxler, A. W., G. R. Dickens, S. J. Bentley, L. C. Peterson, and B. N. Opdyke (2004), Neogene evolution of the mixed carbonate/siliciclastic margin of the Gulf of Papua: Preliminary results of spring 2004 PANASH Cruise on the R/V *Melville*, *Eos Trans. AGU*, *86* (52), Fall Meet. Suppl., Abstract OS44A-08.

Fairbanks, R. G. (1989), A 17,000 year glacio-eustatic sea level record; influence of glacial melting rates on the Younger Dryas event and deep ocean circulation, *Nature*, *342*, 637–642.

Fairbanks, R. G., R. A. Mortlock, T. C. Chiu, L. Cao, A. Kaplan, T. P. Guilderson, T. W. Fairbanks, A. L. Bloom, P. M. Grootes, and M. J. Nadeau (2005), Radiocarbon calibration curve spanning 0 to 50000 years BP based on paired $^{230}Th/^{234}U/^{238}U$ and ^{14}C dates on pristine corals, *Quat. Sci. Rev.*, *24*, 1781–1796.

Febo, L. A., S. J. Bentley, J. H. Wrenn, A. W. Droxler, G. R. Dickens, L. C. Peterson, and B. N. Opdyke (2008), Late Pleistocene and Holocene sedimentation, organic-carbon delivery, and paleoclimatic inferences on the continental slope of the northern Pandora Trough, Gulf of Papua, *J. Geophys. Res.*, *113*, F01S18, doi:10.1029/2006JF000677.

Francis, J. M., J. J. Daniell, A. W. Droxler, G. R. Dickens, S. J. Bentley, L. C. Peterson, B. Opdyke, and L. Beaufort (2008), Deep-water geomorphology and sediment pathways of the mixed siliciclastic-carbonate system, Gulf of Papua, *J. Geophys. Res.*, *113*, doi:10.1029/2007JF000851.

Gardner, J. V. (1970), Submarine geology of the western Coral Sea, *Geol. Soc. Am. Bull.*, *81*, 2599-2614.

GEOTEK (2003), GeoScan Digital Imaging System Manual.

Guilderson, T. P., R. G. Fairbanks and J. L. Rubenstone (2001), Tropical Atlantic coral oxygen isotopes: glacial-interglacial sea surface temperatures and climate change, *Mar. Geol.*, *172*, 75-89.

Hanebuth, T., K. Stattegger and P. M. Grootes (2000), Rapid flooding of the Sunda Shelf-a late-glacial sea-level record, *Science*, *288*, 1033–1035.

Harris, P. T., E. K. Baker, A. R. Cole, and S. A. Short (1993), A preliminary study of sedimentation in the tidally dominated Fly River delta, Gulf of Papua, *Cont. Shelf Res.*, *13*, 441–472.

Harris, P. T., C. B. Pattiaratchi, J. B. Keene, R. W. Dalrymple, J. V. Gardner, E. K. Baker, A. R. Cole, D. Mitchell, P. Gibbs, and W. W. Schroeder (1996), Late Quaternary deltaic and carbonate sedimentation in the Gulf of Papua foreland basin: Response to sea-level change, *J. Sediment. Res.*, *66*, 801–819.

Jorry, S. J., A. W. Droxler, G. Mallarino, G. R. Dickens, S. J. Bentley, L. Beaufort, L. C. Peterson, and B. N. Opdyke (2008), Bundled turbidite deposition in the central Pandora Trough (Gulf of Papua) since Last Glacial Maximum: Linking sediment nature and accumulation to sea level fluctuations at millennial timescale, *J. Geophys. Res.*, *113*, doi:10.1029/2006JF000649.

Keen, T. R., D. S. Ko, R. L. Slingerland, S. Riedlinger, and P. Flynn (2006), Potential transport pathways of terrigenous material in the Gulf of Papua, *Geophys. Res. Lett.*, *33*, L04608, doi:10.1029/2005GL025416.

Kuehl, S. A., B. M. Levy, W. S. Moore, M. A. Allison (1997), Subaqueous delta of the Ganges-Brahmaputra river system, *Mar. Geol., 144*, 81-96.

Lambeck, K., and J. Chappell (2001), Sea level change through the last glacial cycle, *Science, 292*, 679–686.

Liu, J. P., J. D. Milliman, S. Gao, and P. Cheng (2004), Holocene development of the Yellow River's subaqueous delta, North Yellow Sea, *Mar. Geol., 209*, 45-67.

Milliman, J. D. (1995), Sediment discharge to the ocean from small mountainous rivers: The New Guinea example, *Geo. Mar. Lett., 15*, 127–133.

Milliman, J. D., K. L. Farnsworth, C. S. Albertin (1999), Flux and fate of fluvial sediments leaving large islands in the East Indies, *Neth. J. Sea Res., 41*, 97-107.

Mitchum, R. M., P. R. Vail, and J. B. Sangree (1977), Seismic stratigraphy and global changes of sea level: Part 6, Stratigraphic interpretation of seismic reflection patterns in depositional sequences, in *Seismic Stratigraphy: Applications to Hydrocarbon Exploration*, edited by C. E. Payton, pp. 135–143, Am. Assoc. of Pet. Geol., Tulsa, Okla.

Muhammad, Z., S. J. Bentley, L. A. Febo, A. W. Droxler, G. R. Dickens, L. C. Peterson, and B. N. Opdyke (2008), Excess ^{210}Pb inventories and fluxes along the continental slope and basins of the Gulf of Papua, *J. Geophys. Res., 113*, F01S17, doi:10.1029/2006JF000676.

Nittrouer, C. A., S. A. Kuehl, D. J. DeMaster, and R. O. Kowsmann (1986), The deltaic nature of Amazon shelf sedimentation, *Geol. Soc. Am. Bull., 97*, 444–458.

Nittrouer, C. A., and L. D. Wright (1994), Transport of Particles Across Continental Shelves, *Rev. Geophys., 32*(1), 85–113.

Ota, Y., J. Chappell, R. Kelley, N. Yonekura, E. Matsumoto, T. Nishimura, and J. Head, (1993), Holocene coral reef terraces and coseismic uplift of Huon Peninsula, Papua New Guinea, *Quat. Res., 40*, 177-188.

Pain, C. F. and R. J. Blong (1979), The distribution of tephras in the Papua New Guinea Highlands, *Search, 10*, 228-230.

Patterson, L. J. (2006), Petrological and geochemical investigations of deep sea turbidite sands in the Pandora and Moresby Troughs: Source to sink Papua New Guinea focus area, M. S. thesis, Louisiana State University.

Pickup, G., and R. F. Warner (1984), Geomorphology of tropical rivers: I. Channel adjustment to sediment load and discharge in the Fly and lower Purari, Papua New Guinea, in *Channel Processes—Water, Sediment, Catchment Controls*, edited by A. P. Schick, *Catena Suppl., 5*, 18-41.

Posamentier, H. W., and P. R. Vail (1988), *Eustatic controls on clastic deposition. II. Sequence and systems tract models* in *Sea Level Changes-An Integrated Approach*, edited by C. K. Wilgus, B. S. Hastings, C. G. St, C. Kendall, H. W. Posamentier, C. A. Ross, and J. C. Van Wagoner, Spec. Publ. SEPM Soc. Sediment. Geol., 42, 125-154.

Roberts, H. H., R. H. Fillon, B. Kohl, J. M. Robalin and J. C. Sydow (2004), Depositional architecture of the Lagniappe delta: sediment characteristics, timing of depositional events, and temporal relationship with adjacent shelf-edge deltas: in *Late Quaternary stratigraphic evolution of the northern Gulf of Mexico margin*, edited by J. B. Anderson and R. H. Fillon, Spec. Publ. SEPM Soc. Sediment. Geol., 79, 143-188.

Ruxton, B. P. (1966), Correlation and stratigraphy of dacitic ash-fall layers in northeastern Papua, *J. Geol. Soc. Aus*., *13*, 41-67.

Sadler, P. M. (1981), Sediment accumulation rates and the completeness of stratigraphic sections, *J. Geol*., *89*, 569–584.

Sangree, J. B., D. C. Waylett, D. E. Frazier, G. B. Amery, and W. J. Fennessy (1978), Recognition of continental slope seismic facies, offshore Texas-Louisiana in *Framework, facies, and oil-trapping characteristics of the upper continental margin*, edited by A. H. Bouma, G. T. Moore, and J. M. Coleman, *AAPG Studies in Geol*., 7, 87-116.

Sarg, J. F., L. J. Weber, J. R. Markello, J. K. Southwell, J. M. Thomson, J. J. Kmeck, M. E. Christal, and Y. Tanaka (1996), Carbonate sequence stratigraphy—A summary and perspective with case history, Neogene, Papua New Guinea, in *Proceedings of the International Symposium on Sequence Stratigraphy in SE Asia*, pp. 137–179, Indonesian Pet. Assoc., Jakarta.

Slingerland, R., N. W. Driscoll, J. D. Milliman, S. R. Miller, and E. A. Johnstone (2008a), Anatomy and growth of a Holocene clinothem in the Gulf of Papua, *J. Geophys. Res.*, *113*, F01S13, doi:10.1029/2006JF000628.

Slingerland, R., R. W. Selover, A. S. Ogston, T. R. Keen, N. W. Driscoll, and J. D. Milliman (2008b), Building the Holocene clinothem in the Gulf of Papua: An ocean circulation study, *J. Geophys. Res.*, *113*, F01S14, doi:10.1029/2006JF000680.

Tcherepanov, E., A. W. Droxler, P. Lappointe, G. R. Dickens, S. J. Bentley, L. Beaufort, L. C. Peterson, J. J. Daniell, and B. Opdyke (2008), Neogene evolution of the mixed carbonate-siliciclastic system in the Gulf of Papua, Papua New Guinea, *J. Geophys. Res.*, *113*, F01S21, doi:10.1029/2006JF000684.

Thom, B. G., and P. S. Roy (1983), Sea-level change in New South Wales over the past 15,000 years: in *Australian Sea Levels in the Past 15,000 Years: A Review*, edited by D. Hopley, Townsville, Australia, James Cook University, Department of Geography, pp. 64-84.

Thom, B. G., and L. D. Wright (1983), Geomorphology of the Purari Delta, in *The Purari: Tropical Environment of a High Rainfall River Basin*, edited by T. Petr, pp. 47-65, Dr. W. Junk, The Hague.

Visser, K., R. C. Thunell, and L. Stott (2003), Magnitude and timing of temperature change in the Indo-Pacific warm pool during deglaciation, *Nature, 421*, 152–155.

Walsh, J. P., and C. A. Nittrouer (2003), Contrasting styles of off-shelf sediment accumulation in New Guinea, *Mar. Geol., 196*, 105–125.

Walsh, J. P., C. A. Nittrouer, C. M. Palinkas, A. S. Ogston, R. W. Sternberg, and G. J. Brunskill (2004), Clinoform mechanics in the Gulf of Papua, New Guinea, *Cont. Shelf Res., 24*, 2487–2510.

Weber, M. E., F. Niessen, G. Kuhn, and M. Wiedicke (1997), Calibration and application of marine sedimentary physical properties using a multi-sensor core logger, *Mar. Geol., 136*, 151–172.

Weaver, A. J., O. A. Saenko, P. U. Clark, and J. X. Mitrovica (2003), Meltwater pulse 1A from Antarctica as a trigger of the Bølling-Allerød warm interval, *Science, 299*, 1709-1713.

Winterer, E. L. (1970), Submarine valley systems around Coral-Sea basin (Australia), *Mar. Geol., 8*, 229–244.

Wolanski, E., and M. Eagle (1991), Oceanography and fine sediment transport, Fly River estuary and Gulf of Papua, Publ. 21, pp. 453–457, Water Qual. Cent., Natl. Agric. Libr., Beltsville, Md.

Wolanski, E., and D. M. Alongi (1995), A hypothesis for the formation of a mud bank in the Gulf of Papua, *Geo Mar. Lett., 15*(3–4), 166–171.

Wolanski, E., A. Norro, and B. King (1995), Water circulation in the Gulf of Papua, *Cont. Shelf Res., 15*, 185–212.

Wright, L. D., and J. M. Coleman (1973), Variations in morphology of major river deltas as function of ocean wave and river discharge regimes, *AAPG Bull., 57*, 370-398.

Yokoyama, Y., K. Lambeck, P. De Deckker, P. Johnston, and K. Fifield (2000), Timing of the Last Glacial Maximum from observed sea-level minima, *Nature, 406*, 713–716.

CHAPTER 5
SUMMARY AND CONCLUSIONS

This study has examined sediment flux to the shelf and slope of the Gulf of Papua on century and millennium timescales. Analyses of sediment cores have given an insight into the patterns of sedimentation dynamics in the study region.

Sediment accumulation (0.05–0.35 cm y^{-1}; 0.05–0.28 g cm^{-2} y^{-1}) measured from excess ^{210}Pb and inventory-derived ^{210}Pb fluxes (1–12.8 dpm cm^{-2} y^{-1}) display regional variations, decreasing seaward, and along isobaths away from the northeastern shelf edge. This study estimates a terrigenous sediment load of approximately 7–14 × 10^6 t, being discharged annually from the shelf and accumulating in the northern Pandora Trough, which is consistent with previous findings. The existence of possible turbidity current transport and deposition have been documented in a core taken from Moresby Trough, where water depths exceed 2000 m. Estimated excess ^{210}Pb fluxes at the shelf edge and upper slope are highest, consistent with the combined effects of sediment focusing and boundary scavenging of oceanic water masses.

Bioturbation and sediment accumulation rates estimated from model results show that D_b and S in GoP shelf and slope vary by an order of magnitude. Using a two-layer particle mixing numerical model, Model D_{b1} (biodiffusion coefficient in the upper layer) values are in the range of 0.007-60 cm^2 y^{-1} and D_{b2} (biodiffusion coefficient in the lower layer) values are in the range of 0.002-2.9 cm^2 y^{-1}. Model S values range from 0.04-0.32 cm y^{-1}. For the cores locates on the upper slope and middle slope in the Pandora Trough, biodiffusion coefficients and mixing depths exhibit a decreasing trend with increasing water depth consistent with similar observations in other studies.

Modeled bioturbation rates on selected cores in Gulf of Papua shelf and slope region vary by an order of magnitude. A two-layer model is used where sediment mixing by bioturbation is

faster in the upper layer. Modeled bioturbation rates in the upper layer are in the range of 0.02-60 $cm^2\ y^{-1}$ while in the lower layer, bioturbation rates are in the range of 0.009-3 $cm^2\ y^{-1}$. Modeled sediment accumulation rates for these cores, which are similar in the upper and lower layer, are in the range of 0.04-0.31 cm y^{-1}. From this model, depth of the upper mixed layer (L_1) varies between 2 and 10 cm while the depth of lower mixed layer (L_2) varies between 7 and 31 cm. For the cores locates on the upper slope and middle slope in the Pandora Trough, bioturbation coefficients rates exhibit a decreasing trend with increasing water depth consistent with similar observations in other continental margin studies.

Sediment cores taken from the shelf edge and upper and middle slope in the northern Pandora Trough in Gulf of Papua show that sediment mass accumulation rates have not remained the same since post-LGM sea level rise. Climatic fluctuations during Late Pleistocene caused step-wise sea level rise resulting in periods of high and low sediment accumulation. Upper 12 m of the sediment on the northeastern shelf edge has deposited in less than 12 ky BP after post-LGM sea level rise. The bulk of this mud deposit, with sediment mass accumulation rates exceeding 3900 g $cm^{-2}\ ky^{-1}$, is constrained between the time of LGM and Younger Dryas. After the rapid sea level rise during MWP-1B, the continental shelf was starved of terrigenous input from Papua New Guinea rivers, although sediments were still being deposited on the shelf region at lower sediment mass accumulation rates of 5-23 g $cm^{-2}\ ky^{-1}$. The findings from this study suggest that physical processes building the mud wedge on the northeastern Gulf of Papua shelf were similar to the physical processes acting today building the clinoform in the western Gulf of Papua shelf.

APPENDIX A: MATLAB CODE

```
% MULTILAYER NUMERICAL MODEL.
% This multilayer model consists of 2 layers solved by finite difference
% technique.
% A = excess Pb-210 activity (dpm/g)
% D = biodiffusion coefficient (cm^2/y)
% S = sediment accumulation rate (cm/y)
% lambda = Pb-210 decay constant (per yr)
% x = depth (cm)
% Declare variables
real A1(150):A2(150);
% A1 = model excess Pb-210 activity in layer 0-L1.
% A2 = model excess Pb-210 activity in layer L1-L2.
real a(150):b(150):c(150):d(150);
% a,b,c, and d are discretization coefficients
real p(150):q(150);
% p and q are tri-diagonal matrix coefficients
% Declare D1,D2, S, and lambda
% D1 = biodiffusion coefficient, 0-L1 cm (upper layer).
% D2 = biodiffusion coefficient, L1-L2 cm (lower layer).
% S = sediment accumulation rate, cm/yr.
real D1:D2:S:lambda;
% Declare depth
real xl1:xl2;
% xl1 = depth of upper layer
% xl2 = depth of lower layer
real x1(150):x2(150);
real dx1:dx2;
% Declare values for parameters
% maximum number of iterations
% integer itermax;
%
% Declare itermax (maximun number of iterations)
itermax=100;
% Declare D (biodiffusion coefficient, cm^2/y) and S (sed. acc.rate, cm/yr)
% for all layers.
D1=’enter input parameter’
D2=’enter input parameter’
S=’enter input parameter’
lambda=0.031;
%
%Make grids in all layers
n1=80; % no. of points in layer 0-L1.
n2=80; % no. of points in layer L1-L2.
%
```

```
    %
================================================================================
    % Define grid in all 2 layers.
    %
    % Grid in layer 1
    xl1=5.0 % depth of first layer, 0-L1
    % set x values for each point in layer 0-L1
    dx1=xl1/(n1-1);
    for i=1:n1
       x1(i)=(i-1)*dx1;
    end
    %
    % Grid in layer 2
    xl2=3.*23.0; % depth of second layer, L1-L2
    % set x values for each point in layer L1-L2
    dx2=xl2/(n2-1);
    for i=1:n2
       x2(i)=xl1+(i-1)*dx2;
    end
    %
    %
================================================================================
    % Specify initial/boundary conditions in all layers.
    % Specify all values of A1,and A2.
    for i=1:n1
       A1(i)=1.0;
    end
    for i=1:n2
       A2(i)=1.0;
    end
    %
    % Start solving equations iteratively
    %
    for it=1:itermax
    %
    % solve first equation for layer 0-L1
    %
    % specify boundary conditions for layer 0-L1
    %
    n = n1;
    A1(1)=12.6; % upper boundary at the seabed
    A1(n)=(D2/D1)*(A2(2)-A2(1))*(dx1/dx2)+A1(n-1); % lower boundary-interface
    % between 0-L1 and L1-L2.
    %
    % build coeffiecients
    %
    for i=1:n
```

```
a(i)=S/dx1+2.*D1/dx1/dx1+lambda;
b(i)=D1/dx1/dx1;
c(i)=S/dx1+1.*D1/dx1/dx1;
d(i)=0.0;
end
% solve using Tri-Diogonal Matrix Analysis (TDMA)
%
a(1)=1.;
a(n)=1.;
b(1)=0.;
b(n)=0.;
c(1)=0.;
c(n)=0.;
d(1)=A1(1);
d(n)=A1(n);
p(1)=b(1)/a(1);
q(1)=d(1)/a(1);
% p and q are TDMA coefficients.
for i = 2:n
   p(i) = b(i)/(a(i)-c(i)*p(i-1));
   q(i) = (d(i)+c(i)*q(i-1))/(a(i)-c(i)*p(i-1));
end
A1(n) = q(n);
for i = 1:n-1
   i1 = n-i;
   A1(i1) = p(i1)*A1(i1+1)+q(i1);
end
%
% solved equation for layer 0-L1.
%
```
==========

```
% Solve second equation for layer L1-L2
%
% Specify boundary conditions for layer L1-L2
%
n = n2;
A2(1)=A1(n1); % upper boundary-interface between layer 0-L1 and L1-L2
A2(n)=A2(n-1); % lower boundary-interface at L1-L2 with backward diff.
%
% build Tri-Diogonal Matrix Analysis (TDMA) coeffiecients
%
for i=1:n
a(i)=S/dx2+2.*D2/dx2/dx2+lambda;
b(i)=D2/dx2/dx2;
c(i)=S/dx2+1.*D2/dx2/dx2;
d(i)=0.0;
end
```

```
% solve using TDMA
a(1)=1.;
a(n)=1.;
b(1)=0.;
b(n)=0.;
c(1)=0.;
c(n)=0.;
d(1)=A2(1);
d(n)=A2(n);
p(1)=b(1)/a(1);
q(1)=d(1)/a(1);
for i = 2:n
   p(i) = b(i)/(a(i)-c(i)*p(i-1));
   q(i) = (d(i)+c(i)*q(i-1))/(a(i)-c(i)*p(i-1));
end
A2(n) = q(n);
for i = 1:n-1
   i1 = n-i;
   A2(i1) = p(i1)*A2(i1+1)+q(i1);
end
% solved equation 2
end
% Plot the curves
semilogx(A1,x1,'k--',A2,x2,'k--')
hold on
K = xlsread(‘add path here’); % depth-y-axis
L = xlsread(‘add path here’); % Pb-210-x-axis
semilogx(L,K,'ko')
axis([1,200,0,30])
set(gca,'YDir','reverse')
xl=xlabel('MV-43','FontWeight','bold');
set(xl,'FontSize',10)
set(xl,'FontWeight','bold')
yl=ylabel('Depth (cm)');
set(yl,'FontWeight','bold')
set(yl,'FontSize',10)
set(gca,'FontWeight','bold')
% interpolate data by using spline
A1=A1(1:40);
A2=A2(2:40);
x1=x1(1:40);
x2=x2(2:40);
A=[A1 A2];
x=[x1 x2];
y=interp1(x,A,K,'spline');
set(gca,'YDir','reverse')
% calculation of goodness of fit (R^2)
```

```
Lm=0.; % Lm = number of data points
for i=1:18
   Lm=Lm+L(i);
end
Lm=Lm/18.;
sum1=0.;
for i= 1:18
   sum1=sum1+(L(i)-y(i))*(L(i)-y(i));
end
sum2=0.;
for i= 1:18
   sum2=sum2+(L(i)-Lm)*(L(i)-Lm);
end
R2=1-sum1/sum2
```

APPENDIX B: ^{210}Pb DATA

Core MV-10

Depth interval (cm)	Excess ^{210}Pb activity (dpm g^{-1})	Supported ^{210}Pb activity (dpm g^{-1})	Excess ^{210}Pb inventory (dpm cm^{-2})
0-1	20.24±0.54	0.57±0.02	19.97±0.53
1-2	11.38±0.42	0.54±0.02	10.55±0.39
2-3	5.27±0.34	0.62±0.04	4.92±0.32
3-4	2.03±0.24	0.69±0.06	2.13±0.26
4-5	2.84±0.27	0.55±0.05	2.81±0.27
5-6	2.26±0.24	0.62±0.05	2.43±0.26

Core MV-12

Depth interval (cm)	Excess ^{210}Pb activity (dpm g^{-1})	Supported ^{210}Pb activity (dpm g^{-1})	Excess ^{210}Pb inventory (dpm cm^{-2})
0-2	11.28±0.39	0.56±0.02	24.71±0.84
2-3	7.78±0.34	0.49±0.02	8.54±0.37
3-4	5.42±0.29	0.50±0.03	6.00±0.32
4-5	3.89±0.27	0.55±0.03	3.93±0.27
5-6	2.66±0.26	0.52±0.04	3.12±0.31
6-8	1.73±0.23	0.40±0.04	3.56±0.47

Core MV-14

Depth interval (cm)	Excess ^{210}Pb activity (dpm g^{-1})	Supported ^{210}Pb activity (dpm g^{-1})	Excess ^{210}Pb inventory (dpm cm^{-2})
0-1	31.91±0.77	1.27±0.03	19.78±0.48
1-2	13.47±0.46	0.90±0.03	9.52±0.33
2-3	9.21±0.42	1.02±0.04	7.96±0.37
3-4	6.18±0.39	1.19±0.06	4.71±0.30
4-5	7.62±0.36	0.99±0.04	6.54±0.31
5-6	7.35±0.38	1.09±0.05	5.91±0.30
6-8	4.28±0.32	1.17±0.07	7.07±0.52
8-10	3.03±0.27	1.09±0.07	5.11±0.46

Core MV-16

Depth interval (cm)	Excess ^{210}Pb activity (dpm g^{-1})	Supported ^{210}Pb activity (dpm g^{-1})	Excess ^{210}Pb inventory (dpm cm^{-2})
0-1	27.62±0.64	1.33±0.03	28.65±0.67
1-2	17.15±0.50	1.35±0.04	18.09±0.53
2-3	8.05±0.36	1.49±0.06	8.28±0.38
3-4	3.49±0.27	1.28±0.08	3.58±0.28
4-5	4.08±0.29	1.19±0.07	4.14±0.29
5-6	1.08±0.14	1.26±0.07	1.21±0.15
6-8	1.95±0.22	0.87±0.07	3.85±0.44

Core MV-18

Depth interval (cm)	Excess ^{210}Pb activity (dpm g^{-1})	Supported ^{210}Pb activity (dpm g^{-1})	Excess ^{210}Pb inventory (dpm cm^{-2})
0-4	27.92±0.61	1.02±0.02	102.58±0.56
4-5	24.70±0.61	0.89±0.02	33.24±0.82
5-6	30.42±0.74	0.86±0.02	30.19±0.73
6-8	25.54±0.63	0.99±0.02	43.12±1.07
8-10	25.62±0.63	0.94±0.02	32.64±0.81
10-12	30.76±0.70	0.99±0.02	42.55±0.96
12-14	22.99±0.59	1.01±0.03	31.90±0.82
14-16	20.46±0.59	1.15±0.03	27.43±0.79
16-18	17.22±0.56	1.12±0.04	23.39±0.76
18-20	13.66±0.49	0.87±0.03	19.54±0.71
20-22	7.11±0.35	0.94±0.04	10.93±0.54
22-24	7.14±0.43	0.93±0.05	10.93±0.66
24-26	3.04±0.25	0.86±0.06	4.97±0.42

Core MV-19

Depth interval (cm)	Excess ^{210}Pb activity (dpm g^{-1})	Supported ^{210}Pb activity (dpm g^{-1})	Excess ^{210}Pb inventory (dpm cm^{-2})
2-3	13.98±0.37	0.87±0.02	16.00±0.43
3-4	14.23±0.37	0.93±0.02	16.78±0.44
4-5	12.07±0.36	0.89±0.03	13.72±0.41
5-6	10.14±0.36	0.78±0.03	12.27±0.43
6-8	7.79±0.31	0.87±0.03	17.14±0.68
8-12	6.58±0.31	0.84±0.04	28.84±1.35
12-14	2.58±0.20	0.76±0.05	5.84±0.45
14-16	1.01±0.15	0.79±0.07	2.47±0.37

Core MV-20

Depth interval (cm)	Excess ^{210}Pb activity (dpm g^{-1})	Supported ^{210}Pb activity (dpm g^{-1})	Excess ^{210}Pb inventory (dpm cm^{-2})
0-1	31.15±0.69	0.82±0.02	28.27±0.62
1-2	15.59±0.53	0.88±0.03	14.25±0.49
2-3	10.72±0.49	0.75±0.03	9.47±0.43
3-4	8.40±0.41	0.56±0.03	7.53±0.36
4-5	10.79±0.49	0.89±0.04	9.54±0.43
5-6	5.09±0.35	0.94±0.06	4.25±0.29
6-8	1.56±0.24	0.90±0.09	2.67±0.42
8-10	0.84±0.21	0.62±0.09	1.35±0.34
10-12	1.32±0.19	0.87±0.08	2.17±0.31

Core MV-21

Depth interval (cm)	Excess ^{210}Pb activity (dpm g^{-1})	Supported ^{210}Pb activity (dpm g^{-1})	Excess ^{210}Pb inventory (dpm cm^{-2})
0-1	25.99±0.62	1.79±0.04	21.26±0.50
1-2	16.24±0.55	2.04±0.07	13.65±0.47
2-3	15.67±0.52	2.17±0.07	12.51±0.42
3-4	16.42±0.55	2.08±0.06	12.88±0.43
4-5	16.37±0.51	2.46±0.07	12.54±0.39
5-6	9.97±0.42	1.50±0.06	7.76±0.33
6-8	1.40±0.16	1.57±0.09	2.15±0.25

Core MV-24

Depth interval (cm)	Excess ^{210}Pb activity (dpm g^{-1})	Supported ^{210}Pb activity (dpm g^{-1})	Excess ^{210}Pb inventory (dpm cm^{-2})
0-1	39.44±0.92	2.10±0.02	18.29±0.43
1-2	24.53±0.72	2.43±0.03	9.93±0.29
2-3	16.77±0.62	2.22±0.03	7.27±0.27
3-4	14.89±0.57	2.47±0.04	6.66±0.25
4-5	11.67±0.54	2.12±0.04	5.29±0.25
5-6	11.84±0.49	2.50±0.04	5.84±0.24
6-8	10.07±0.45	2.26±0.05	4.65±0.21
8-10	1.91±0.17	2.66±0.04	1.01±0.09
10-12	2.06±0.19	2.12±0.06	0.91±0.09
12-14	1.49±0.17	2.24±0.03	0.84±0.09

Core MV-26

Depth interval (cm)	Excess ^{210}Pb activity (dpm g^{-1})	Supported ^{210}Pb activity (dpm g^{-1})	Excess ^{210}Pb inventory (dpm cm^{-2})
0-1	39.59±1.09	3.89±0.09	10.63±0.29
1-2	24.75±0.74	3.73±0.09	10.59±0.32
2-3	20.90±0.68	3.20±0.09	8.96±0.29
3-4	15.81±0.48	3.04±0.08	7.22±0.22
4-5	16.09±0.54	3.36±0.09	6.84±0.23
5-6	12.78±0.45	3.99±0.11	5.41±0.19
6-8	3.79±0.30	4.71±0.17	6.22±0.49
8-10	1.44±0.13	6.22±0.10	2.29±0.20
10-12	4.99±0.19	2.95±0.15	7.50±0.59
12-14	1.19±0.39	2.34±0.12	1.86±0.29
14-16	1.45±0.19	2.41±0.12	2.25±0.31
18-20	1.16±0.15	2.77±0.11	1.72±0.23
20-22	1.26±0.16	2.95±0.12	1.81±0.23
22-24	1.62±0.19	2.99±0.12	2.38±0.28

Core MV-28

Depth interval (cm)	Excess ^{210}Pb activity (dpm g^{-1})	Supported ^{210}Pb activity (dpm g^{-1})	Excess ^{210}Pb inventory (dpm cm^{-2})
0-1	53.49±0.89	5.00±0.08	21.45±0.36
1-2	27.52±0.63	4.12±0.08	12.55±0.29
2-3	32.44±0.69	4.32±0.08	15.11±0.32
3-4	23.83±0.67	4.54±0.11	12.02±0.34
4-5	14.61±0.42	6.29±0.13	7.17±0.21
5-6	15.84±0.45	5.14±0.11	8.09±0.23
8-10	4.16±0.19	5.27±0.11	4.63±0.22
10-12	2.43±0.19	2.84±0.11	2.59±0.21
12-14	1.09±0.11	2.72±0.08	1.10±0.11

Core MV-30

Depth interval (cm)	Excess ^{210}Pb activity (dpm g^{-1})	Supported ^{210}Pb activity (dpm g^{-1})	Excess ^{210}Pb inventory (dpm cm^{-2})
0-1	106.31±2.01	3.88±0.09	24.50±0.47
1-2	30.86±0.78	3.81±0.09	13.09±0.33
2-3	16.93±0.63	4.04±0.09	7.54±0.28
3-4	15.99±0.51	4.00±0.08	7.74±0.25
4-5	14.67±0.51	3.29±0.09	7.77±0.27
5-6	19.75±0.59	3.10±0.11	9.83±0.29
6-8	4.28±0.25	3.86±0.17	9.57±0.57
10-12	2.31±0.14	5.67±0.15	2.66±0.17
12-14	2.42±0.16	3.99±0.12	2.87±0.19
14-16	1.16±0.11	3.19±0.12	1.29±0.12

Core MV-32

Depth interval (cm)	Excess ^{210}Pb activity (dpm g^{-1})	Supported ^{210}Pb activity (dpm g^{-1})	Excess ^{210}Pb inventory (dpm cm^{-2})
0-2	56.28±0.96	3.27±0.05	49.42±0.85
2-4	16.84±0.57	3.06±0.09	16.11±0.55
4-6	3.25±0.26	3.33±0.13	3.87±0.31
6-8	3.48±0.25	3.49±0.13	4.33±0.31

Core MV-38

Depth interval (cm)	Excess ^{210}Pb activity (dpm g^{-1})	Supported ^{210}Pb activity (dpm g^{-1})	Excess ^{210}Pb inventory (dpm cm^{-2})
0-1	46.86±1.11	4.30±0.09	14.03±0.33
1-2	30.96±0.72	3.57±0.08	12.72±0.29
2-3	21.53±0.64	3.56±0.09	9.60±0.29
3-4	18.84±0.57	4.39±0.11	8.81±0.27
4-5	18.69±0.58	4.89±0.12	8.50±0.27
5-6	10.92±0.44	3.16±0.10	5.13±0.21
6-8	4.69±0.28	2.99±0.11	5.22±0.31
8-10	4.21±0.28	2.47±0.11	9.51±0.63
10-12	1.54±0.15	2.56±0.09	1.72±0.17
12-14	2.59±0.20	3.05±0.11	2.82±0.22

Core MV-39

Depth interval (cm)	Excess ^{210}Pb activity (dpm g^{-1})	Supported ^{210}Pb activity (dpm g^{-1})	Excess ^{210}Pb inventory (dpm cm^{-2})
0-2	42.45±0.73	1.67±0.03	45.18±0.78
2-3	33.49±0.64	1.34±0.03	16.65±0.32
3-5	27.38±0.63	1.85±0.04	28.85±0.66
5-6	15.16±0.47	1.46±0.04	8.43±0.26
6-8	12.55±0.47	1.42±0.05	14.93±0.56
8-10	6.28±0.37	1.54±0.08	8.08±0.47
10-12	7.66±0.39	1.52±0.07	9.43±0.49
16-18	1.76±0.21	1.40±0.09	2.17±0.26
18-20	1.65±0.20	1.37±0.09	2.14±0.26

Core MV-42

Depth interval (cm)	Excess ^{210}Pb activity (dpm g^{-1})	Supported ^{210}Pb activity (dpm g^{-1})	Excess ^{210}Pb inventory (dpm cm^{-2})
0-1	18.21±0.78	1.72±0.07	8.30±0.36
1-2	11.82±0.52	1.54±0.06	5.12±0.23
2-3	11.51±0.55	1.42±0.06	5.14±0.24
3-4	9.01±0.43	1.41±0.05	4.78±0.23
4-5	9.17±0.52	1.29±0.07	4.11±0.24
5-6	7.46±0.36	1.29±0.06	4.35±0.21
6-8	7.29±0.38	1.34±0.08	16.76±0.87
8-10	4.39±0.34	1.46±0.07	4.70±0.36
10-12	4.33±0.32	1.29±0.04	5.37±0.39
12-14	16.68±0.57	1.24±0.09	19.57±0.6
14-16	3.73±0.33	1.48±0.09	4.00±0.36
16-18	2.15±0.26	1.10±0.10	2.53±0.30
18-20	1.75±0.23	1.39±0.09	2.04±0.27
20-22	1.05±0.16	1.24±0.09	1.20±0.19
22-24	2.20±0.26	1.29±0.09	2.63±0.31
24-26	1.96±0.24	1.41±0.09	2.38±0.29
26-28	2.02±0.24	1.25±0.09	2.38±0.28
28-30	1.09±0.15	1.45±0.09	1.33±0.18

Core MV-43

Depth interval (cm)	Excess ^{210}Pb activity (dpm g^{-1})	Supported ^{210}Pb activity (dpm g^{-1})	Excess ^{210}Pb inventory (dpm cm^{-2})
0-1	12.64±0.44	0.55±0.02	8.55±0.29
1-2	13.46±0.46	0.51±0.02	9.32±0.32
2-3	10.28±0.40	0.52±0.02	7.44±0.29
3-4	10.41±0.44	0.49±0.02	8.39±0.36
4-5	7.43±0.40	0.58±0.03	5.57±0.30
5-6	8.23±0.39	0.34±0.02	6.25±0.30
6-8	6.52±0.37	0.57±0.03	10.09±0.57
8-10	6.06±0.32	0.52±0.03	10.40±0.58
10-12	3.36±0.29	0.55±0.04	6.36±0.55
12-14	4.31±0.30	0.64±0.04	7.60±0.54
14-16	2.79±0.29	0.47±0.04	4.87±0.50
16-18	3.10±0.27	0.53±0.04	5.25±0.45
18-20	1.94±0.26	0.58±0.06	3.34±0.45
20-22	4.66±0.31	0.46±0.03	8.19±0.54
22-24	2.72±0.27	0.39±0.04	4.77±0.48
24-26	1.46±0.22	0.45±0.05	2.59±0.39
26-28	2.88±0.28	0.53±0.05	4.67±0.46
28-30	1.85±0.25	0.46±0.05	3.14±0.43

Core MV-44

Depth interval (cm)	Excess ^{210}Pb activity (dpm g^{-1})	Supported ^{210}Pb activity (dpm g^{-1})	Excess ^{210}Pb inventory (dpm cm^{-2})
0-1	23.19±0.78	1.57±0.05	10.94±0.37
1-2	22.62±0.76	1.68±0.05	10.15±0.34
2-3	19.74±0.59	1.31±0.04	9.30±0.28
3-4	18.82±0.55	1.34±0.04	9.96±0.29
4-5	16.95±0.53	1.38±0.04	9.41±0.29
5-6	16.84±0.56	1.35±0.04	9.22±0.31
6-8	16.12±0.55	1.42±0.05	17.16±0.59
8-10	10.61±0.48	1.21±0.05	11.26±0.51
10-12	7.67±0.38	1.46±0.06	9.35±0.46
12-14	4.96±0.28	1.46±0.07	6.29±0.36
14-16	4.11±0.28	1.17±0.06	5.30±0.36
16-18	4.34±0.29	1.15±0.06	5.74±0.39
18-20	2.83±0.25	1.41±0.08	3.72±0.32
20-22	2.52±0.24	1.40±0.09	3.38±0.32
22-24	1.76±0.20	1.29±0.09	2.44±0.28
24-26	3.92±0.27	1.14±0.06	5.27±0.36
26-28	1.42±0.17	1.23±0.08	3.84±0.45
30-32	2.03±0.19	1.30±0.08	2.63±0.26

Core MV-47

Depth interval (cm)	Excess ^{210}Pb activity (dpm g^{-1})	Supported ^{210}Pb activity (dpm g^{-1})	Excess ^{210}Pb inventory (dpm cm^{-2})
0-1	73.33±1.49	1.35±0.03	23.39±0.48
1-2	67.74±1.42	0.94±0.02	22.14±0.47
2-3	59.97±0.59	1.30±0.03	19.26±0.42
3-4	50.37±1.01	0.92±0.02	18.02±0.36
4-5	44.06±0.95	0.89±0.02	17.29±0.37
5-6	41.56±0.94	1.06±0.02	17.54±0.39
6-8	35.55±0.72	1.03±0.02	30.48±0.62
8-10	24.53±0.49	0.93±0.02	22.75±0.46
10-12	21.07±0.53	0.89±0.02	22.07±0.56
12-14	21.25±0.49	0.91±0.02	21.84±0.50
14-16	12.37±0.39	0.69±0.02	13.59±0.43
16-18	12.21±0.41	0.69±0.02	12.86±0.43
18-20	10.55±0.38	0.75±0.03	11.29±0.40
20-22	2.95±0.30	0.73±0.06	2.91±0.29
22-24	2.20±0.27	0.73±0.07	2.41±0.29
24-26	2.23±0.24	0.78±0.06	2.34±0.25
26-28	1.54±0.21	0.73±0.07	1.71±0.23
28-30	1.31±0.21	0.72±0.08	1.46±0.24
34-36	1.21±0.17	0.99±0.08	1.35±0.18
36-38	1.98±0.23	0.88±0.07	2.22±0.26

Core MV-50

Depth interval (cm)	Excess ^{210}Pb activity (dpm g^{-1})	Supported ^{210}Pb activity (dpm g^{-1})	Excess ^{210}Pb inventory (dpm cm^{-2})
0-1	131.12±1.92	2.07±0.03	45.14±0.66
1-2	106.59±1.39	2.11±0.03	40.45±0.53
2-3	80.77±0.59	3.42±0.05	31.21±0.48
3-4	73.89±1.13	6.24±0.09	26.44±0.41
4-5	52.38±1.04	5.68±0.10	18.49±0.37
5-6	46.89±0.98	2.14±0.04	19.14±0.39
6-8	35.05±0.79	1.96±0.04	26.88±0.61
8-10	13.67±0.57	1.94±0.07	10.64±0.44
10-12	10.39±0.47	1.85±0.07	9.46±0.43
12-14	4.19±0.30	2.18±0.11	3.62±0.26
14-16	6.18±0.39	1.82±0.09	5.42±0.34
16-18	3.31±0.31	2.00±0.12	2.87±0.27
18-20	3.11±0.28	1.53±0.09	2.83±0.25
20-22	2.89±0.29	1.90±0.11	2.44±0.25

Core MV-53

Depth interval (cm)	Excess ^{210}Pb activity (dpm g^{-1})	Supported ^{210}Pb activity (dpm g^{-1})	Excess ^{210}Pb inventory (dpm cm^{-2})
0-1	82.47±1.59	2.66±0.05	38.63±0.75
1-2	54.97±1.04	2.71±0.05	31.39±0.59
2-3	35.11±0.86	3.71±0.08	19.41±0.48
3-4	14.58±0.57	7.96±0.21	7.47±0.29
4-5	13.58±0.49	2.70±0.08	7.55±0.28
5-6	13.09±0.47	1.91±0.06	7.24±0.26
6-8	10.13±0.48	2.24±0.09	9.42±0.45
8-10	9.29±0.49	2.01±0.09	8.97±0.48
10-12	6.19±0.42	2.13±0.11	6.05±0.41
12-14	2.95±0.29	2.21±0.13	2.83±0.28
14-16	1.01±0.15	2.24±0.10	1.00±0.15

Core MV-56

Depth interval (cm)	Excess ^{210}Pb activity (dpm g^{-1})	Supported ^{210}Pb activity (dpm g^{-1})	Excess ^{210}Pb inventory (dpm cm^{-2})
0-1	7.37±0.37	1.73±0.07	8.44±0.42
1-2	6.89±0.32	1.68±0.06	7.33±0.34
2-3	5.94±0.31	1.45±0.06	6.18±0.32
3-4	2.25±0.21	1.74±0.09	2.17±0.21
4-5	3.37±0.27	1.59±0.09	3.22±0.26
5-6	1.87±0.18	1.52±0.08	1.94±0.19

Core MV-59

Depth interval (cm)	Excess ^{210}Pb activity (dpm g^{-1})	Supported ^{210}Pb activity (dpm g^{-1})	Excess ^{210}Pb inventory (dpm cm^{-2})
0-1	13.41±0.44	1.38±0.04	15.70±0.52
1-2	23.50±0.85	1.74±0.06	27.07±0.98
2-3	6.02±0.32	1.59±0.08	7.00±0.37
3-4	3.69±0.25	1.55±0.08	4.21±0.29
5-6	3.94±0.26	1.53±0.08	4.39±0.29
6-8	4.07±0.28	1.65±0.09	9.05±0.63
8-10	2.78±0.21	1.39±0.08	6.32±0.49

Core MV-60

Depth interval (cm)	Excess ^{210}Pb activity (dpm g^{-1})	Supported ^{210}Pb activity (dpm g^{-1})	Excess ^{210}Pb inventory (dpm cm^{-2})
0-1	69.56±1.30	2.73±0.05	33.46±0.63
1-2	28.18±0.83	2.48±0.07	14.65±0.43
2-3	17.60±0.63	2.58±0.08	9.18±0.33
3-4	11.92±0.58	2.75±0.11	6.41±0.31
4-5	5.31±0.41	2.79±0.14	3.06±0.23
5-6	6.51±0.45	2.57±0.13	3.72±0.26
8-10	1.91±0.16	3.95±0.11	2.21±0.19
10-12	1.42±0.12	4.34±0.09	1.71±0.14
14-16	1.51±0.11	6.26±0.09	1.73±0.12
16-18	1.38±0.14	3.08±0.09	1.49±0.15

Core MV-65

Depth interval (cm)	Excess ^{210}Pb activity (dpm g^{-1})	Supported ^{210}Pb activity (dpm g^{-1})	Excess ^{210}Pb inventory (dpm cm^{-2})
0-1	19.04±0.69	1.78±0.06	12.79±0.47
1-2	6.69±0.38	1.56±0.07	5.30±0.30
2-3	4.77±0.33	1.64±0.08	3.44±0.24
3-4	7.85±0.45	1.67±0.08	6.43±0.37
4-5	4.41±0.33	1.85±0.09	3.40±0.25

Core MV-67

Depth interval (cm)	Excess ^{210}Pb activity (dpm g^{-1})	Supported ^{210}Pb activity (dpm g^{-1})	Excess ^{210}Pb inventory (dpm cm^{-2})
0-1	24.68±0.68	2.16±0.06	16.76±0.46
1-2	16.57±0.66	2.29±0.08	11.94±0.47
2-3	13.81±0.53	2.60±0.09	9.58±0.37
3-4	12.83±0.55	2.74±0.09	8.96±0.38
4-5	12.66±0.47	2.69±0.08	9.88±0.37
5-6	6.56±0.35	2.95±0.11	5.13±0.27

Core MV-69

Depth interval (cm)	Excess ^{210}Pb activity (dpm g^{-1})	Supported ^{210}Pb activity (dpm g^{-1})	Excess ^{210}Pb inventory (dpm cm^{-2})
0-1	57.64±1.04	2.97±0.05	33.37±0.60
1-2	30.02±0.71	2.76±0.06	19.73±0.47
2-3	19.65±0.69	2.87±0.09	12.74±0.45
3-4	8.97±0.47	3.15±0.12	6.18±0.32
4-5	5.64±0.36	3.22±0.13	3.92±0.25
5-6	1.51±0.15	3.52±0.11	1.01±0.09
6-8	2.53±0.17	3.28±0.09	3.41±0.11
14-16	1.88±0.14	2.74±0.08	2.49±0.09

Core MV-70

Depth interval (cm)	Excess ^{210}Pb activity (dpm g^{-1})	Supported ^{210}Pb activity (dpm g^{-1})	Excess ^{210}Pb inventory (dpm cm^{-2})
0-1	50.99±1.04	3.60±0.07	24.96±0.51
1-2	16.59±0.55	3.61±0.09	9.29±0.31
2-3	9.19±0.43	3.92±0.13	5.90±0.27
3-4	10.83±0.48	3.69±0.12	7.54±0.33
4-5	9.72±0.41	3.49±0.11	6.77±0.29
5-6	4.23±0.24	3.88±0.12	2.87±0.17
6-8	3.28±0.24	3.40±0.13	4.30±0.32

Core MV-72

Depth interval (cm)	Excess ^{210}Pb activity (dpm g^{-1})	Supported ^{210}Pb activity (dpm g^{-1})	Excess ^{210}Pb inventory (dpm cm^{-2})
0-1	20.72±0.61	1.16±0.03	16.21±0.48
1-2	10.02±0.49	1.17±0.05	8.12±0.39
2-3	9.11±0.46	1.42±0.06	7.74±0.39
3-4	6.42±0.42	1.56±0.08	5.77±0.38
4-5	1.95±0.24	1.34±0.09	1.69±0.21
5-6	4.01±0.33	1.18±0.08	3.41±0.28
6-8	1.04±0.15	1.07±0.08	1.74±0.25

Core MV-76

Depth interval (cm)	Excess ^{210}Pb activity (dpm g^{-1})	Supported ^{210}Pb activity (dpm g^{-1})	Excess ^{210}Pb inventory (dpm cm^{-2})
0-1	33.40±0.96	2.63±0.07	20.25±0.58
1-2	12.55±0.65	2.07±0.09	8.59±0.44
2-3	4.53±0.35	2.21±0.12	3.31±0.26
3-4	6.54±0.47	2.18±0.12	4.75±0.34
6-8	1.39±0.17	1.71±0.09	2.07±0.25

APPENDIX C: GRAIN SIZE FOR CORES DISCUSSED IN CHAPTER 2

Core MV-12

Depth interval (cm)	Clay %	Silt %	Sand %
0-2	18.2	78	3.8
2-3	17.3	78.4	4.3
3-4	17.7	77.3	5
4-5	14.7	82.2	3.1
5-6	14.1	82.4	3.5
6-8	15.9	81.4	2.7

Core MV-18

Depth interval (cm)	(Clay+Silt) %	Sand %
0-2	47.0	53.0
2-4	28.2	71.8
4-6	55.2	44.9
6-8	71.2	28.8
8-10	73.1	26.9
10-12	75.7	24.3
12-14	76.2	23.8
14-16	79.6	20.4
16-18	79.8	20.2
18-20	71.6	28.4
20-22	67.4	32.6
22-24	65.2	34.8
24-26	62.4	37.6
26-28	20.4	79.6

Core MV-19

Depth interval (cm)	(Clay+Silt) %	Sand %
0-2	18.4	81.6
2-4	18.2	81.8
4-6	17.6	82.4
6-8	17.0	83.0
8-12	18.4	81.6
12-14	22.1	77.9
14-16	16.3	83.7
16-18	18.6	81.5
18-20	17.8	82.3
20-22	16.5	83.5
22-24	21.2	78.8
24-26	22.5	77.5
26-28	18.4	81.6
28-30	18.2	81.8

Core MV-26

Depth interval (cm)	Clay %	Silt %	Sand %
0-1	82.1	16.2	1.7
1-2	83.1	13.3	3.6
2-3	81.9	17.5	0.6
3-4	87.1	9.9	3
4-5	86.9	10.5	2.6
5-6	87.9	11.1	1
6-8	91.5	5.5	3
8-10	87.9	10.7	1.4
10-12	90.7	7.1	2.2
12-14	93.3	4.4	2.3
14-16	88.8	8.7	2.5
16-18	83.5	13.8	2.7
18-20	79.4	19.2	1.4
20-22	90.1	7.5	2.4
22-24	89.5	10.5	0
24-26	91.6	7.1	1.3
26-28	90.4	6.7	2.9
28-30	93.8	6	0.2

Core MV-28

Depth interval (cm)	Clay %	Silt %	Sand %
0-1	87.2	12.2	0.6
1-2	89.6	9.5	0.9
2-3	90.9	7.8	1.3
3-4	89.9	9.2	0.9
4-5	88	10.7	1.3
5-6	89.3	9.6	1.1
8-10	92.7	6	1.3
10-12	92.9	5.7	1.4
12-14	95.9	3.8	0.3
14-16	96.6	2.7	0.7
16-18	95.5	3.8	0.7
18-20	90.7	9.1	0.2
20-22	79.4	19.2	1.4
22-24	92.2	6.7	1.1
24-26	93.6	4.3	2.1
26-28	94.5	4.8	0.7
28-30	95.3	3.4	1.3

Core MV-38

Depth interval (cm)	Clay %	Silt %	Sand %
0-1	58.4	40	1.6
1-2	50.5	47.1	2.4
2-3	48	48.8	3.2
3-4	51.6	45.9	2.5
4-5	60	39.1	0.9
5-6	59.9	37.5	2.6
6-8	68	28.9	3.1
8-10	72.1	25	2.9
10-12	66.4	32	1.6
12-14	73.9	23.3	2.8
14-16	72.8	25.3	1.9
16-18	75.4	22.6	2
18-20	75.6	23.5	0.9
20-22	79.2	18.2	2.6
22-24	78.5	19	2.5
24-26	78.1	20.2	1.7

Core MV-39

Depth interval (cm)	Clay %	Silt %	Sand %
0-4	65.7	31.7	2.6
4-5	79.7	17.4	2.9
5-6	80.7	15.8	2.9
6-8	81.1	17	3.5
8-10	82.3	14.8	1.9
10-12	81.1	17	2.9
16-18	82.2	14.9	1.9
18-20	81.7	15.4	2.9
20-22	82.9	14.9	2.9
22-24	81.9	16.2	2.2
24-26	85.3	12.8	1.9
26-28	85.5	13.3	1.9
28-30	85.5	12.2	1.2

Core MV-41

Depth interval (cm)	(Clay+Silt) %	Sand %
7-9	98.4	1.6
14-16	99.0	1.0
28-30	99.2	0.8
42-44	99.1	0.9
49-51	99.0	1.0
61-63	97.1	2.9
73-75	99.2	0.8
85-87	98.1	1.9
97-99	98.9	1.1
102-104	93.2	6.8
109-111	99.0	1.0
121-123	98.8	1.2
133-135	98.7	1.3
145-147	93.6	6.4
157-159	98.6	1.4
169-171	98.8	1.2
193-195	98.4	1.6
205-207	99.1	0.9
309-311	98.5	1.5
361-363	99.1	0.9
413-415	99.5	0.5
517-519	99.4	0.6
569-571	97.2	2.8
621-623	97.4	2.6
673-675	99.3	0.7
725-727	99.5	0.5
777-779	99.1	0.9
829-823	99.3	0.7
881-883	98.2	1.8
933-935	99.3	0.7
985-987	97.9	2.1
1037-1039	99.4	0.6
1141-1143	99.0	1.0
1193-1195	99.4	0.6
1245-1247	99.6	0.4

Core MV-42

Depth interval (cm)	Clay %	Silt %	Sand %
0-1	95.5	4.4	0.1
1-2	95.5	3.4	1.1
2-3	92.8	7.2	0
3-4	92.8	6.3	0.9
4-5	95.2	4.1	0.7
5-6	93.3	6.3	0.4
6-8	95.2	3.6	1.2
8-10	92.1	5.6	2.3
10-12	85	12.9	2.1
12-14	86	12.3	1.7
14-16	84.3	14	1.7
16-18	90.3	9	0.7
18-20	85.1	12	2.9
20-22	87.2	11	1.8
22-24	78.5	20.6	0.9
24-26	86.2	11.2	2.6
26-28	87.7	10	2.3
28-30	88.3	9.4	2.3

Core MV-43

Depth interval (cm)	Clay %	Silt %	Sand %
0-1	40.7	49.2	10.1
1-2	67.8	21.5	10.7
2-3	62	28.7	9.3
3-4	57	29.9	13.1
4-5	48.8	38	13.2
5-6	62.7	23.1	14.2
6-8	65.1	24.5	10.4
8-10	68.6	20.8	10.6
10-12	65	22.6	12.4
12-14	60.3	26.1	13.6
14-16	65.7	19.8	14.5
16-18	69	20.4	10.6
18-20	76	15.3	8.7
20-22	72.2	17.9	9.9
22-24	69.3	19	11.7
24-26	72.6	15.9	11.5
26-28	73.3	17.6	9.1
28-30	66.8	20.7	12.5

Core MV-44

Depth interval (cm)	Clay %	Silt %	Sand %
0-1	61.4	33.9	4.7
1-2	74.1	25.2	0.7
2-3	75.2	21.9	2.9
3-4	77.6	19.4	3
4-5	74.7	23	2.3
5-6	79.4	16.1	4.5
6-8	77.1	19.2	3.7
8-10	82.4	15.4	2.2
10-12	81.3	16.4	2.3
12-14	78.5	17.1	4.4
14-16	79	18	3
16-18	80.2	18.1	1.7
18-20	80	18.7	1.3
20-22	78.3	18	3.7
22-24	74.8	20.5	4.7
24-26	66.1	30.1	3.8
26-28	74.4	21.8	3.8
28-30	73.9	23.5	2.6

Core MV-46

Depth interval (cm)	(Clay+Silt) %	Sand %
0-2	98.8	1.2
7-9	98.8	1.2
14-16	98.6	1.4
21-23	98.6	1.4
28-30	98.7	1.3
35-37	98.7	1.3
42-44	98.3	1.7
49-51	98.9	1.1
61-63	99.0	1.0
73-75	98.7	1.3
85-87	97.6	2.4
97-99	97.4	2.6
109-111	95.8	4.2
121-123	98.1	1.9
193-195	96.7	3.3
205-207	97.1	2.9
257-259	97.0	3.0
309-311	91.7	8.3
361-363	95.2	4.8
413-415	92.9	7.1
517-519	94.6	5.4
569-571	96.8	3.2
621-623	95.9	4.1
673-675	96.9	3.1
725-727	97.5	2.5
777-779	98.2	1.8
829-823	97.3	2.7
881-883	97.3	2.7
933-935	98.4	1.6
985-987	98.8	1.2
1037-1039	99.4	0.6
1141-1143	99.5	0.5
1193-1195	97.5	2.5
1245-1247	98.7	1.3
1297-1299	97.6	2.4
1325-1327	99.1	0.9
1349-1351	98.7	1.3
1428-1430	99.5	0.5

Core MV-47

Depth interval (cm)	Clay %	Silt %	Sand %
0-1	92	6.4	1.6
1-2	93.9	4.2	1.9
2-3	87.5	12	0.5
3-4	91.8	8.2	0
4-5	93.6	5.8	0.6
5-6	90.9	7.4	1.7
6-8	89.4	10.6	0
8-10	88.3	11	0.7
10-12	92	7.2	0.8
12-14	87.3	12.1	0.6
14-16	85.4	14.6	0
16-18	87	12.1	0.9
18-20	84.4	15	0.6
20-22	84.9	14.6	0.5
22-24	85.4	13.7	0.9
24-26	83.2	15.8	1
26-28	86	11.8	2.2
28-30	87.4	11.9	0.7

Core MV-49

Depth interval (cm)	(Clay+Silt) %	Sand %
61-63	95.6	4.4
157-159	87.1	12.9
169-171	90.0	10.0
181-183	92.2	7.8
193-195	94.8	5.2
205-207	97.0	3.0
217-219	97.0	3.0
229-231	96.8	3.2
269-271	93.3	6.7
281-283	91.1	8.9
293-295	90.0	10.0
361-363	84.9	15.1
387-389	89.2	10.8
399-401	93.1	6.9
413-415	92.2	7.8
425-427	94.1	5.9
436-438	92.1	7.9
465-467	89.4	10.6
489-491	91.7	8.3
517-519	92.5	7.5
569-571	87.8	12.2
621-623	90.7	9.3
673-675	85.0	15.0
725-727	90.6	9.4
777-779	88.1	11.9
829-823	92.7	7.3
881-883	92.8	7.2
893-895	93.2	6.8
905-907	96.6	3.4
917-919	95.5	4.5
948-950	96.6	3.4
960-962	94.4	5.6
972-974	94.3	5.7
985-987	94.1	5.9
1022-1024	94.2	5.8
1034-1036	91.8	8.2
1037-1039	93.0	7.0
1089-1091	91.2	8.8

Core MV-50

Depth interval (cm)	Clay %	Silt %	Sand %
0-1	84.8	13.6	1.6
1-2	85.1	13.2	1.7
2-3	82.5	14.5	3
3-4	86.6	12.2	1.2
4-5	90.4	8.2	1.4
5-6	92.1	7.2	0.7
6-8	90.5	8.1	1.4
8-10	91.6	6.1	2.3
10-12	92.2	7.4	0.4
12-14	91.7	8.3	0
14-16	91.4	7.7	0.9
16-18	87.3	10	2.7
18-20	93.6	5.3	1.1
20-22	90.9	9	0.1
22-24	90.6	7.9	1.5
24-26	91.6	6.4	2
26-28	88.7	10.7	0.6
28-30	90.7	8.1	1.2

Core MV-69

Depth interval (cm)	Clay %	Silt %	Sand %
0-1	53.9	44	2.1
1-2	35.2	62.5	2.3
2-3	45.6	52	2.4
3-4	47.8	50.4	1.8
4-5	45.4	52.3	2.3
5-6	47.1	50.2	2.7
6-8	34.2	63.7	2.1
14-16	43.2	54.9	1.9
16-18	48.6	47.9	3.5
18-20	52.5	44.7	2.8
20-22	46.7	50.9	2.4
22-24	36.1	60.3	3.6

APPENDIX D: POROSITY DATA

Core MV-10

Depth interval (cm)	Porosity
0-1	0.63
1-2	0.65
2-3	0.65
3-4	0.60
4-5	0.63
5-6	0.59

Core MV-12

Depth interval (cm)	Porosity
0-2	0.59
2-3	0.59
3-4	0.58
4-5	0.62
5-6	0.56
6-8	0.61

Core MV-14

Depth interval (cm)	Porosity
0-1	0.77
1-2	0.73
2-3	0.67
3-4	0.71
4-5	0.68
5-6	0.70
6-8	0.69
8-10	0.68

Core MV-16

Depth interval (cm)	Porosity
0-1	0.61
1-2	0.60
2-3	0.61
3-4	0.61
4-5	0.62
5-6	0.58
6-8	0.63

Core MV-18

Depth interval (cm)	Porosity
0-4	0.65
4-5	0.49
5-6	0.63
6-8	0.68
8-10	0.76
10-12	0.74
12-14	0.74
14-16	0.75
16-18	0.74
18-20	0.73
20-22	0.71
22-24	0.71
24-26	0.69

Core MV-19

Depth interval (cm)	Porosity
2-3	0.57
3-4	0.56
4-5	0.57
5-6	0.54
6-8	0.58
8-12	0.59
12-14	0.57
14-16	0.54

Core MV-20

Depth interval (cm)	Porosity
0-1	0.66
1-2	0.65
2-3	0.67
3-4	0.66
4-5	0.67
5-6	0.69
6-8	0.68
8-10	0.70
10-12	0.69

Core MV-21

Depth interval (cm)	Porosity
0-1	0.69
1-2	0.68
2-3	0.70
3-4	0.70
4-5	0.71
5-6	0.71
6-8	0.71

Core MV-24

Depth interval (cm)	Porosity
0-1	0.82
1-2	0.85
2-3	0.84
3-4	0.83
4-5	0.83
5-6	0.81
6-8	0.83
8-10	0.80
10-12	0.83
12-14	0.79

Core MV-26

Depth interval (cm)	Porosity
0-1	0.90
1-2	0.84
2-3	0.84
3-4	0.83
4-5	0.84
5-6	0.84
6-8	0.69
8-10	0.70
10-12	0.72
12-14	0.70
14-16	0.71
18-20	0.72
20-22	0.73
22-24	0.72

Core MV-28

Depth interval (cm)	Porosity
0-1	0.85
1-2	0.83
2-3	0.82
3-4	0.81
4-5	0.81
5-6	0.81
8-10	0.79
10-12	0.80
12-14	0.81

Core MV-30

Depth interval (cm)	Porosity
0-1	0.91
1-2	0.84
2-3	0.83
3-4	0.82
4-5	0.80
5-6	0.81
6-8	0.79
10-12	0.78
12-14	0.78
14-16	0.79

Core MV-32

Depth interval (cm)	Porosity
0-2	0.83
2-4	0.82
4-6	0.78
6-8	0.77

Core MV-38

Depth interval (cm)	Porosity
0-1	0.89
1-2	0.85
2-3	0.83
3-4	0.82
4-5	0.83
5-6	0.82
6-8	0.79
8-10	0.79
10-12	0.79
12-14	0.79

Core MV-39

Depth interval (cm)	Porosity
0-2	0.80
2-3	0.81
3-5	0.80
5-6	0.79
6-8	0.78
8-10	0.76
10-12	0.77
16-18	0.77
18-20	0.75

Core MV-42

Depth interval (cm)	Porosity
0-1	0.83
1-2	0.84
2-3	0.83
3-4	0.80
4-5	0.83
5-6	0.78
6-8	0.78
8-10	0.80
10-12	0.77
12-14	0.78
14-16	0.80
16-18	0.78
18-20	0.78
20-22	0.78
22-24	0.77
24-26	0.77
26-28	0.78
28-30	0.77

Core MV-43

Depth interval (cm)	Porosity
0-1	0.74
1-2	0.74
2-3	0.73
3-4	0.70
4-5	0.72
5-6	0.71
6-8	0.71
8-10	0.68
10-12	0.64
12-14	0.67
14-16	0.67
16-18	0.68
18-20	0.68
20-22	0.67
22-24	0.67
24-26	0.66
26-28	0.69
28-30	0.68

Core MV-44

Depth interval (cm)	Porosity
0-1	0.82
1-2	0.83
2-3	0.82
3-4	0.80
4-5	0.79
5-6	0.79
6-8	0.80
8-10	0.80
10-12	0.77
12-14	0.76
14-16	0.76
16-18	0.75
18-20	0.75
20-22	0.75
22-24	0.74
24-26	0.75
26-28	0.74
30-32	0.76

Core MV-47

Depth interval (cm)	Porosity
0-1	0.88
1-2	0.88
2-3	0.88
3-4	0.87
4-5	0.85
5-6	0.84
6-8	0.84
8-10	0.83
10-12	0.80
12-14	0.81
14-16	0.79
16-18	0.80
18-20	0.80
20-22	0.81
22-24	0.79
24-26	0.80
26-28	0.79
28-30	0.79
34-36	0.79
36-38	0.79

Core MV-50

Depth interval (cm)	Porosity
0-1	0.87
1-2	0.86
2-3	0.85
3-4	0.86
4-5	0.87
5-6	0.85
6-8	0.86
8-10	0.85
10-12	0.83
12-14	0.84
14-16	0.83
16-18	0.84
18-20	0.83
20-22	0.84

Core MV-53

Depth interval (cm)	Porosity
0-1	0.82
1-2	0.78
2-3	0.79
3-4	0.81
4-5	0.79
5-6	0.79
6-8	0.82
8-10	0.82
10-12	0.82
12-14	0.82
14-16	0.81

Core MV-56

Depth interval (cm)	Porosity
0-1	0.57
1-2	0.60
2-3	0.61
3-4	0.64
4-5	0.64
5-6	0.61

Core MV-59

Depth interval (cm)	Porosity
0-1	0.56
1-2	0.57
2-3	0.56
3-4	0.57
5-6	0.58
6-8	0.58
8-10	0.57

Core MV-60

Depth interval (cm)	Porosity
0-1	0.82
1-2	0.80
2-3	0.80
3-4	0.80
4-5	0.78
5-6	0.78
8-10	0.78
10-12	0.77
14-16	0.78
16-18	0.80

Core MV-65

Depth interval (cm)	Porosity
0-1	0.75
1-2	0.70
2-3	0.73
3-4	0.69
4-5	0.71

Core MV-67

Depth interval (cm)	Porosity
0-1	0.74
1-2	0.73
2-3	0.74
3-4	0.74
4-5	0.71
5-6	0.70

Core MV-69

Depth interval (cm)	Porosity
0-1	0.78
1-2	0.75
2-3	0.76
3-4	0.74
4-5	0.74
5-6	0.75
6-8	0.75
14-16	0.75

Core MV-70

Depth interval (cm)	Porosity
0-1	0.82
1-2	0.79
2-3	0.76
3-4	0.74
4-5	0.74
5-6	0.74
6-8	0.75

Core MV-72

Depth interval (cm)	Porosity
0-1	0.70
1-2	0.69
2-3	0.68
3-4	0.66
4-5	0.67
5-6	0.68
6-8	0.69

Core MV-76

Depth interval (cm)	Porosity
0-1	0.77
1-2	0.74
2-3	0.72
3-4	0.73
6-8	0.72

APPENDIX E: ABBREVIATIONS AND ACRONYMS USED IN TEXT

AMS	Accelerator Mass Spectrometry
BP	Before Present
CSC	Coral Sea Current
DEM	Digital Elevation Model
dpm	Decay Per Minute
GD	Gamma Density
GEOSECS	Geochemical Ocean Sections Study
GIS	Geographic Information System
GoP	Gulf of Papua
kHz	KiloHertz
LGM	Last Glacial Maximum
MAR	Mass Accumulation Rates
MBSF	Meter Below Sea Floor
MBSL	Meter Below Sea Level
MSCL	Multi-Sensor Core Logger
MS	Magnetic Susceptibility
Mt	Megatonnes
MWP	Melt-Water Pulse
NE	North East
NNE	North North East
PNG	Papua New Guinea
SAR	Sediment Accumulation Rates
SEC	South Equatorial Current
SSW	South South West
SW	South West
TDMA	Tri-Diagonal Matrix Algorithm
YD	Younger Dryas

Isotopes discussed in text

^{137}Cs	Caesium-137
^{14}C	Carbon-14
^{210}Pb	Lead-210
$^{239,240}Pu$	Plutonium-239,240
^{226}Ra	Radium-226
^{222}Rn	Radon-222
^{234}Th	Thorium-234

APPENDIX F: PERMISSION REQUEST

Dated: May 14, 2009 at 9:35 AM
From: Michael Connolly, MConnolly@agu.org
To: Zahid Muhammad, zmuham1@lsu.edu
Subject: Permission to add manuscript in dissertation

We are pleased to grant permission for the use of the material requested for inclusion in your thesis. The following non-exclusive rights are granted to AGU authors:

- All proprietary rights other than copyright (such as patent rights).
- The right to present the material orally.
- The right to reproduce figures, tables, and extracts, appropriately cited.
- The right to make hard paper copies of all or part of the paper for classroom use.
- The right to deny subsequent commercial use of the paper.

Further reproduction or distribution is not permitted beyond that stipulated. The copyright credit line should appear on the first page of the article or book chapter. The following must also be included, "Reproduced by permission of American Geophysical Union." To ensure that credit is given to the original source(s) and that authors receive full credit through appropriate citation to their papers,
we recommend that the full bibliographic reference be cited in the reference list. The standard credit line for journal articles is: "Author(s), title of work, publication title, volume number, issue number, citation number (or page number(s) prior to 2002), year. Copyright [year] American Geophysical Union."

If an article was placed in the public domain, in which case the words "Not subject to U.S. copyright" appear on the bottom of the first page or screen of the article, please substitute "published" for the word "copyright" in the credit line mentioned above.

Copyright information is provided on the inside cover of our journals. For permission for any other use, please contact the AGU Publications Office at AGU, 2000 Florida Ave., N.W., Washington, DC 20009.

Michael Connolly
Journals Publications Specialist

VITA

Zahid Muhammad was born in 1970, and grew up in Karachi, Pakistan. Zahid graduated from The Karachi University in 1995 with a master of science degree in applied chemistry. After working for Shell Pakistan Limited, Zahid enrolled at Louisiana State University and graduated with a master's degree in 2001 in petroleum engineering. During Zahid's doctorate research at Louisiana State University, he traveled to the Gulf of Papua in March-April 2004. He is expected to graduate with a Doctor of Philosophy degree in oceanography, in August 2009.